FOSSIL ENERGY

DOE/BC/14994-16
OSTI ID: 9329

SUPRI HEAVY OIL RESEARCH PROGRAM
TWENTY-SECOND ANNUAL REPORT

AUGUST 26, 1998 – AUGUST 25, 1999

SUPRI TR 117

By
William E. Brigham
Anthony R. Kovscek
Louis M. Castanier

May 1999

Work Performed Under Contract No. DE-FG22-96BC14994

Stanford University
Stanford, California

National Petroleum Technology Office
U. S. DEPARTMENT OF ENERGY
Tulsa, Oklahoma

DISCLAIMER

This report was prepared as an account of work sponsored by an agency of the United States Government. Neither the United States Government nor any agency thereof, nor any of their employees, makes any warranty, expressed or implied, or assumes any legal liability or responsibility for the accuracy, completeness, or usefulness of any information, apparatus, product, or process disclosed, or represents that its use would not infringe privately owned rights. Reference herein to any specific commercial product, process, or service by trade name, trademark, manufacturer, or otherwise does not necessarily constitute or imply its endorsement, recommendation, or favoring by the United States Government or any agency thereof. The views and opinions of authors expressed herein do not necessarily state or reflect those of the United States Government.

This report has been reproduced directly from the best available copy.

DOE/BC/14994-16
Distribution Category UC-122

SUPRI Heavy Oil Research Program
Twenty-Second Annual Report

August 26, 1998 – August 25, 1999

SUPRI TR 117

By
William E. Brigham
Anthony R. Kovscek
Louis M. Castanier

May 1999

Work Performed Under Contract DE-FG22-96BC14994

Prepared for
U.S. Department of Energy
Assistant Secretary for Fossil Energy

Thomas Reid, Project Manager
National Petroleum Technology Office
P.O. Box 3628
Tulsa, OK 74101

Prepared by
Stanford University
Petroleum Engineering Department
65 Green Earth Sciences Bldg.
Stanford, CA 94305

TABLE OF CONTENTS

	Page
List of Tables	vii
List of Figures	ix
Acknowledgements	xiii
Summary	xv
PROJECT 1: FLOW PROPERTIES STUDY	**1**
1.1 Effects of Temperature on Multiphase Relative Permeability (S. Akin, L.M. Castanier, and W.E. Brigham)	3
1.2 Experimental and Theoretical Investigation of Multiphase Flow in Fractured Media (Edgar Rangel-German)	17
1.2.1 Experimental and Theoretical Investigation of Multiphase Flow in Fractured Media (Edgar Rangel-German, S. Akin and L. Castanier)	17
1.2.2 SPE 54591: Multiphase-Flow Properties of Fractured Porous Media (Edgar Rangel-German, S. Akin and L. Castanier)	31
PROJECT 2: IN-SITU COMBUSTION	**49**
2.1 In-Situ Combustion (Louis Castanier)	51
2.1.1 Introduction: Advantages of In-situ Combustion	51
2.1.2 In-situ Combustion with Metallic Additives	52
2.1.3 In-situ Combustion and Solvents: Possible Research	52
PROJECT 3: STEAM WITH ADDITIVES	**57**
3.1 Simulation of Early-Time Response of Single-Well Steam Assisted Gravity Drain (SW-SAGD) (Keith Elliott and A.R. Kovscek)	59
3.1.1 SPE 54618	59
3.2 Visualization of solution Gas Drive in Medium to Heavy Oils	73

(David George)
3.2.1 Abstract 73
3.2.2 Introduction 73
3.2.2.1 Solution Gas Drive 73
3.2.2.2 Micromodels 80
3.2.2.3 Objectives 82
3.2.3 Experimental Apparatus 83
3.2.3.1 Pressure Vessel 83
3.2.3.2 Pressure System 86
3.2.3.3 Optics 87
3.2.4 Experimentation and Results 88
3.2.4.1 Foam Flow 88
3.2.4.2 Bubble Nucleation in a N_2/Water System 88
3.2.4.3 Solution Gas Drive 89
3.2.5 Plans 90
3.2.6 Conclusions 91
3.2.7References 91

3.3 Visualization of Multiphase Flow Through Porous Media 95
(Bolivia Vega)
3.3.1 Literature Review 95
3.3.1.1 Foamy Oil 95
3.3.1.2 Hamaca Case 97
3.3.1.3 Micromodels and Nucleation 97
3.3.2 Research Project 98
3.3.3 Conclusions 99
3.3.4 References 100

3.4 Gas Drive in Heavy Oils 101
(Prabhat Arora)
3.4.1 Introduction 101
3.4.2 Literature Review 102
3.4.3 Population Balance Model 103
3.4.4 Bubble Nucleation 104
3.4.5 Bubble Growth in Porous Media 105
3.4.6 Summary 107
3.4.7 References 107

3.5 Reservoir Simulation of Foam Displacement Processes 109
(Anthony R. Kovscek)

PROJECT 4: FORMATION EVALUATION **121**

4.1 A Streamline Approach to Inverse Problems 123
(Yuandong Wang)
4.1.1 Introduction 123
4.1.1.1 Brief Description of the Study 123

4.1.1.2 Example Problem to Solve 123
4.1.1.3 Importance of the Research 124
4.1.2 Literature Review 124
4.1.2.1 Simulated Annealing 125
4.1.2.2 Sensitivity Studies 126
4.1.2.3 Geo-Statistical and Streamline Approach 126
4.1.2.4 Streamlines and Mobility Ratio 127
4.1.2.5 Streamline Simulator (3DSL) 129
4.1.3 Basic Ideas 129
4.1.3.1 Streamline Breakthrough Versus Production Factional Flow 129
4.1.3.2 Permeability Modification Along the Streamline 130
4.1.4 Steps of the Streamline Approach to the Inverse Problem 131
4.1.5 Strategies of the Study 131
4.1.5.1 Starting Simplifications 131
4.1.5.2 Programming in C++ 132
4.1.5.3 Way to Modify the Permeability Distribution 133
4.1.6 Equations 133
4.1.6.1 Objective Functions 133
4.1.6.2 Systems to Solve for Modification of the Permeability Along Streamlines 135
4.1.6.3 Sensitivity Study – Computing of Derivatives 137
4.1.7 Preliminary Results, Plans and Expectations 140
4.1.7.1 Some Preliminary Results 140
4.1.7.2 Plans 140
4.1.8 Nomenclature 141
4.1.9 References 143

4.2 Displacement Efficiencies for Direct-Line Drive and Edge-Water Drive-waterflooding Using Streamtube Methods (Amos O. Kehinde) 149
4.2.1 Summary 149
4.2.2 Introduction 149
4.2.3 Objectives 154
4.2.4 Literature Review 155
4.2.4.1 Laboratories Studies 155
4.2.4.2 Simulation 156
4.2.4.3 Analytical Methods 157
4.2.5 Future Work Plans 161
4.2.6 References 162

PROJECT 5: FIELD SUPPORT SERVICES 165

LIST OF TABLES

	Page
PROJECT 1: FLOW PROPERTIES STUDY	**1**
1.1 Effect of Temperature on Multiphase Relative Permeability (S. Akin, L.M. Castanier, and W.E. Brigham)	3
1. A summary of the recent experimental investigations of temperature effects on relative permeability	6
2. Properties of porous medium and fluids used for hypothetical experiments	8
3. Stability numbers for different experiments with no initial water water saturation	8
4. End point oil saturation and relative permeability to water at different temperatures without initial water saturation	9
5. Stability numbers for different experiments with initial water water saturation	9
6. End point oil saturation and relative permeability to water at different temperatures with initial water saturation	9
7. Properties of the sand and fluids used in the first set of experiments	10
1.2.1Experimental and Theoretical Investigation of Multiphase Flow in Fractured Media (Edgar Rangel-German, S. Akin and L. Castanier)	17
1. Rates and timing for the core with thin fracture	22
1.2.2SPE 54591: Multiphase-Flow Properties of Fractured Porous Media (Edgar Rangel-German, S. Akin and L. Castanier)	31
1. Rates and timing for the core with narrow fracture	40
2. Rates and timing for the core with wide fracture	41
PROJECT 3: STEAM WITH ADDITIVES	**57**
3.1 Simulation of Early-Time Response of Single-Well Steam Assisted Gravity Drain (SW-SAGD) (Keith Elliott and A.R. Kovscek)	59
1. Model description	65
2. Description of operating conditions	65
3. Description of simulation cases	65

LIST OF FIGURES

Page

PROJECT 1: FLOW PROPERTIES STUDY 1

1.1 Effects of Temperature on Multiphase Relative Permeability 3
(S. Akin, L.M. Castanier, and W.E. Brigham)

1. Comparison of saturation distributions at different temperatures: top 70°F, middle 122°F, at 0.193 PV injected 8
2. Comparison of JBN derived relative permeabilities to input data for differing temperatures with no initial water saturation 8
3. Comparison of JBN derived relative permeabilities to input data for different temperatures for 40% initial water saturation 9
4. Comparison of history matched relative permeabilities to input data for different temperatures for no initial water saturation 10
5. Schematic diagram of the core holder used in the experiments 11
6. 3-D reconstruction of water saturation distribution at different stages of the Experiment 1 (left 70°F, right top 70°F, middle 122°F, and bottom 150°F) 11
7. Oil saturation distribution at different stages of experiment 1 12
8. Relative permeabilities obtained by automated history matching technique for Experiment 1 12
9. Press and production data fit to Experiment 1 12
10. South Belridge oil/water viscosity ratio temperature chart for Experiment 2 12
11. Planar reconstruction of water saturation distribution at different stages of Experiment 2 (left 70°F, right top 70°F, middle two 122°F and bottom 150°F) 13
12. Oil saturation distribution at different stages of the Experiment 2 13
13. Pressure differential data fit to Experiment 2 13
14. Relative permeabilities obtained by automated history matching technique for Experiment 2 14

1.2.1 Experimental and Theoretical Investigation of Multiphase Flow in Fractured Media 17
(Edgar Rangel-German, S. Akin and L. Castanier)

1. The Core Holder 21
2. Flow system (after Hughes, 1995) 21
3. CT Scan Locations 22
4. Porosity distribution for the experimental system 23
5. CT saturation images for the thin fracture system after 1 hr 30 min of water injection 24
6. CT saturation images for the fracture system after 1 hr 30 min of water injection 24
7. 3-D reconstruction for both systems for $S_w \geq 0.5$ 25

8. Different cases for capillary pressure curves and relative permeability curves for the fracture 26
9. Comparison between experiments and simulations for narrow and wide fracture systems 28

1.2.2SPE 54591: Multiphase-Flow Properties of Fractured Porous Media 31
(Edgar Rangel-German, S. Akin and L. Castanier)
1. Core Holder 34
2. Flow system (after Hughes, 1995) 34
3. Production system (after Hughes, 1995) 35
4. CT scan locations 35
5. Porosity distribution for the experimental system 42
6. CT saturation images for the thin fracture system after 1 hr 30 min of water injection (0.67 PV) 42
7. CT saturation images for the wide fracture system after 1 hr 30 min of water injection (0.67 PV) 42
8. CT saturation images for the narrow fracture system after 2 hr 30 min of oil injection (1.13 PV) 43
9. CT saturation images for the wide fracture system after 2 hr 30 min of oil injection (1.13 PV) 43
10. CT saturation images for the wide fracture system after 16 hours of water injection (7.2 PV) 43
11. CT saturation images for the wide fracture system after 17 hours of water injection (7.7 PV) 44
12. 3-D reconstruction for both systems for water injection 44
13. 3-D reconstruction for both systems for oil injection 45
14. Capillary pressure curves and relative permeability curves for the fracture 45
15. Comparison between experiments and numerical simulations for narrow and wide fracture systems for different PV of water injection 46
16. Comparison between experiments and numerical simulations for narrow and wide fracture systems for different PV of water injection 47

PROJECT 3: STEAM WITH ADDITIVES 57

3.1 Simulation of Early-Time Response of Single-Well Steam Assisted Gravity Drainage (SW-SAGD) 59
(Keith Elliott and A.R. Kovscek)
1. Visual description of the grid system 66
2. Water-oil relative permeability curve 66
3. Gas-liquid relative permeability 67
4. Viscosity/temperature relationship 67
5. Recovery factor vs. time for all cases 67
6. Production and injection rates vs. time 68
7. Well BHP vs. time 68
8. Temperature profile at 100 days 69

9. Well BHP vs. time 69
10. Production and injection rates vs. time 70
11. Temperature profile at 200 days (100 days after SAGD began) 70
12. Production and injection rates vs. time 71
13. Well BHP vs. time 72
14. Temperature profile at 300 days (120 days after SAGD began) 72

3.2 Visualization of Solution Gas Drive in Medium to Heavy Oils (David George) 73
1. SEM of silicon-water micromodel. Features of grain roughness are reproduced with accuracy on the order of 1 μm 81
2. Photograph of the repeated etch pattern on the silicon water 82
3. Top view of the interior of the pressure vessel 84
4. Exploded cross-sectional view of the pressure vessel 85
5. Pressure system 87
6. This image of a micromodel in the pressure vessel exhibits noticeable "ghost" images (200X magnification) 87

3.5 Reservoir Simulation of Foam Displacement Processes (Anthony R. Kovscek) 109
1. Pore-level schematic of a flowing foam 119
2. Gas saturation profiles for unfoamed gas injection into a confined five-spot 119
3. Gas saturation profiles for the simultaneous injection of gas and foamer solution into a confined five-spot 119
4. Foam texture profiles for the simultaneous injection of gas and foamer solution into a confined five-spot 120
5. Surfactant concentration profiles for the simultaneous injection of gas and foamer solution into a confined five-spot 120

PROJECT 4: FORMATION EVALUATION **121**

4.1 A Streamline Approach to Inverse Problems (Yuandong Wang) 123
1. Streamline breakthrough vs. fractional flow 144
2. Comparison on permeability field 145
3. Comparison on breakthrough curve 146
4. Error vs. iterations 147

4.2 Displacement Efficiencies for Direct-Line Drive and Edge-Water Drive-waterflooding Using Streamtube Methods 149
(Amos O. Kehinde)
1(a) Direct-line drive pattern. The dotted line marks out the element of symmetry for the pattern. Aspect ratio is d/a 150
1(b) Staggered-line drive pattern. The dotted line marks out the element of symmetry for the pattern. Aspect ratio is d/a 151
1(c) Five-spot drive pattern. the dotted line marks out the element of symmetry for the pattern. Aspect ratio is always 1 (since $a = d$ by definition 152
1(d) Peripheral or edge water drive (EWD) waterflooding. Most common applications are offshore dripping reservoirs 153
2 Demonstration of mass conservation in fluid flow 158
3 Source-sink geometry 161

ACKNOWLEDGEMENTS

This work was supported by the United States Department of Energy, under contract no. DE-FG22-96BC14994 to Stanford University. Present industrial affiliate members are: Amoco, Arco Exploration and Production, Chevron Petroleum Technology Co., Elf Exploration Production, Exxon, Intevep, Mobil, Texaco, and Total Exploration Production USA, Inc.

SUMMARY

The goal of the Stanford University Petroleum Research Institute is to conduct research directed toward increasing the recovery of heavy oils. Present, SUPRI is working in five main directions:

1. FLOW PROPERTIES STUDIES - To assess the influence of different reservoir conditions (temperature and pressure) on the absolute and relative permeability to oil and water and on capillary pressure.

2. IN-SITU COMBUSTION - To evaluate the effect of different reservoir parameters on the in-situ combustion process. This project includes the study of the kinetics of the reactions.

3. STEAM WITH ADDITIVES - To develop and understand the mechanisms of the process using commercially available surfactants for reduction of gravity override and channeling of steam.

4. FORMATION EVALUATION - To develop and improve techniques of formation evaluation such as tracer tests and pressure transient tests.

5. FIELD SUPPORT SERVICES - To provide technical support for design and monitoring of DOE sponsored or industry initiated field projects.

PROJECT 1: FLOW PROPERTY STUDIES

To assess the influence of different reservoir conditions (temperature and pressure) on the absolute and relative permeability to oil and water and on capillary pressure.

1.1 EFFECT OF TEMPERATURE ON HEAVY OIL/WATER RELATIVE PERMEABILITIES

(Serhat Akin)

1.1 EFFECT OF TEMPERATURE ON HEAVY OIL/WATER RELATIVE PERMEABILITIES

(S. Akin, L.M. Castanier, and W.E. Brigham)

This paper, SPE 54120, was presented at the1999 SPE International Thermal Operations Symposium, March 17-19, 1999, Bakersfield, California.

SPE 54120

Effect of Temperature on Heavy Oil/Water Relative Permeabilities

Serhat Akin, SPE, Middle East Tech. U., Louis M. Castanier and William E. Brigham, SPE, Stanford U.

Copyright 1999, Society of Petroleum Engineers Inc.

This paper was prepared for presentation at the 1999 SPE International Thermal Operations and Heavy Oil Symposium held in Bakersfield, CA, 17-19 March 1999.

This paper was selected for presentation by an SPE Program Committee following review of information contained in an abstract submitted by the author(s). Contents of the paper, as presented, have not been reviewed by the Society of Petroleum Engineers and are subject to correction by the author(s). The material, as presented, does not necessarily reflect any position of the Society of Petroleum Engineers, its officers, or members. Papers presented at SPE meetings are subject to publication review by Editorial Committees of the Society of Petroleum Engineers. Electronic reproduction, distribution, or storage of any part of this paper for commercial purposes without the written consent of the Society of Petroleum Engineers is prohibited. Permission to reproduce in print is restricted to an abstract of not more than 300 words; illustrations may not be copied. The abstract must contain conspicuous acknowledgment of where and by whom the paper was presented. Write Librarian, SPE, P.O. Box 833836, Richardson, TX 75083-3836, U.S.A., fax 01-972-952-9435.

Abstract

In the first part of this study, the accuracy of the JBN technique for the determination of heavy oil/water relative permeabilities, and the effect of temperature on relative permeabilities is examined by giving numerical as well as experimental examples. Using the JBN technique leads to a false temperature dependence of relative permeability curves. In the second part, we present unsteady state relative permeability experiments with initial brine saturation at differing temperatures conducted using South Belridge sand and heavy oil. A new three step experimental technique and an analysis procedure were developed to test the effect of temperature on relative permeabilities. In this technique, an ambient temperature unsteady-state relative permeability run is conducted in the first stage, and following that the temperature is increased twice (i.e. 122°F and 150°F). Two phase saturation profiles along the sand pack are measured using a CT scanner. A commercial black oil simulator, coupled with a global optimization code is then used to estimate two phase relative permeabilities. Experimental saturation profiles, differential pressure and recovery data collected from both the ambient and higher temperature data are used in the numerical model. It has been observed that a single set of relative permeability curves can represent both the ambient and high temperature parts of the experiment. This suggests that relative permeability is not a function of temperature at least for the system tested.

Introduction

For modeling thermal recovery processes for heavy oil recovery, one needs to know not only the relative permeabilities at the original reservoir temperature but also the effect of increasing temperature on the relative permeability curves. Over the past three decades, a number of experimental studies have reported contradictory temperature effects on two-phase relative permeabilities as well as residual oil saturations in porous media. Although a number of studies have reported significant effects no consensus has emerged on the generality of such effects or on possible mechanisms causing such effects. Therefore this study aims to determine the effect of temperature on relative permeability curves for a reservoir sand/ heavy-oil/ NaBr water system and to examine the use of unsteady-state relative permeability estimation techniques in such systems.

Edmondson[1] found a reduction in residual oil saturation in Berea cores as the temperature increased. Using refined oils and an unsteady state experimental technique, he noted that the relative permeability ratio of oil to water shifted toward a higher water saturation as the temperature increased.

Poston et al.[2] investigated the effects of temperature on unconsolidated sand using refined oils. They reported that irreducible water saturation increased, and the residual oil saturation decreased with increasing temperature. Moreover, they concluded that relative permeabilities to both oil and water increased with increasing temperature.

Contradicting previous researchers, two studies[3,4] have reported temperature independent relative permeability data obtained from unsteady state experiments in unconsolidated and Berea sandstone cores using refined oils. Miller and Ramey[4] noted various artifacts, such as; material balance errors, viscous instability, clay migration, wettability alteration by miscible cleaning methods, and capillary pressure end effects, that may have affected former conclusions on the effect of temperature on relative permeability data.

Closmann et al.[5] used the steady state technique to measure altered, unaltered and de-asphalted tar and brine relative permeabilities at elevated temperature using previously frozen Peace River cores. They concluded that, at higher temperatures, tar and water relative permeability curves shifted toward lower water saturations.

Maini and Batcyky[6] conducted unsteady state experiments at temperatures ranging from room temperature to 522°F using a previously frozen core from a heavy oil reservoir, and stock tank oil and formation brine from the same reservoir. They measured the absolute permeability to formation brine using a transient pressure decay test, and used history-matching calculations to obtain relative permeabilities. They concluded

that, irreducible water saturation increased and residual oil saturation decreased with increasing temperature up to a temperature limit. Moreover, they reported that relative permeability to oil decreased, and relative permeability to brine remained unchanged with increasing temperature.

Polikar et al.[7] used the steady state technique to measure the relative permeability of Athabasca bitumen using unconsolidated Ottawa sand as the porous medium. Their results showed no significant effect of temperature on relative permeability and saturation data up to 392°F.

Maini and Okazawa[8] analyzed unsteady state experiments conducted on an unconsolidated silica sand using Bodo stock tank oil and de-ionized water. They history matched production and differential pressure data to obtain relative permeability curves. They concluded that the most reliable data they obtained were at residual oil saturation after three pore volumes injected. They observed increasing relative permeability to water with increasing temperature.

Unlike the previous researchers, Watson and Ertekin[9] studied the effect of temperature gradient on relative permeability measurements using the steady state technique. They found that different temperature gradients caused differences in both irreducible water saturations and residual oil saturations. These data suggested that the fired Berea cores become increasingly water-wet, and unfired cores become increasingly oil wet, during imbibition and drainage. Moreover, they concluded that relative permeabilities to both oil and water decreased with increasing temperature. They also observed that the absolute water permeabilities of fired Berea sandstone cores were unaffected by temperature.

Polikar et al.[10] conducted both steady state and unsteady-state relative permeability experiments to find out the effect of temperature on relative permeability. Using Athabasca bitumen and deionized water, they used the JBN[11] technique to analyze their results. They observed no significant temperature effects on relative permeability of either phase, nor in the residual oil and irreducible water saturations. They attributed the small changes seen to core heterogeneity. Moreover, they reported that steady state and unsteady-state techniques resulted in similar relative permeability curves.

More recently, Muqeem et al.[12] conducted steady state two phase and three phase relative permeability experiments at 167°F and 257°F (75°C and 125°C) using an unconsolidated silica sand with refined oil, brine and nitrogen gas. The measured relative permeabilities showed no significant temperature effect.

Table 1 - A Summary Of The Recent Experimental Investigations Of Temperature Effects On Relative Permeability.

Ref.	*Technique*	*Fluids*	*Core*	*Temperature Range*	*Saturation Measurement*	*End-Point Saturation*	*Relative Permeability*
1	Unsteady State (Welge)	Refined Oils (No 5 & 15)	Berea (1382°F)	room-500°F	graduated cylinders	$S_{or}\downarrow T\uparrow$ -	k_{rw} shifted to lower S_w
3	Unsteady State (JBN)	Refined Oil	Unconsolidated Ottawa (170-200)	room-250°F	photo cell + frequency counter	independent	independent
4	Unsteady State (JBN)	Refined Oil (Blandol)	Unconsolidated Ottawa (100-200) + Berea (932°F)	room-300°F	separator + graduated cylinders	independent	independent
5	Steady State	Altered-unaltered-deasphalted tar	Frozen Peace River Cores	385°F	electrical resistance	not presented	k_{rw} shifted to lower S_w
6	Unsteady State (History Matching)	Stock Tank Oil	Frozen Core from a Hvy Oil Res	room-522°F	separator + fractional collector	$S_{wirr}\uparrow T\uparrow$ $S_{or}\downarrow T\uparrow$	$k_{ro}\downarrow T\uparrow$ $k_{rw}\rightarrow T\uparrow$
7	Steady State	Athabasca Bitumen	Unconsolidated Ottawa (~200)	room-482°F	material balance	independent	independent
8	Unsteady State (History Matching)	Bodo Stock Tank Oil+3.5% ether	Unconsolidated Silica Sand (140-170)	room-392°F	separator + fractional collector	not presented	$k_{rw}\uparrow T\uparrow$ $k_{ro}\downarrow\uparrow T\uparrow$
10	Steady State	Refined Oil (Soltrol 170)	Berea (1832°F) + unfired	room-300°F	material balance	$S_{wirr}\uparrow T\uparrow$	k_{ro}, $k_{rw}\downarrow T\uparrow$
11	Steady & Unsteady State (JBN)	Athabasca Bitumen	Unconsolidated Silica Sand (170-230)	212°F-482°F	material balance	independent	independent
12	Steady State	Refined Oil+N2	Unconsolidated Silica Sand (140-200)	167°F&257°F	separator	not presented	independent
13	Unsteady State (JBN)	SJV Oil-GulfLight + SJV	Unconsolidated preserved cores + Berea (925°F)	room-300°F	graduated cylinders	independent	k_{rw} shifted to lower S_w

Kumar and Inouye[13] used the JBN technique to analyze unsteady state relative permeability experiments conducted at differing temperatures. They tried to obtain low temperature analogues to high temperature relative permeability data. They concluded that relative permeability data obtained at ambient conditions can be used for high temperatures as long as the viscosity ratios and the wettabilities were similar. They also reported that residual oil saturation and irreducible water saturation are independent of temperature and are a function of viscosity ratio.

The results obtained from the aforementioned studies are summarized in Table 1. It can be observed that there is no conclusive agreement on the effect of temperature on oil/water relative permeabilities. Although some studies show an effect of temperature, others disagree with that by attributing changes observed to viscous instabilities and to other experimental errors. Basically, the reasons for divergence of experimental data may be summarized as follows:

1. Errors in saturation measurements.
2. Errors caused by neglect of capillary pressure end effects.
3. Wettability variations with differing oils, and brines.
4. Assumptions made to relate experimental procedures and/or calculations.
5. Inadequacy of mathematical models used to represent multiphase flow conditions.

It is clear that, unless the problems stated above are overcome, a better understanding of the effects of temperature on relative permeabilities will not be achieved. In the first part of this study, the accuracy of the JBN technique for the determination of heavy oil/water relative permeabilities and its implication on the effect of temperature on relative permeabilities is discussed by giving numerical as well as experimental examples. In the second part of the study, a new experimental technique is presented to tackle the effect of the temperature problem in a qualitative manner. In this technique, an ambient temperature unsteady-state relative permeability run is conducted in the first stage, and following that, the temperature is increased twice (i.e. 122°F and 150°F). Two phase saturation profiles along the sand pack are measured using a CT scanner. A commercial black oil simulator, coupled with a global optimization code is then used to estimate two phase relative permeabilities. It has been observed that a single set of relative permeability curves can represent both the ambient and high temperature parts of the experiment. This suggests that relative permeability is not a function of temperature at least over the temperature range studied on the system tested.

Application of the Unsteady-State Relative Permeability Estimation Technique to Heavy Oil Systems

Most of the parameters used in thermal simulations are obtained from laboratory measurements. For instance, water/oil relative permeability curves are determined from corefloods involving formation brine and oil. There is, however, uncertainty associated with this type of data since the high viscosity of heavy oils makes the measurement difficult, and the unspecified heterogeneity of the core material complicates flow paths and saturation distributions.. The principal objective of this section is to examine whether or not a Buckley-Leverett type displacement model (i.e. JBN technique) could be used to describe the behavior of such unstable displacements. Another purpose is to find out what happens if such a technique is used to estimate oil/water relative permeabilities. To achieve this goal, several hypothetical, unstable and immiscible displacements corresponding to experiments conducted at different temperatures were simulated using a commercial simulator. The level of instability in these experiments was quantified by a dimensionless stability number, N_{is} proposed by Peters and Flock[14].

$$N_{is} = \frac{(M-1)(V-V_c)\mu_w d^2}{N_w k_{wor} \sigma}$$

According to Peters and Flock, a core-flood will be stable (piston-like displacement, and no viscous fingering) if the dimensionless stability number is less than 13.56. The properties of the porous medium and the fluids used in the hypothetical experiments as well as the stability numbers for no initial water saturation are presented in Tables 2 and 3. It can be observed that even at high temperatures, these core-floods are highly unstable showing significant viscous fingering. However, capillary end effects were kept at a minimum as the scaling coefficients proposed by Rapoport and Leas[15] were higher than the critical value (i.e. L u μ_w, ft-ft/s-cp is greater than 3.5) for all experiments.

A commercial black oil simulator, ECLIPSE[16], was used to simulate the experimental conditions given in Table 2. Three dimensional, radial geometry was used to simulate the experiments. To account for viscous fingers, center grids had smaller diameter increments compared to the outer ones . The first and last grid planes in the z direction had higher transmissibility compared to other grids to reproduce the experimental inlet and outlet lines together with spider-web shaped end plates. Production and pressure differential history across the core were collected. Unsteady-state relative permeabilities were then computed by applying the JBN technique[11] using the equations given below:

$$f_o = \frac{1}{1+\frac{k_{rw}\mu_o}{k_{ro}\mu_w}} = \frac{dN_p}{dW_i}$$

$$S_{w2} = S_{wi} + N_p - W_i f_o$$

Table 2 - Properties Of Porous Medium And Fluids Used For Hypothetical Experiments.

Porous Medium	Fluid Properties
	Oil
Permeability = 5.3 Darcies	Viscosity @°70 F=220 cp
Porosity = 0.394	Density @°70 F=0.878 gm/cc
Length = 17.8 cm	Water
Diameter = 2.54 cm	Viscosity at °70 F = 0.97 cp
	Density at °70 F = 1.00 gm/cc

Table 3 - Stability Numbers For Different Experiments With No Initial Water Saturation.

Experiment	1	2	3
Temperature, °F	70	122	150
Stability Number	40167	6650	3174
Rapoport & Leas Number	14.21	7.82	5.97

Figure 1 gives the comparison of the saturation distributions at 0.193PV of water injected obtained from simulations along the hypothetical core (L=17.8 cm) at three different temperatures (70, 122 and 150°F) and at four different locations with a zero initial water saturation. It can be observed that the front is not stable, and moreover, a fingering pattern is visible in the center of the core for all cases. Note that the same set of relative permeability curves was used to generate these data.

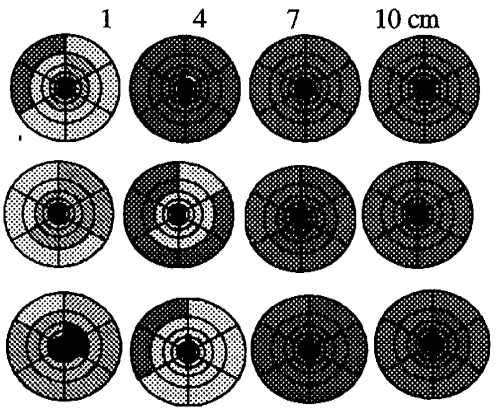

Fig.1- Comparison of saturation distributions at different temperatures: top 70°F, middle 122°F, bottom 150°F, at 0.193 PV injected.

The relative permeability curves obtained using JBN analysis for no initial water saturation are compared to the input curves in Fig 2. Notice that although the same relative permeability curves were used to simulate core-floods at different temperatures, different apparent relative permeability curves were obtained using the JBN technique. Interestingly, the resulting relative permeability curves show a false temperature dependence. That is to say, there is a considerable increase in the calculated relative permeability to oil and water at a constant saturation as temperature increases. The end point oil saturation also decreases and the corresponding water relative permeability increases as temperature increases as observed in Table 4. This false temperature dependence agrees with the general trend that oil and water relative permeability curves shift to the right as reported in studies by Sinnokrot[17], Weinbrandt et al.[18], and others[5,6]. Moreover, these false findings agree with the concept of decreased residual oil saturation with a temperature increase.

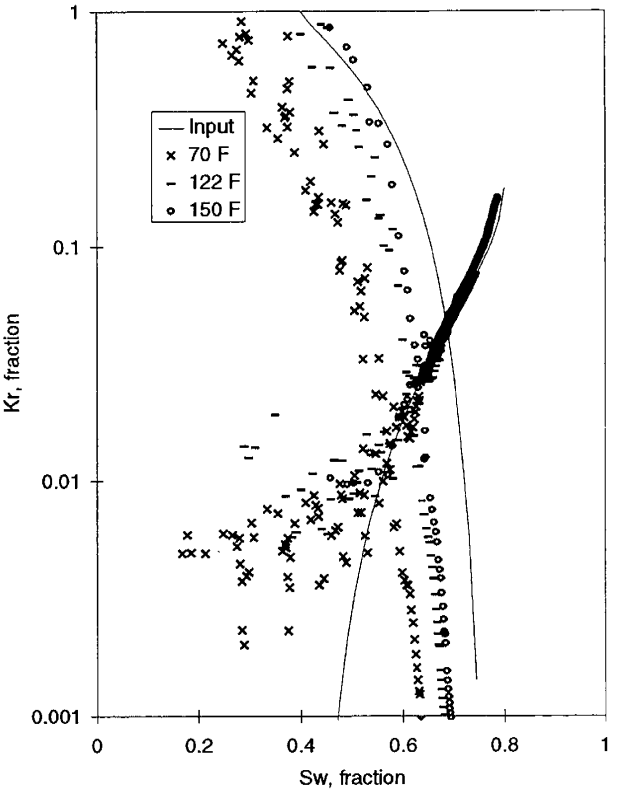

Fig. 2- Comparison of JBN derived relative permeabilities to input data for differing temperatures with no initial water saturation.

Table 4 - End Point Oil Saturation And Relative Permeability To Water At Different Temperatures Without Initial Water Saturation.

Temperature (°F)	Sor	Krw
70	0.292	0.0538
122	0.255	0.0764
150	0.212	0.161
input	0.200	0.172

Three similar hypothetical experiments were simulated to see the effect of initial water saturation. The stability numbers were much smaller compared to the no initial water saturation case, but still indicated unstable displacements as observed in Table 5. In these cases, the calculated relative permeability curves showed similar false temperature effects, and also failed to find the input relative permeability curves as shown in Fig 3; the differences were somewhat smaller for oil relative permeabilities but larger for water relative permeabilities. Similar to the no initial water saturation cases, the calculated residual oil saturation decreased as temperature increased as observed in Table 6.

Table 5 - Stability Numbers For Different Experiments With Initial Water Saturation.

Experiment	1	2	3
Temperature, °F	70	122	150
Stability Number	582.3	96.4	46
Rapoport & Leas Number	14.21	7.82	5.97

Table 6 - End Point Oil Saturation And Relative Permeability To Water At Different Temperatures With Initial Water Saturation.

Temperature (°F)	S_{or}	K_{rw}
70	0.281	0.0684
122	0.244	0.0995
150	0.204	0.2119
input	0.200	0.172

Another common technique used to estimate relative permeability curves is one dimensional history matching. To estimate relative permeability curves with the history matching or parameter estimation approach, an objective function as shown below, is constructed as a weighted sum of squared differences between the measured data and calculations from a one-dimensional mathematical model of the experiment.

$$J = \left.\begin{aligned} &\sum_{i=1}^{N} W_{pi}\left(\Delta P_i^{obs} - \Delta P_i^{cal}\right)^2 + \\ &\sum_{i=1}^{N} W_{qi}\left(Q_{ti}^{obs} - Q_{ti}^{cal}\right)^2 + \\ &\sum_{k=1}^{M}\sum_{i=1}^{N} W_{si}\left(S_{i,k}^{obs} - S_{i,k}^{cal}\right)^2 \end{aligned}\right\}$$

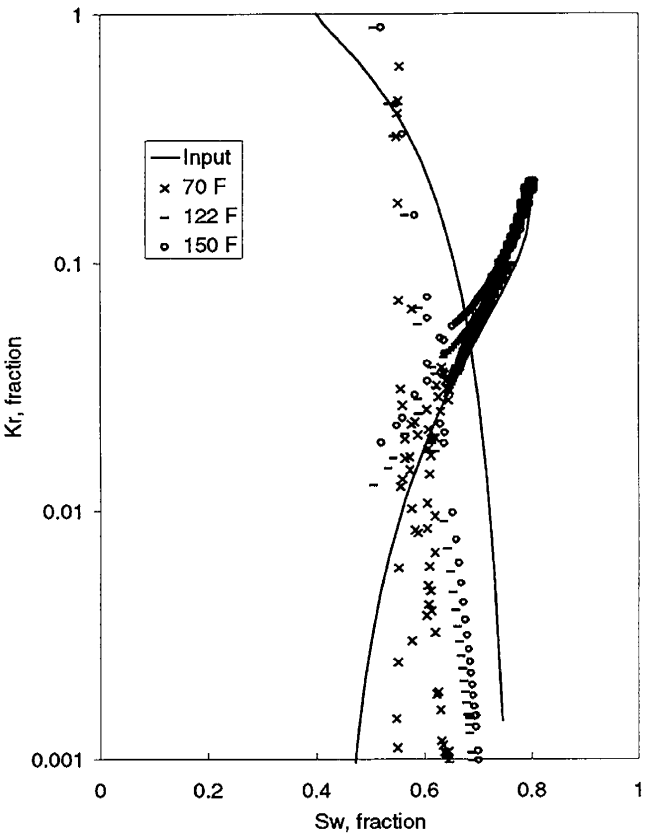

Fig. 3- Comparison of JBN derived relative permeabilities to input data for different temperatures for 40% initial water saturation.

For a typical displacement experiment, the measured data might consist of a set of pressure drops across the core, the recovery histories of the displaced phase, and if available the internal saturation profiles[19].

By using a one dimensional radial grid definition, the same hypothetical, aforementioned data for no initial water saturation was used to generate relative permeability curves by

matching the pressure and production response for differing temperatures. Figure 4 compares the estimated relative permeability curves with the input data. As the temperature increased, oil relative permeability increased and water relative permeability decreased at the same saturation. Therefore, it can be concluded that one dimensional history matching is also showing a false temperature effect.

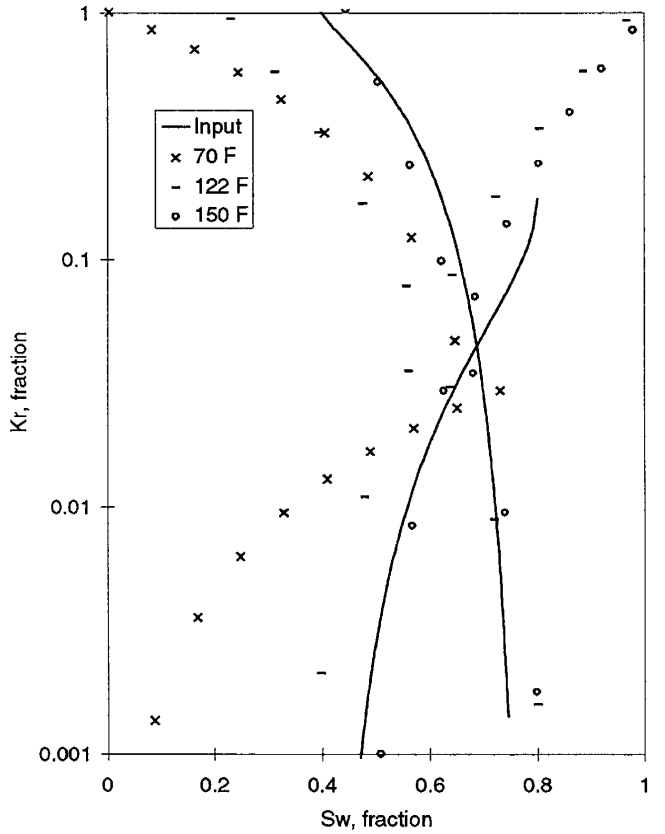

Fig. 4- Comparison of history matched relative permeabilities to input data for different temperatures for no initial water saturation.

The above findings clearly show that JBN, and like techniques can lead to erroneous results. It seems that the viscous instability effects get smaller if the core is initially at residual water saturation. Another important finding is that because of viscous instabilities, the JBN technique also leads to a false temperature effect regardless of initial water saturation.

A possible, alternative solution to the problem of finding the effect of temperature on heavy-oil/water relative permeabilities is to introduce a new experimental technique that consists of three different parts. In the first part, a conventional oil/water relative permeability experiment is conducted until no more oil is produced. Following that the temperature is increased twice, and at each of these higher temperatures injection is continued until residual oil saturation. The pressure, saturation and production data collected during the ambient part of the experiment is used to calculate heavy oil/water relative permeability curves using the aforementioned history matching procedure. Then, using these relative permeability curves, the rest of the experiment (i.e. higher temperature parts) is simulated and compared to experimental data. There are two possible outcomes of this procedure:

1. Both parts of the data (i.e. cold and hot) are matched by using only one set of relative permeability curves, which would indicate that the flow functions do not depend on temperature.
2. The algorithm fails to represent both parts of the experimental data (i.e. cold and hot) using a single set of relative permeability curves, which would indicate that the flow functions depend on temperature.

This technique provides a qualitative result to the effect of temperature on oil/water relative permeabilities. Yet, at the same time the higher temperature parts of the experiment provide some quantitative information on the residual oil saturation and end point relative permeabilities.

Results and Discussion

Two different sets of experiments were conducted using the proposed experimental procedure and analysis. In the first set of experiments, clean Ottawa sand and a high viscosity mineral oil were used. Table 7 gives the properties of the porous medium and the fluids used in these experiments. Since high temperature relative permeability experiments require core holders and sleeves that can withstand high temperature and pressure, a core holder was designed that consists of an aluminum outer shell with internal adjustable centralizers which hold and centralize an aluminum core sleeve (1 3/4 in ID, and 16 in long) as shown in Fig 5. The core sleeve can operate safely up to 482°F and 1000 psi. With its current design the core holder is suitable for CT monitored high temperature experiments using a heating circulator for the annulus.

Table 7 - Properties Of The Sand And Fluids Used In The First Set Of Experiments.

Porous Medium	***Fluid Properties***
Ottawa Sand (mesh 100-200)	*Mineral Oil (Kaydol)*
Permeability = 5.3 Darcies	Viscosity @ 70°F=220 cp
Porosity = 0.31%	Density @ 70°F=0.878 gm/cc
Length = 40.64 cm	*Water (8% weight KBr)*
Diameter = 4.445 cm	Viscosity at 70°F=1.075 cp
	Density at 70°F=1.05 gm/cc

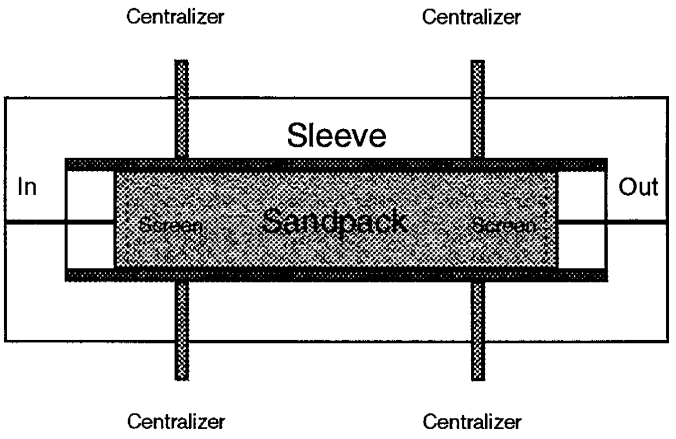

Fig. 5- Schematic diagram of the core holder used in the experiments.

Following the aforementioned procedure a displacement experiment was conducted with initial water saturation. The first part of the experiment was performed at room temperature and then the temperature was increased to 122°F and, then to 150°F. CT scans were taken to monitor saturation changes at differing times. Figure 6 displays 3D re-constructions of water saturation distributions at different stages of the experiment at differing temperatures. The left column of this figure gives images taken at 0.606, 1.01, 6.06, and 8.33 pore volumes of water injected from the ambient temperature part of the experiment. It can be observed that, because of the high viscosity ratio, water fingers were formed and the flood front was not stable. The effect of temperature is presented at the right column of the same figure. As can be seen, average water saturation does not change much. Figure 7 shows average oil saturation profiles obtained by averaging CT derived saturations plotted at differing times. It can be noticed that temperature increase has a minimal affect on the end point saturations. We can say that residual oil saturation is independent of temperature. Following that, a nonlinear optimization code[19] coupled with a commercial simulator[16] in 2-D radial mode was used to history match the ambient part of the experimental data in a least squares manner and the relative permeability curves presented in Fig 8 were obtained. Figure 9 gives pressure differential and production data fits to all parts of the experiment using these curves. It can be observed that the experiment can be modeled using the relative permeability curves obtained from the cold part. This indicates that heavy oil/water relative permeabilities do not depend on temperature for the system in consideration at this temperature range.

Variations in capillary pressure and relative permeability with temperature may be expected for a rock/fluid system whose wettability is temperature dependent. Sinnokrot et al.[17] discussed that relative permeabilities and capillary pressures may exhibit temperature dependence for systems whose fluids contain large concentrations of wettability altering compounds like asphaltenes. To check such a possibility another experiment with initial water saturation was conducted using South Belridge sand and oil. This field was selected since it is a major target for thermal recovery operations like steam flooding and in-situ combustion[20]. Table 8 gives the properties of the porous medium and the fluids used in the experiment. The sand was packed without cleaning to preserve the original wettability. The initial temperature of the experiment was kept at the reservoir temperature of 95°F (35°C)[20] to have a reasonable starting viscosity ratio as observed in Fig 10. The rest of the experimental procedure was similar to the previous one such that the temperature was increased to 122°F and, then to 150°F after the initial part. However, because of experimental difficulties water injection at higher temperatures was not continued down to residual oil saturation.

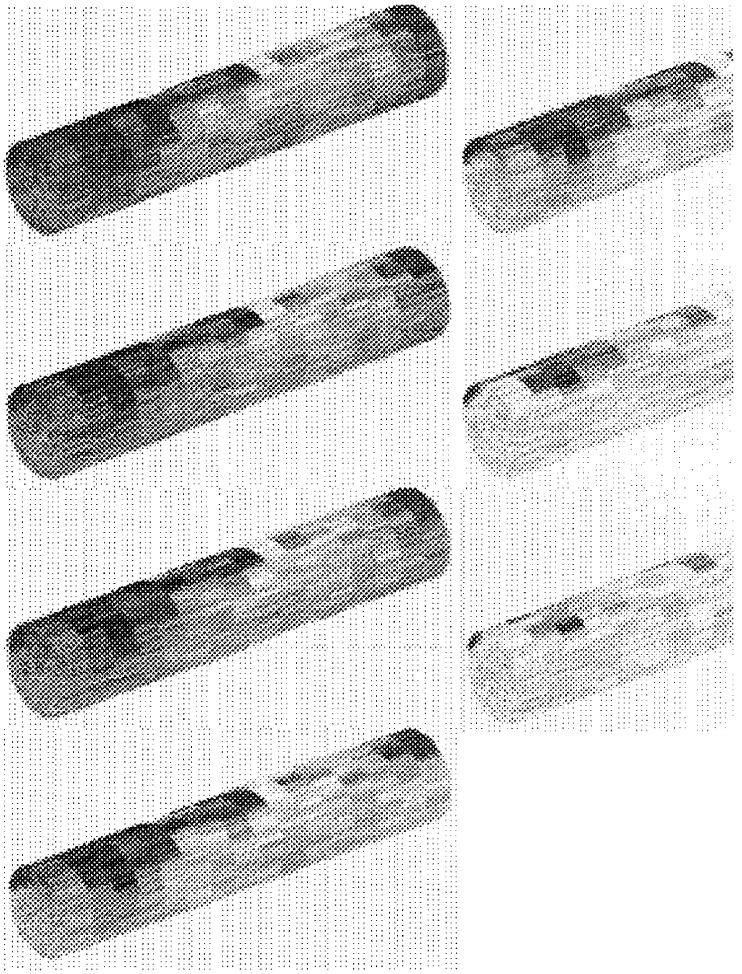

Fig. 6- 3-D reconstruction of water saturation distribution at different stages of the experiment 1 (Left 70°F, right top 70°F, middle 122°F and bottom 150°F).

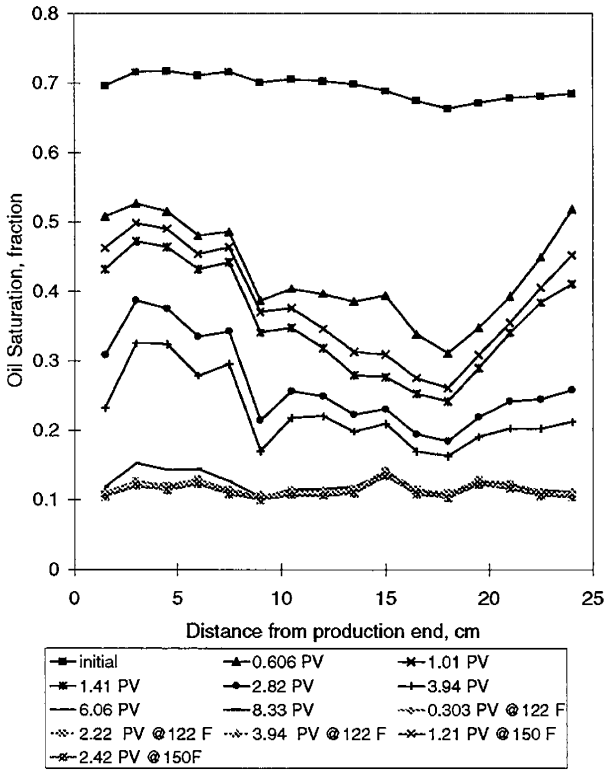

Fig. 7- Oil saturation distribution at different stages of Experiment 1.

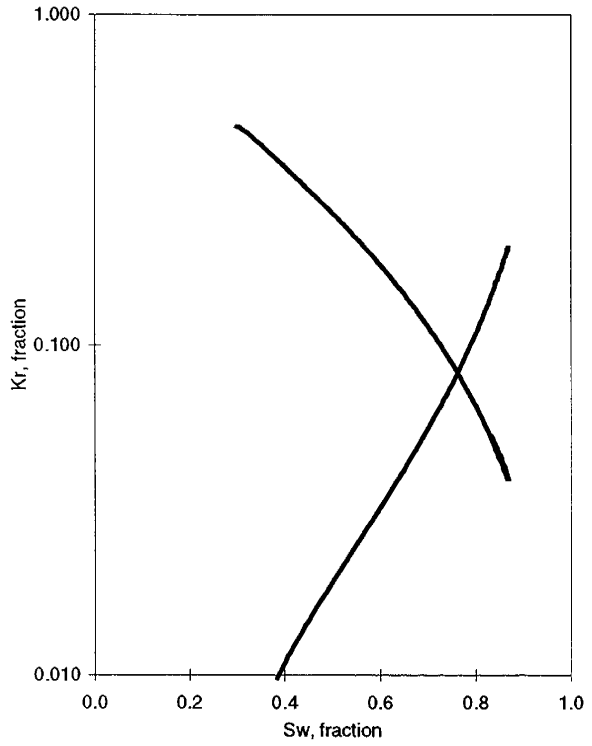

Fig. 8- Relative permeabilities obtained by automated history matching technique for Experiment 1.

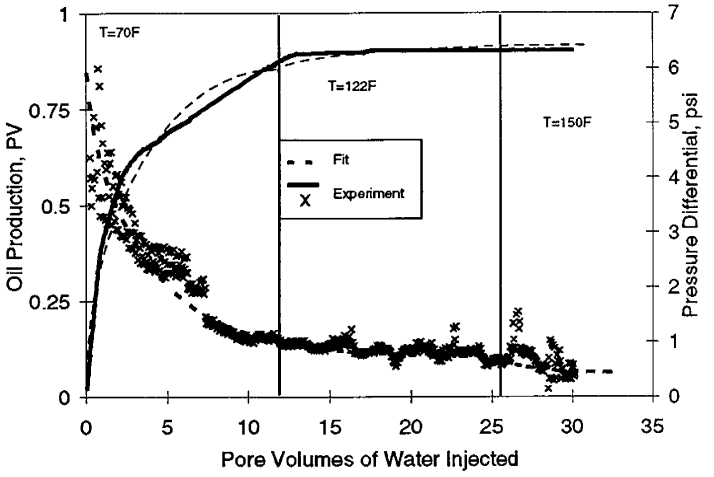

Fig. 9- Pressure and production data fit to Experiment 1.

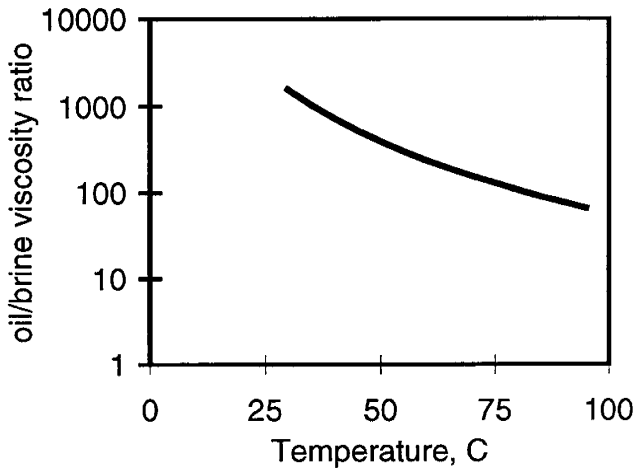

Fig. 10- South Belridge oil/water viscosity ratio temperature chart for Experiment 2.

Figure 11 gives re-constructions of the water saturation profiles obtained using the CT scan images. A higher level of instability is apparent compared to the previous experiment because of the high viscosity ratio. Compared to the previous experiment the effect of temperature is much greater as can also be observed from the average saturation profiles plotted in Fig 12. This was due to the short duration of each hot part of the experiment. However, a nice match was obtained to experimental pressure data shown in Fig 13 using the relative permeability curves presented in Fig 14 which is based on the cold temperature match. Therefore, it was concluded that relative permeability is not a function of temperature at least for the systems presented and for the temperature range studied. It also appears that wettability alteration is not an important factor at this temperature level. Further study at higher temperatures is required.

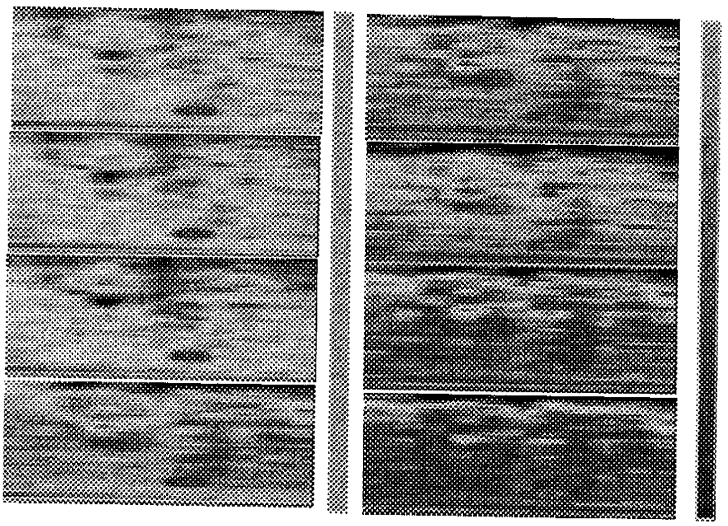

Fig. 11- Planar reconstruction of water saturation distribution at different stages of the Experiment 2 (Left 70°F, right top 70°F, middle two 122°F and bottom 150°F).

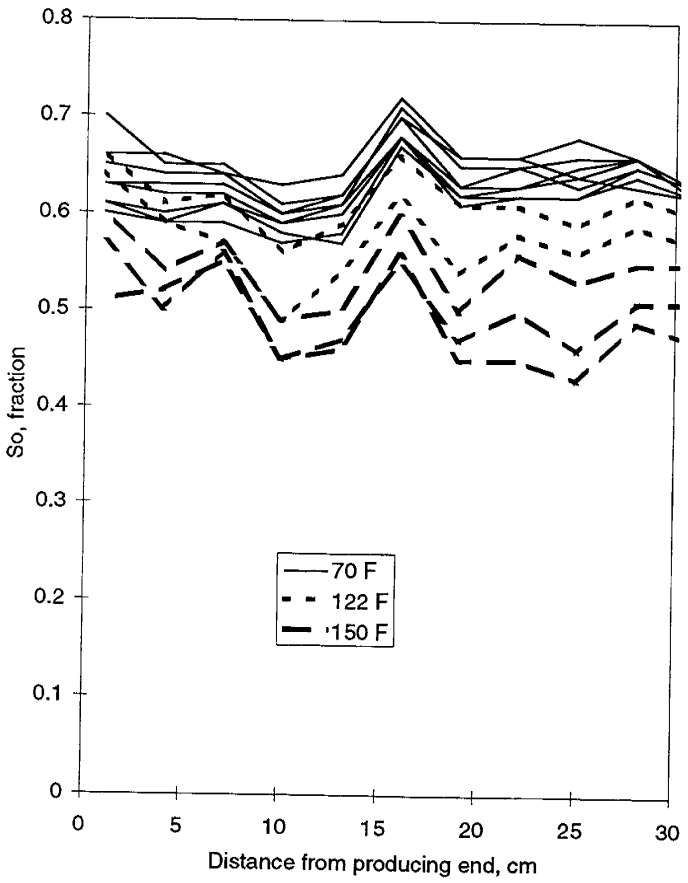

Fig. 12- Oil saturation distribution at different stages of the Experiment 2.

Figure 11 gives re-constructions of the water saturation profiles obtained using the CT scan images. A higher level of instability is apparent compared to the previous experiment because of the high viscosity ratio. Compared to the previous experiment the effect of temperature is much greater as can also be observed from the average saturation profiles plotted in Fig 12. This was due to the short duration of each hot part of the experiment. However, a nice match was obtained to experimental pressure data shown in Fig 13 using the relative permeability curves presented in Fig 14 which is based on the cold temperature match. Therefore, it was concluded that relative permeability is not a function of temperature at least for the systems presented and for the temperature range studied. It also appears that wettability alteration is not an important factor at this temperature level. Further study at higher temperatures is required.

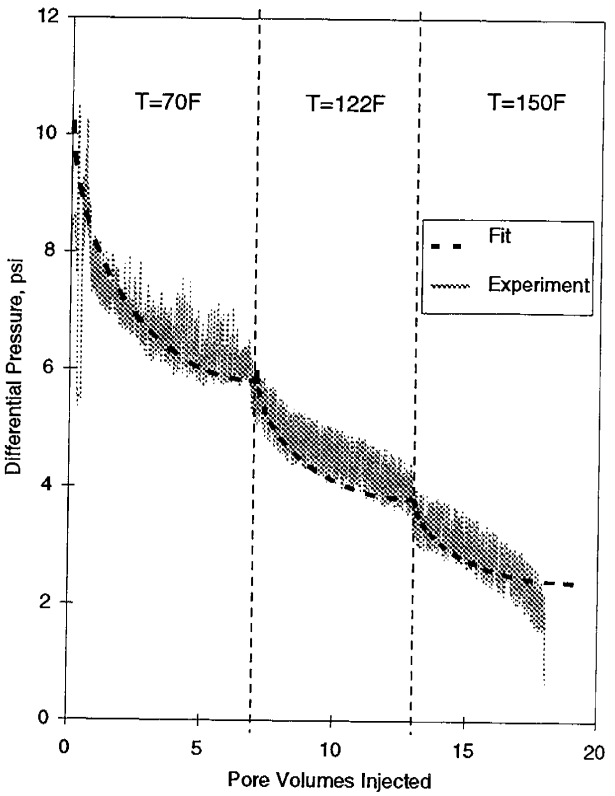

Fig. 13- Pressure differential data fit to Experiment 2.

Conclusions

Based on hypothetical heavy-oil/water numerical simulations it was observed that the use of the JBN technique for the estimation of heavy-oil/water relative permeabilities leads to erroneous results and a false temperature effect A new experimental technique is presented to tackle the problem of the effect of temperature on oil/water relative permeability. It was found that temperature does not have any effect on the relative permeabilities for the systems and temperatures used in this study. These findings show that previously observed

apparent temperature dependence of endpoint saturations and relative permeabilities is basically caused by a decrease in the oil/water viscosity ratio with temperature.

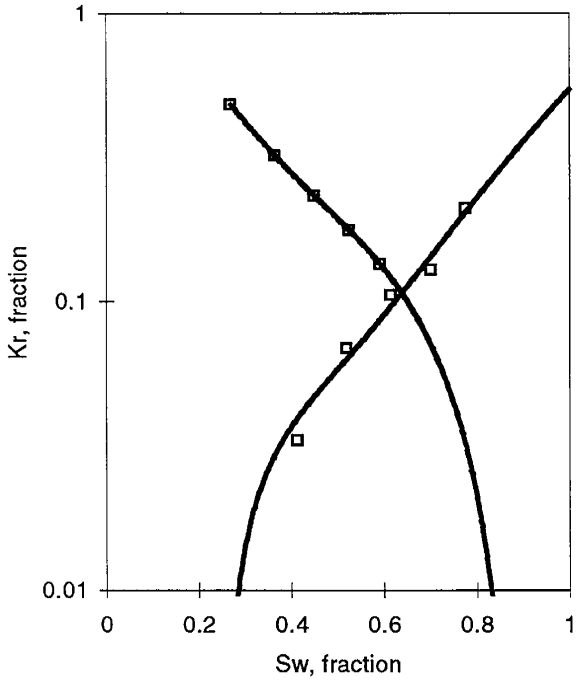

Fig. 14- Relative permeabilities obtained by automated history matching technique for Experiment 2.

Acknowledgments

This work is supported by SUPRI A industrial affiliates and the Department of Energy under contract DE FG 22-96 BC 14994. We would like to thank to Dr. Nizar Djabbarah for his suggestions and discussion.

Nomenclature

d = Core diameter, ft.
f = Fractional flow, fraction
g = Gravitational acceleration
k = Relative permeability, fraction
u = Darcy velocity, ft/sec
I_r = Relative injectivity, fraction
J = Objective function
M = Mobility ratio or number of grids
N = Number of data points
N_p = Production, PV
N_w = Wettability number, dimensionless
Q = Volume of displaced phase recovered, PV
Δp = Pressure differential across the core, psi
S = Saturation, fraction
V_c = Characteristic velocity, ft/sec
W = Injection, PV or weighing factor
μ = Viscosity, cp
ρ = Density, lb/ft^3
σ = Oil-water interfacial tension, dyne/cm

Subscripts and superscripts

cal = Calculated
i, j, k = Indices
o = Oil
obs = Observed
or = Residual oil
p = Produced
w = Water
w2 = End point

References

1. Edmondson, T. A.: "Effect of Temperature on Waterflooding," J. Cdn. Pet. Tech. (Oct. - Dec. 1965) 236-42.
2. Poston, S. W., Israel, S., Hossain, A. K. M. S., Montgomery III, E. F. and Ramey, H. J. Jr.: "The Effect of Temperature on Irreducible Water Saturation and Relative Permeability of Unconsolidated Sands," Soc. Pet. Eng. J. (June, 1970) 171-180.
3. Sufi A. H., Ramey, H. J. Jr., and Brigham, W. E.: "Temperature Effects on Relative Permeabilities of Oil-Water," paper SPE 11071 presented at 57th Annual Fall Technical Conference and Exhibition of Society of Petroleum Engineers held in New Orleans, USA, Sept. 26-29, 1982.
4. Miller, M. A., and Ramey, H. J. Jr.: "Effect of Temperature on Oil/Water Relative Permeabilities of Unconsolidated and Consolidated Sands," JPT (Dec. 1985) 945-953.
5. Closmann, P. J., Waxman, M. H., and Deeds, C. T.: "Steady-State Tar/Water Relative Permeabilities in Peace River Cores at Elevated Temperature," paper SPE 14227 presented at 60th Annual Technical Conference and Exhibition of Society of Petroleum Engineers held in Las Vegas, USA, Sept. 22-25, 1985.
6. Maini, B. B., and Batycky, J. P.: "Effect of Temperature on Heavy-Oil/Water Relative Permeabilities and Vertically Drilled Core Plugs," JPT (Aug. 1985) 1500-1510.
7. Polikar, M., Ferracuti, F., Decastro, V., Puttagunta, V. R., and Ali, F. S. M.: 'Effect of Temperature on Bitumen-Water End Point Relative Permeabilities and Saturations," J. Cdn. Pet. Tech. (Sep. - Oct. 1986) 44-50.
8. Maini, B. B., and Okazawa, T.: "Effect of Temperature on Heavy Oil-Water Relative Permeability of Sand," J. Cdn. Pet. Tech. (May - June 1987) 33-41.
9. Watson, R. W., and Ertekin, T.: "The Effect of Steep Temperature Gradient on Relative Permeability Measurements,' paper SPE 17505 presented at the SPE Rocky Mountain Regional Meeting held in Casper, WY, USA, May 11-13, 1988.

10. Polikar, M., Ali, F. S. M., and Puttagunta, V. R.: 'High Temperature Relative Permeabilities for Athabasca Oil Sands," SPE Res. Eng. (Feb. 1990) 25-32.
11. Johnson, E.F., Bossler, D. P., and Naumann, V. O. :"Calculation of Relative Permeability From Displacement Experiments," Trans. AIME (1959) 216, 61-63.
12. Muqeem, M., Bentsen, R., and Maini, B.: "Effect of Temperature on Three-Phase Water-Oil-Gas Relative Permeabilities of Unconsolidated Sands," paper 5593-03 presented at the 5th Petroleum Conference of the South Saskatchewan Section, the Petroleum Society of CIM, held in Regina, Canada, Oct. 18-20, 1993.
13. Kumar, M., and Inouye, T. A.: "Low-Temperature Analogs of High-Temperature Water/Oil Relative Permeabilities," paper SPE 28616 presented at 69th Annual Technical Conference and Exhibition of Society of Petroleum Engineers held in New Orleans, USA, Sept. 25-28, 1994.
14. Peters, E.J. and Flock, D.L. :"The Onset of Instability During Two-Phase Immiscible Displacement in Porous Media" Soc. Pet. Eng. J.(April, 1981) 249-258.
15. Rapoport, L. A., and Leas, W. J.: "Properties of Linear Waterfloods," J. Pet. Tech. (May 1953) 139-48.
16. Eclipse Reference Manual, Intera Information Technologies Ltd., Oxfordshire, England, 1995.
17. Sinnokrot, A.A., Ramey, H.J.Jr., and Marsden, S.S,Jr. :"Effect of Temperature Level upon Capillary Pressure Curves," Soc. Pet. Eng. J. (March 1971) 13-22.
18. Weinbrandt, R.M., Ramey, H.J.Jr., and Casse, F.J. :"The Effect of Temperature on Relative and Absolute Permeability of Sandstones," Soc. Pet. Eng. J. (Oct. 1975) 376-84.
19. Akin, S. : "Application of Computerized Tomography to the Determination of Three Phase Relative Permeabilities," Ph.D. dissertation, Middle East Technical University, Ankara, Turkey, Jan 1997.
20. Ramey, H. J Jr., Stamp, VW, Pebdani, FN and Mallinson, JE :"Case History of South Belridge, California, In-Situ Combustion Oil Recovery," paper SPE/DOE 24200 presented at the SPE/DOE Eighth Symposium on Enhanced Oil Recovery held in Tulsa, Oklahoma, April 22-24, 1992.

1.2 EXPERIMENTAL AND THEORETICAL INVESTIGATION OF MULTIPHASE FLOW IN FRACTURED MEDIA

(Edgar Rangel-German)

1.2.1 EXPERIMENTAL AND THEORETICAL INVESTIGATION OF MULTIPHASE FLOW IN FRACTURED MEDIA

(Edgar Rangel-German, Serhat Akin, and Louis M. Castanier)

This paper was presented at the 1998 Geothermal Resource Congress held in San Diego, California (September 1998).

Experimental and Theoretical Investigation of Multiphase Flow in Fractured Media

E. Rangel-German, S. Akin and L. Castanier
Petroleum Engineering Department, Stanford University

ABSTRACT

A laboratory flow apparatus was built to obtain data on water-air displacements in horizontal single-fractured block systems. For this purpose, two configurations have been used: a two matrix-block system with a 1mm spacer between the blocks, and a two matrix-block system with no spacer. During the experiments, porosity and saturation calculations along the cores have been made utilizing an X-ray Computerized Tomography (CT) scanner. Saturation images were reconstructed in 3-D to observe better matrix-fracture interactions. Differences in fluid saturations and relative permeabilities caused by changes in fracture width have also been analyzed. The fracture system without a spacer showed a more stable front and faster breakthrough than the other. However, the final water saturation was higher in the wide fracture system, thus showing that capillary pressure in the narrow fracture has more effect on recovery. Simulations of the experiments were made using a commercial reservoir simulator (Eclipse). Fracture relative permeability and capillary pressure curves were obtained by history matching the experiments. Sensitivity analysis of parameters such as fracture relative permeability, capillary pressure in the fracture, and fracture width were also conducted. The results showed that the assumption of fracture relative permeability equal to phase saturation is incorrect. Moreover, larger flow resistance in the fractures was observed by comparing the experiments with numerical simulation work . We found that the processes are both capillary and viscous dominated.

INTRODUCTION

Fractured porous media are usually comprised of two systems: a matrix system that contains most of the fluid storage, and a fracture system where fluids can flow more easily. Under this assumption, flow equations are written assuming that reservoir behavior is dominated by the transfer of fluid from the matrix to the high conductivity fractures, which are also often entirely responsible for flow between blocks and flow to wells.

Any representation of the material balance equation that describes the flow through fractured porous media will assume the knowledge of both rock and fluids properties, capillary pressure and relative permeabilities. Any of these parameters can be obtained for the matrix by laboratory work, but not for the properties for the fractures. To obtain more data on parameters such as fracture capillary pressure, fracture relative permeabilities and/or saturation distributions, further experimental work is necessary.

Therefore, the purpose of this study is to investigate this problem both experimentally and by numerical simulation.

Previous experiments can be grouped into several broad categories: 1) imbibition dominated experiments, 2) gravity dominated experiments, and 3) flow in a single fracture experiments, which are mostly studied in geothermal and hazardous waste disposal problems, where the main topic is the understanding of flow with no or little matrix interaction in an attempt to obtain better fracture relative permeabilitiy data in more realistic fractures (Hughes, 1995).

In general, several authors (Kazemi and Merrill (1979), Beckner (1990), Gilman et al. (1994)) have assumed that fracture capillary pressures are negligible. Others have shown experimentally that capillary continuity becomes important when gravity provides a driving force (Horie et al. (1988), Firoozabadi and Hauge (1990), Labastie (1990), Firoozabadi and Markeset (1992). Kazemi (1990) states his belief that capillary continuity is prevalent in the vertical direction and has suggested that, to reduce the number of equations to solve, fractured reservoir simulations should use the dual permeability formulation for the z direction and the dual porosity formulation for the x and y directions.

For this work, detailed measurements of pressure, rate, and saturation distribution were performed, and attempts to measure phase distribution inside the fracture were also made using a (CT) scanner. This research resulted in a much better understanding of the physical processes that occur when two or three phases flow in a fractured system, compared to previous reported studies (Guzman and Aziz (1993), Hughes (1995)). Our first step was constructing an experimental apparatus capable of reproducing the results obtained by that by Hughes(1995). Thus, we conducted similar experiments using two of the core holders developed by him in order to verify that this new experiment gives consistant results. Once the apparatus was tested, we conducted water-air flow experiments using an 8% NaBr brine solution as the wetting phase. Differences in fluid saturations and relative permeabilities caused by changes in fracture width were also analyzed.

Simulations of the experiments using a commercial reservoir simulator were performed. Fracture relative permeability and capillary pressure curves were obtained by history matching the experiments qualitatively. A sensitivity analysis of parameters such as fracture relative permeability, capillary pressure in the fracture, and fracture width was also made.

EXPERIMENTAL DESIGN AND PROCEDURE

Two Boise sandstone cores that are rectangular in shape were used. Due to the rectangular shape and the desire to measure in-situ saturations through the use of the CT scanner, conventional core holders could not be used. A core holder similar to the one designed by Guzman and Aziz (1993) later developed by Hughes (1995) was used. It consists of an epoxy resin surrounding the core as well as plexiglas end plates and a piece

of 3/8 inch Viton acting as a gasket between the core and the plexiglas end plates as shown in Figure 1.

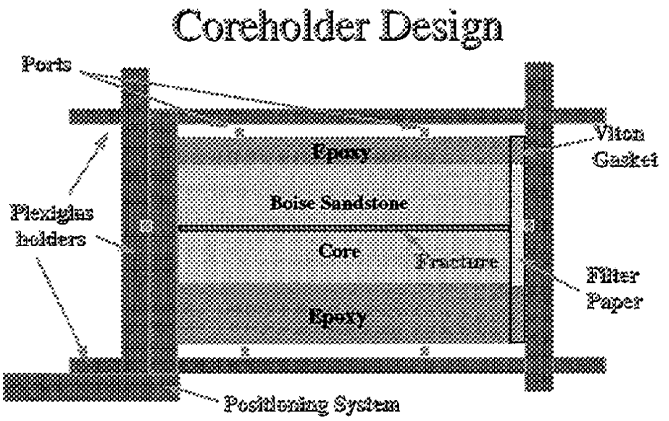

Figure 1. The Core Holder.

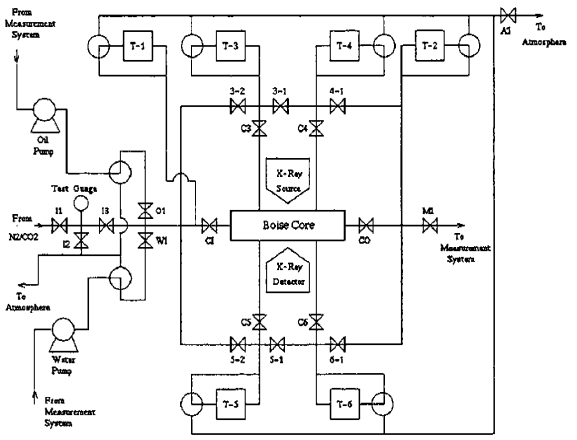

Figure 2. Flow System (After Hughes, 1995.)

The flow system shown in Figure 2 allows fluids to be directed to any port or combination of ports in the experiment such that 1)It can be directed to calibrate the pressure transducers, 2)It can be used to inject from one end and to produce from the opposite end, 3) It can be used to inject into one or more of the ports on the top and bottom of the core holder, or 4) To bypass the core holder completely. It also consists of two pumps that inject 0.01 to 9.99 cm^3/min in 0.01 increments. Plumbing downstream of the pumps allows mixing of the fluids being discharged by each pump. This setup allows injection pressure to be monitored with a test gauge and recirculation to measure pump output rates. An 8% NaBr doped water was used as the water phase, since adding salts to water increases water density and allows higher resolution images from the CT Scanner.

The first core used had a fracture with no spacer in between the blocks. The total travel distance of the positioning system (accuracy ± 0.01 mm) was then 25.5 cm,

resulting in 13 slices including those two located at the pressure ports (fourth and eleventh, for the first experiment; and fourth and tenth, for the second one.) The second experiment was done using a coreholder that contained a similar system with two Boise sandstone blocks with a 1 mm thick fracture in between. Figure 3 shows the CT scan locations.

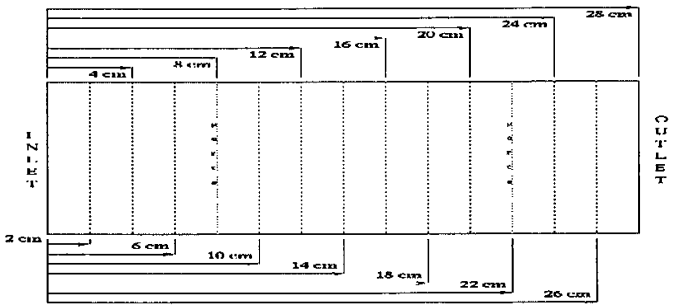

Figure 3. CT Scan Locations.

The first step of all experiments was to scan the dry core for reference dry images that are used to calculate the porosity and saturation distribution along the cores. The second step was to evaluate how water imbibed into an unsaturated core. Starting with a flow rate of 2 cm^3/min, CT images of the core were taken every 5 minutes until the first 20 minutes of water injection (0.15 PV). After this, images were taken at regular intervals. Following that the top and bottom ports were opened to allow the core to the maximum water saturation. Common to all time steps, we tried to take images up to one location ahead of the water front. After 5 hours (2.25 PV) of water injection, the flow rate was dropped to 0.5 cm^3/min and we injected water for 14 more hours to reach steady state. After 8.55 PV of water injected, reference 100% water saturated images were taken at the same locations. Two sets of CT slices were taken to find a possible change in CT numbers. Negligible changes in CT numbers were observed. Table 1 summarizes the flow rates used. The same experimental procedure was followed.

Table 1. Rates and Timing for the Core with Thin Fracture.

Fluid Injected	Time [hr.]	Flow Rate [cm^3/min]	Ports
Water	0.0 - 4.0	2.0	Top and bottom closed, lateral open.
Water	4.0 - 5.0	2.0	Top and bottom open, lateral closed.
Water	5.0 - 19.8	0.5	Top and bottom open, lateral closed.
Water	19.8 - 23.0	2.0	Top and bottom closed, lateral open..

DATA ANALYSIS

Using the CT numbers obtained from the experiments, porosity and saturation distribution along the core were determined. The most common way to calculate porosity

from CT Scanner images is by using the following expression (Withjack, 1988):

$$\phi = \frac{CT_{cw} - CT_{cd}}{CT_w - CT_a} \tag{1}$$

where CT_{cw} is the CT number for a 100% water saturated core at a matrix location, CT_{cd} is the CT number for a dry core at a matrix location, CT_w is the CT number for water, and CT_a is the CT number for air. The CT number for water (8%NaBr solution) is around 360, while the CT number for air is -1000. The water saturations were also calculated from the CT images. The following equation shows the way to evaluate water saturation for the water displacing air case.

$$Sw = \frac{CT_{aw} - CT_{cd}}{CT_{cw} - CT_{cd}} \tag{2}$$

RESULTS

First, we computed the values of porosity using Equation 1 at each location indicated in Figure 3. The porosity images for both systems are shown in Figure 4, where the values below each square correspond to the mean and the standard deviation, respectively, of the porosity values obtained from CT numbers. This step was essential for both experiments because from these images and their corresponding values we differentiated the regions with higher or lower porosity. The range of values are shown in the color bar in the right hand side in Figure 4. There, we can also see that the system with the thin fracture has a little higher porosity than the system with the wide fracture, especially in the top block, where values up to 0.13 were observed. We found that the average value for porosity calculated from the scans was 14.5% for the wide fracture system, which matches with the average value 14.35% reported by Hughes (1995).

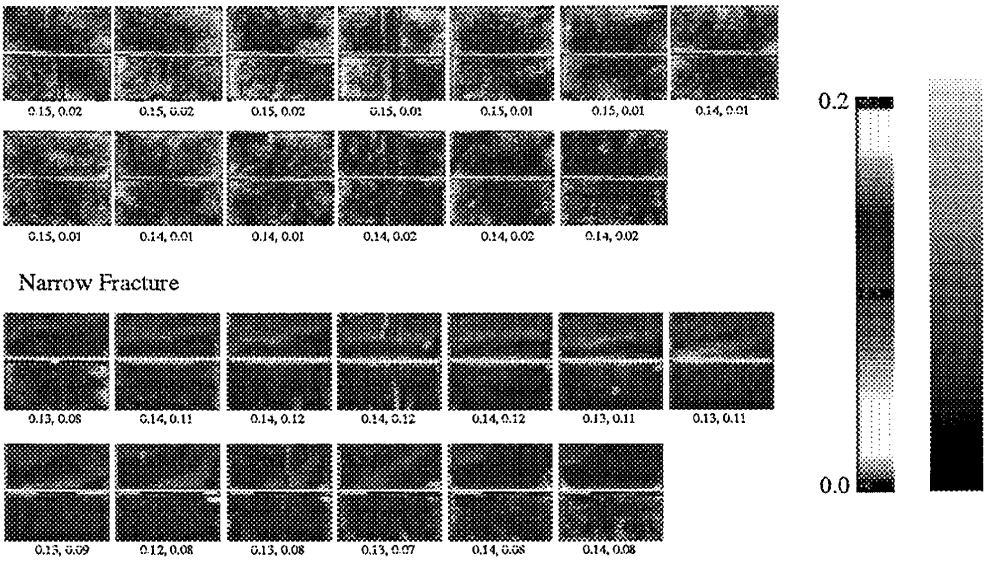

Figure 4. Porosity Distribution for the experimental system.

Following the aforementioned procedure, and the flow rates, times and injection/production conditions shown in Table 1, several sets of images like the one shown in Figure 5 corresponding to 1.5 hours of water injection (0.67 PV) were obtained. Similar to the porosity images, each square corresponds to water saturation values obtained at one location. The pair of values presented below each square corresponds to the mean and standard deviation of the top, bottom, and both blocks, respectively. The color bar on the right hand side shows the range of water saturation values. Different profiles, corresponding to different pore volumes of water injected were plotted. The profiles are more or less stable and they appear to be quasi one dimensional.

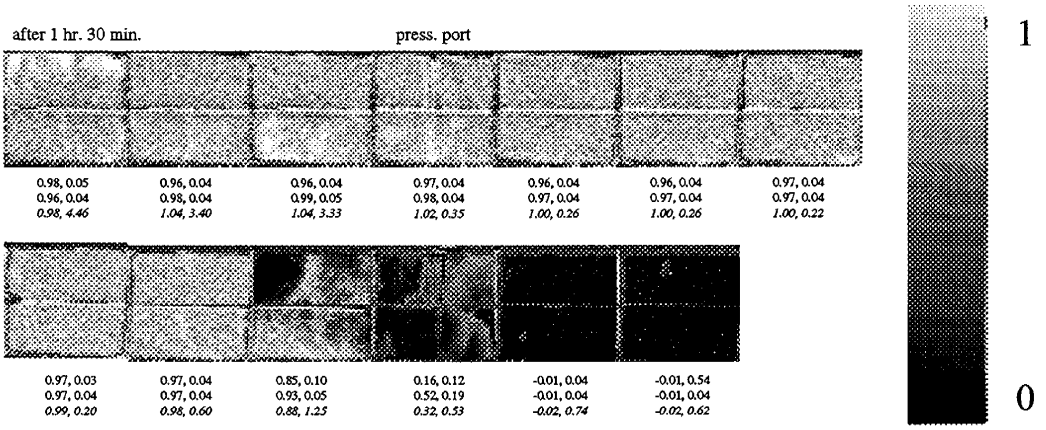

Figure 5. CT Saturation images for the Thin Fracture System after 1hr 30 min of Water injection.

The same procedure was followed for the wide fracture system and CT saturations were obtained. Figure 6 gives water saturation distribution at 0.67 PV of water injected. Different profiles, corresponding to different pore volumes of water injected were also plotted. The profiles are less stable than those for the thin fracture system as observed from the 8th through 12th slices. We observed similar profiles for all times (i.e., piston-like movement in thin fracture system, and unstable front in wide fracture system.)

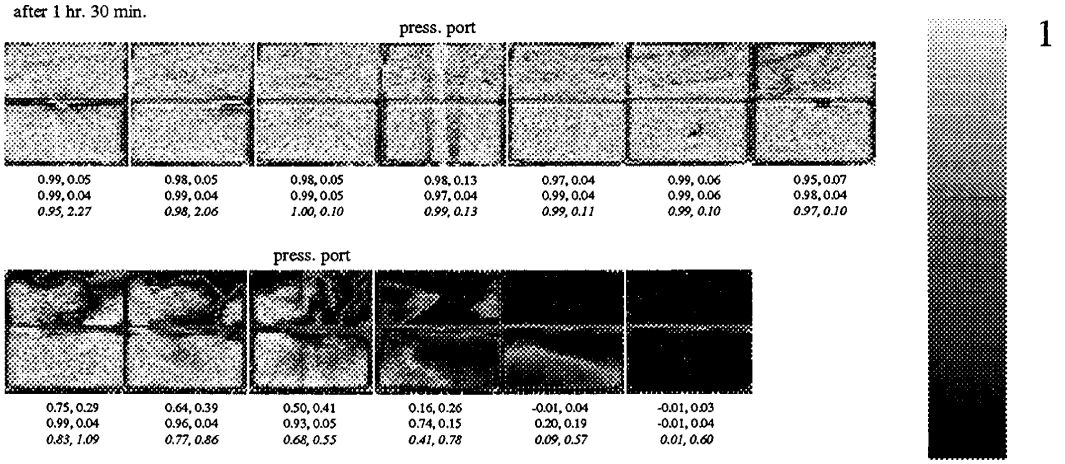

Figure 6. CT Saturation images for the Fracture System after 1hr 30 min of Water injection.

In order to have a better understanding of the processes and the differences between the flow patterns for different fracture widths, three dimensional (3-D) reconstruction of several sets of images were computed. These 3-D images show more clearly how the fluids actually flow through fractured porous media as shown in Figure 7. These reconstructions show water saturations greater than 50%. There, we can see how the water front for the wider fracture system goes almost at the same speed as the water front for the thinner fracture system does for the same time. For instance, one can see that after 1.5 hours of water injection, the water front in the thin fracture system seems to be ahead of the front for the wide fracture system; however, after two hours of water injection water has filled up both systems.

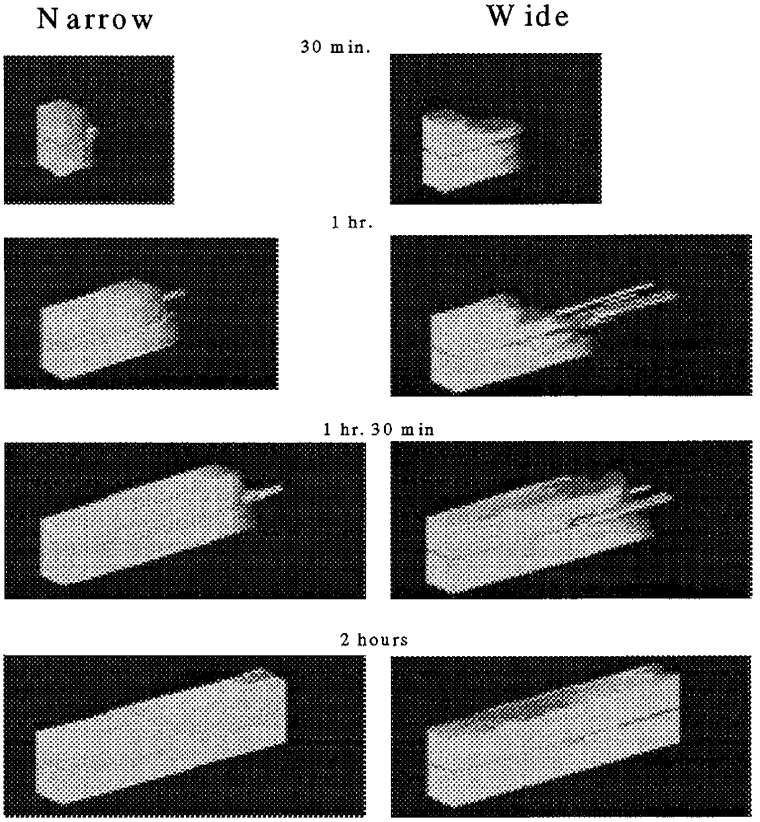

Figure 7. 3-D Reconstruction for both systems for $S_w \geq 0.5$.

It can be observed that for the thin fracture system the front is stable. The flow from the fracture to the matrix is clearly visible. That is to say, capillary continuity is maintained between the fracture and the matrix. However, for the wide fracture system the imbibition forces are not that strong and the front is not piston like. We also observed faster breakthrough times for the wide fracture.

NUMERICAL SIMULATION WORK

Simulations of the experiments using a commercial reservoir simulator have been completed. A cubic cartesian gridding proportional to the cores was designed in such a way that we had three different "boxes". Two of them simulate the top and bottom blocks with matrix rock properties; i.e., matrix capillary pressure curves, matrix relative permeability curves, matrix absolute permeability, porosity, and the other set of blocks simulate the horizontal fracture with fracture properties; i.e., large absolute permeability, fracture capillary pressure curves, and fracture relative permeability curves. It was assumed that relative permeability and capillary pressure in the matrix are constant. We used the curves presented by Persoff et. al. (1991). Fracture relative permeability and capillary pressure curves were obtained by history matching the experiments. Sensitivity analysis of parameters such as fracture relative permeability, capillary pressure in the fracture, and fracture width have been done. We considered each parameter independently.

First, we studied capillary pressure in the fracture under the assumption that it is a linear function of water saturation. Different cases for capillary pressure curves and relative permeability curves for the fracture are shown in Figure 8. It is important to note that for fracture relative permeability curves, the lower the slope of the straight line, the higher the resistance to flow through the fracture. Starting with a high capillary pressure in the fracture, we observed that the matrix front matched well, but the breakthrough time was faster compared to our experimental results. We decreased the slope of the straight line capillary pressure in the fracture up to a point in which the breakthrough time as well as the matrix front matched the experiments. For the sake of completeness, we also studied extreme cases that are often used in real practice such as very low and no capillary pressure in the fracture, although neither one resembled experimental data. The no capillary pressure case showed us that the blocks worked independently, so the capillary continuity that we had seen in the experiments did not occur in the numerical studies.

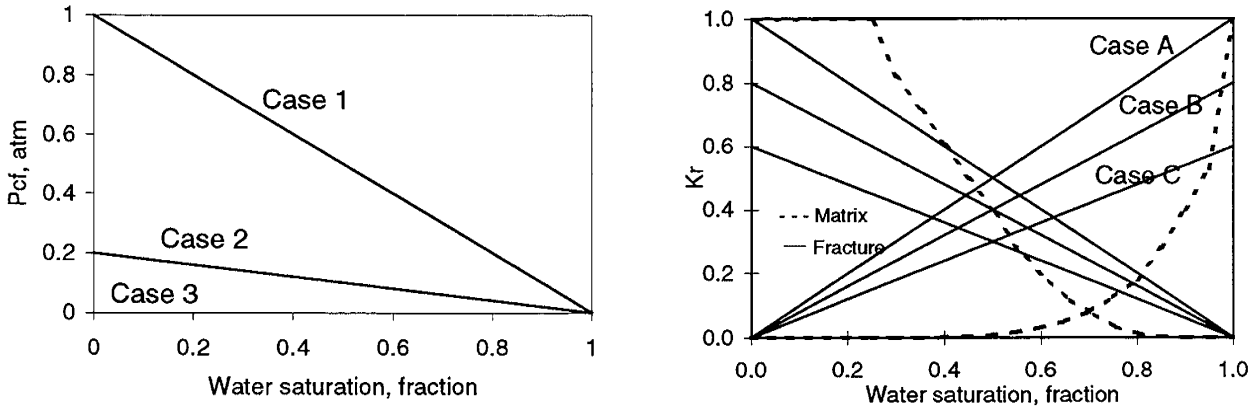

Figure 8. Different cases for capillary pressure curves and relative permeability curves for the fracture.

After obtaining the proper description of capillary pressure in the fracture, we continued by studying the effect of fracture relative permeability curves. The assumption of fracture relative permeability equal to phase saturation is often used in numerical simulation. This assumption suggests, no resistance, ideal flow of fluids in the fractures, such that inside the fracture the phases can move past each other without hindrance. However, if relative permeabilities with a slope less than 1.0 is used, the effective total mobility is reduced. Pan et. al. (1996) discussed that higher resistance in the fractures must be used, such as 0.8 and 0.6 slope straight lines instead. Our results show that the best matches are achieved when an 0.6 slope is used. This indicates that the presence of a small amount of one phase interferes significantly with the flow of the other phase.

In order to obtain the best match, we also examined the heterogeneities present in the systems, especially in the wide fracture system. So we ran different heterogeneous cases until we obtained better matches. We achieved this goal by assigning higher porosity (14%) to the bottom block and lower porosity (13%) to the top block. The results for this case are shown in Figure 9 which proves that, capillary pressure in the fracture can not be neglected and the heterogeneity must also be considered.

Similarly, we followed the same analysis for the system with no spacer in between the blocks. An interesting observation was that neither the capillary pressure in the fracture nor the relative permeability curves affected the results. That lead us to the conclusion that the fracture is so thin that there is almost perfect continuity, and it acts like a solid block. Figure 9 also shows the comparison of the experimental results with the numerical simulation results for the system with no spacer. The fracture system without a spacer showed a more stable front and faster breakthrough than the other, as we had seen in the experimental results.

CONCLUSIONS

The results of the combined experimental and the simulation study show:

1. Areas with lower permeability and porosity were identified and used in numerical simulations.
2. Thin fracture system showed more stable fronts and slower breakthrough compared to wide fracture systems.
3. Capillary pressure has more effect when the fractures are narrow.
4. Larger recoveries can be obtained when the fractures are wider.
5. Assuming zero capillary pressure in the fracture is incorrect.
6. X-type relative permeability curves can be used for fractured systems using high resistance through fractures.

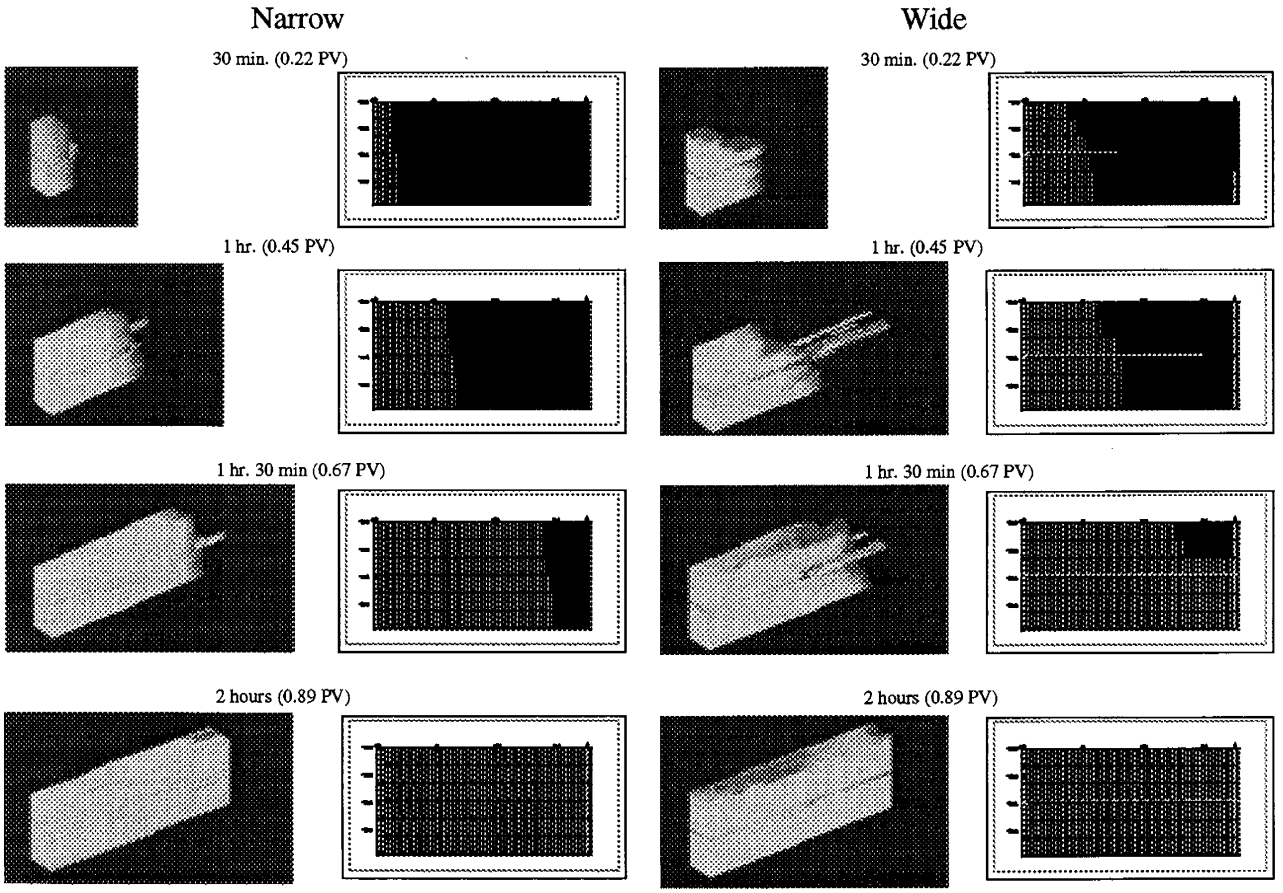

Figure 9. Comparison between experiments and simulations for narrow and wide fracture systems.

AKNOWLEDGEMENTS

This work is supported by U.S. Department of Energy under contract No. DE-FG22-96BC14994, SUPRI-A Industrial Affiliates and Consejo Nacional de Ciencia y Tecnología (CONCACyT), México.

REFERENCES

Beckner, B.L.: *Improved Modeling of Imbibition Matrix/Fracture Fluid Transfer in Double Porosity Simulators*, PhD dissertation, Stanford University (July 1990)

Buckley, S.E. and Leverett, M.C.: "Mechanisms of Fluid Displacement in Sands," Transactions American Institute of Mining and Metallurgical Engineers, 146 (1942), 107-116.

Eclipse 100 User's Manual, Intera Information Technology Limited, Oxfordshire, England, 1994.

Firoozabadi, A. and Hauge, J.: "Capillary Pressure in Fractured Porous Media," JPT (June 1990) 784-791.

Firoozabadi, A. and Markeset, T.: "An Expe
Crossflow in Fractured Porous Media," SPE 2
Technical Conference and Exhibition, Washingt

Gilman, J.R., Bowzer, J.L. and Rothkopf, B.W.
Boreholes in the Naturally Fractured Yates Fiel
Annual Technical Conference and Exhibition, Ne

Guzman, R.E. and Aziz, K.: *Design and Const*
Flow in Fracuted Porous Media, SUPRI TR-9
Stanford, CA, (June 1993).

Horie, T., Firoozabadi, A. and Ishimoto,
Reservoirs," SPE 18282, presented at the 63r
Exhibition, Houston, TX, October 2-5, 1988.

Hughes, R.G.: *CT Measurements of Two-Ph*
Masters Report, Stanford University (December

Kazemi, H. and Merrill, L.S.: "Numerical Sin
Cores," SPEJ (June 1979) 175-182.

Kazemi, H.: *Naturally Fractured Reservoirs,*
Simulation, Baden, Austria (1990).

Labastie, A.: "Capillary Continuity Between Blo
presented at the 65th SPE Annual Technical C
LA, September 23-26, 1990.

Pan, X. and Wong, R.C.: "Steady State Tw
presented at the 47th Annual Technical Meetin
Alberta, Canada, June 10-12, 1996.

Persoff, P., Pruess, K., and Myer, L.: "Two-Pha
Permeability Measurement in Transparent Replic
Sixteenth Workshop on Geothermal Reservoir,

Withjack, E.M.:"Computed Tomography for
Flow Visualization", SPEFE (December, 1988)

1.2.2 SPE 54591: MULTIPHASE-FLOW PROPERTIES OF FRACTURED POROUS MEDIA

(Edgar Rangel-German, Serhat Akin and Louis M. Castanier)

This paper was prepared for presentation at the 1999 SPE Western Regional Meetingh to be held in Anchorage, Alaska, May 256-28, 1999).

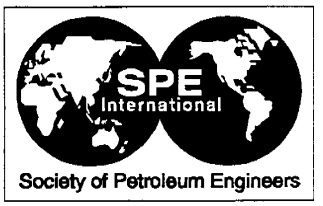

SPE 54591

Multiphase-Flow Properties of Fractured Porous Media

E. Rangel-German, S. Akin, and L. Castanier, Stanford University

Copyright 1999, Society of Petroleum Engineers Inc.

This paper was prepared for presentation at the 1999 SPE Western Regional Meeting held in Anchorage, Alaska, 26–28 May 1999.

This paper was selected for presentation by an SPE Program Committee following review of information contained in an abstract submitted by the author(s). Contents of the paper, as presented, have not been reviewed by the Society of Petroleum Engineers and are subject to correction by the author(s). The material, as presented, does not necessarily reflect any position of the Society of Petroleum Engineers, its officers, or members. Papers presented at SPE meetings are subject to publication review by Editorial Committees of the Society of Petroleum Engineers. Electronic reproduction, distribution, or storage of any part of this paper for commercial purposes without the written consent of the Society of Petroleum Engineers is prohibited. Permission to reproduce in print is restricted to an abstract of not more than 300 words; illustrations may not be copied. The abstract must contain conspicuous acknowledgment of where and by whom the paper was presented. Write Librarian, SPE, P.O. Box 833836, Richardson, TX 75083-3836, U.S.A., fax 01-972-952-9435.

Abstract

The fluid transfer parameters between matrix and fracture are not well known. Consequently, simulation of fractured reservoirs uses, in general, very crude and unproved hypothesis such as zero capillary pressure in the fracture and/or relative permeability functions that are linear with saturation. In order to improve the understanding of flow in fractured media, an experimental study was conducted and numerical simulation used to interpret experimental results.

A laboratory flow apparatus was built to obtain data on water-air imbibition and oil-water drainage displacements in fractured sandstone systems. During the experiments, porosity and saturation were measured along the core utilizing a Computerized Tomography (CT) scanner. Saturation images were reconstructed in 3-D to observe how matrix-fracture interaction occurred. Differences in fluid saturations and relative permeabilities caused by changes of fracture width have also been analyzed.

In the case of water-air imbibition, fracture systems with narrower fracture apertures showed more stable fronts and slower water breakthrough than the wide fracture systems. However, the final water saturation was higher in wide fracture systems, thus showing that capillary pressure in the narrow fracture has more effect on fluid distribution in the matrix. During oil-water drainage, oil saturations were higher in the blocks near the thin fracture, again showing the effect of fracture capillary pressure. Oil fingering was observed in the wide fracture.

Fine-grid simulations of the experiments using a commercial reservoir simulator were performed. Relative permeability and capillary pressure curves were obtained by history matching the experiments. The results showed that the assumption of fracture relative permeability equal to phase saturation is incorrect. We found that both capillary and viscous forces affect the process. The matrix capillary pressure obtained by matching an experiment showed lower values than reported in the literature.

Introduction

Flow equations describing fractured porous media are usually written assuming that reservoir behavior is dominated by the transfer of fluid from the matrix to high conductivity fractures, that are often entirely responsible for flow between blocks and flow to wells.

Conventional representation of these equations assumes the knowledge of both rock and fluid properties, capillary pressure, and relative permeabilities. Any of these parameters can be obtained for the matrix by laboratory work, but not for the fractures. To obtain more data on properties such as fracture capillary pressure, fracture relative permeabilities and/or saturation distributions, an experimental and numerical study was conducted

In general, several authors (Kazemi and Merrill (1979), Beckner (1990), Gilman et al. (1994)) have assumed that fracture capillary pressure is negligible. Others have shown experimentally that capillary continuity becomes important when gravity provides a driving force (Horie et al. (1988), Firoozabadi and Hauge (1990), Labastie (1990), Firoozabadi and Markeset (1992). Kazemi (1990) states his belief that capillary continuity is prevalent in the vertical direction and has suggested that, to reduce the number of equations to solve, fractured reservoir simulators should use the dual-permeability formulation for the z direction and the dual-porosity formulation for the x and y directions.

For this work, detailed measurements of pressure, rate, and saturation distribution were performed, and attempts to measure phase distribution inside the fracture were also made using a (CT) scanner. This research resulted in a much better understanding of the physical processes that occur when two or three phases flow in a fractured system, compared to previous reported studies (Guzman and Aziz (1993), Hughes (1995)). Our first step was constructing an experimental apparatus capable of reproducing the results obtained by that by Hughes(1995). Thus, we conducted similar experiments using two of the core holders developed by him in order to verify that this new experiment gives consistent results. Once the apparatus was tested, we conducted multiphase flow

experiments using an 8% NaBr brine solution as the wetting phase, and decane as the nonwetting phase. Three stages in each experiment were completed: study of water imbibing into a dry core, decane displacing water in a water-saturated core, and water displacing oil. Differences in fluid saturations and relative permeabilities caused by changes in fracture width were also analyzed.

Simulations of the experiments using a commercial reservoir simulator were performed. Fracture relative permeability and capillary pressure curves were obtained by history matching the experiments. A sensitivity analysis of parameters such as fracture relative permeability, capillary pressure in the fracture, and fracture width was also completed.

Experiment Design

The experiments presented in this work were made using an apparatus similar to the one designed, constructed and used by Hughes (1995). The following subsections give a description of the material and methods used to build the experimental set-up.

Cores. For this work, we used two of the three rectangular blocks of Boise sandstone cores constructed and used by Hughes(1995). Both core holders consist of two 2 15/16 x 1 1/2 x 11 inch blocks. The first core holder is system of the two blocks together, i.e. with no spacer in between the blocks. The second one is a similar configuration, but has a 1-mm thick spacer fastened in place with Epoxy 907 to provide separation between the blocks to simulate a fracture.

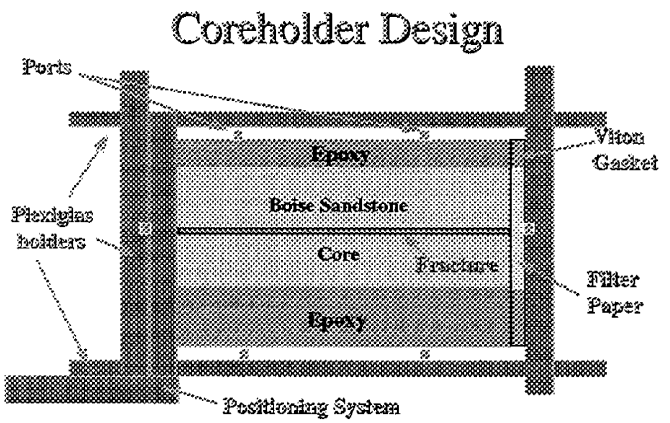

Fig. 1- The Core Holder.

Core holders. Due to the rectangular shape and the desire to measure in-situ saturations through the use of the CT scanner, conventional core holders could not be used. A core holder similar to the one designed by Guzman and Aziz (1993), and later developed by Hughes (1995) was used. An epoxy resin surrounds the core, as well as plexiglas end plates and a piece of 3/8 inch Viton that acts as a gasket between the core and the plexiglas end plates as shown in **Fig. 1**.

Positioning System. The positioning system consists of a moving table with 0.01 mm accuracy that is positioned electronically by means of a control panel. Basically, any flat surface can be attached to this table using screws. This system was one of the major improvements to previous designs (Guzman, 1993; Hughes, 1995). In this way, we can obtain cross-sectional images of the core at the same location at any desired time of the experiment. This could not be performed in other studies because the standard patient table of a CT Scanner of this type lacks comparable accuracy.

Flow System. The flow system **(Fig. 2)** allows fluids to be directed to any port or combination of ports in the experiment such that: 1)It can be directed to calibrate the pressure transducers, 2)It can be used to inject from one end and to produce from the opposite end, 3) It can be used to inject into one or more of the ports on the top and bottom of the core holder, or 4) To bypass the core holder completely. It also consists of two pumps that inject 0.01 to 9.99 cm^3/min in 0.01 increments. Plumbing downstream of the pumps allows mixing of the fluids being discharged by each pump. This setup allows injection pressure to be monitored with a test gauge and recirculation to measure pump output rates.

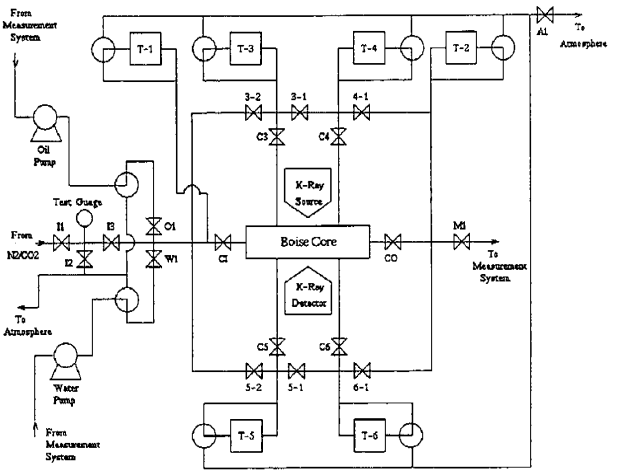

Fig. 2- Flow System (After Hughes, 1995.)

Production Measurement System. The production measurement system is an adaptation of a design given by Ameri and Wong (1985). **Fig. 3** shows this system. The electronic balances are connected to the serial communication ports of a personal computer (PC).

Pressure Measurement System. Pressure drop along the core can be measured between any of the six different positions on the core labeled as T-x. In **Fig. 2,** one can see that two of the transducers are connected to the inlet and outlet of the core holder. Each transducer is connected to a carrier demodulator which produces a DC signal in the range from -10 to +10 V that is proportional to the pressure drop.

The output signals were recorded on a chart recorder and also captured in digital form.

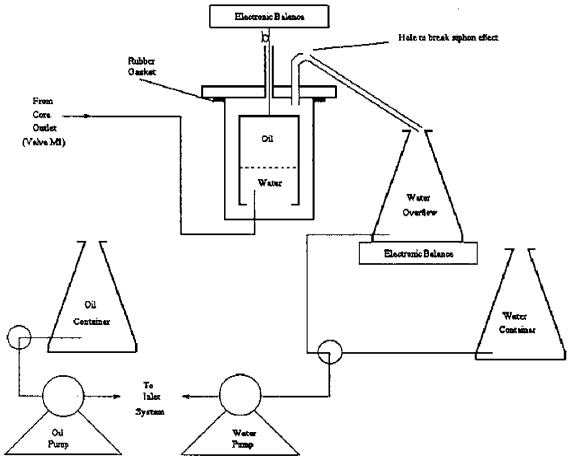

Fig. 3- Production system (after Hughes, 1995.)

CT Scanner. A CT Scanner can be used to calculate porosity, saturation and in some cases, concentration distribution and to track advancing fronts. It can also be used to measure fracture aperture. We use a Picker 1200SX Dual Energy CT scanner.

Fluids. CT numbers are proportional to their densities. A selection of fluids and dopants were employed in order to obtain the best contrast in CT numbers and, hence, most accurate in terms of phase saturation. Decane was used to represent the oil phase, and 8% NaBr, by weight, water solution was used as the water phase.

Experimental Procedure

The first core used had a fracture with no spacer in between the blocks. The total travel distance of the positioning system (accuracy ± 0.01 mm) was then 25.5 cm, resulting in 13 slices including two located at the pressure ports (fourth and eleventh, for the first experiment; and fourth and tenth, for the second experiment.) The second experiment was conducted using a core holder that contained a similar system with two Boise sandstone blocks with a 1 mm thick fracture in between. **Fig. 4** shows the CT scan locations.

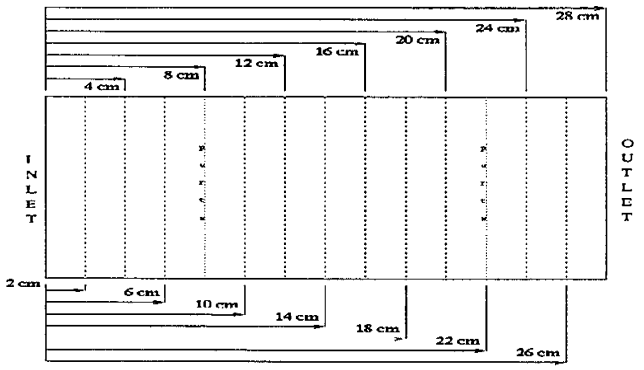

Fig. 4- CT Scan locations.

The first step in the experimental procedure was to scan the dry core. This step was very important to verify that the apparatus and the set-up were working properly. For instance, there were some problems with the core holder in a first trial for the dry scan. We could not keep its position horizontal, because it was quite heavy and held only by one of the sides. Two C clamps were used to strengthen the attachment to the positioning system and, thus, to keep the core holder in the same horizontal position during the experiment. After these improvements, the dry scans were conducted successfully.

The second step was to evaluate how water imbibed into an unsaturated core. This part of the experiment gave us results that can be compared with those obtained by Hughes (1995), and eventually used to evaluate how well the new experiment worked. Starting with a flow rate of 2 cm^3/min, CT images of the core were taken every 5 minutes for the first 20 minutes of water injection (0.15 PV); after this, images were taken at 30 min (0.22 PV), 45 min (0.33 PV), 1 hr. (0.45 PV), 1hr 30 min (0.67 PV), 2 hr (0.89 PV), 3 hr (1.34 PV), and 4 hours (1.78 PV) after water injection started. Next, the top and bottom ports were opened since we wanted to fill up the core to the maximum water saturation (S_w=1.) Common to all time steps, we tried to take images up to one location ahead of the position of the water front.

After 5 hours of water injection (2.25 PV), the flow rate was changed to 0.5 cm^3/min in order to inject water for 14 more hours to reach steady state. After 19 hours (8.55 PV), reference 100% water saturated images were taken. Then, at 19 hours and 45 min (8.9 PV) the water rate was changed back to 2 cm^3/min, and the top and bottom ports were closed. At 21 hours (9.45 PV) a final set of slices was taken to find any possible change in CT numbers. Negligible changes in CT numbers were observed. At 23 hours of water injection, the third step of the experiment started. Table 1 summarizes the flow rates used.

The third step of the experiment involved injecting decane at 2 cm^3/min. The scanning frequency was intended to be the same as the water injection process. Thus, images of the core were taken every five minutes until the first 20 minutes of oil injection (0.15 PV). After that, more images were taken at 30 min (0.22 PV), 45 min (0.33 PV), 1 hr. (0.45 PV), 1hr 30 min (0.67 PV), 2 hr 30 min (1.13 PV), and 3 hr 45 min. (1.69 PV) after oil injection started. Then, the top and bottom ports were opened at 4 hours (1.79 PV) since we wanted to fill the core up to the maximum possible point. At 4 hr 30 min of oil injection, one more set of images was taken. After 5 hours (2.25 PV) of oil injection, the flow rate was changed to 1 cm^3/min for 16 hours (7.2 PV) to reach higher possible oil saturations (1-S_{wc}). After 21 hours of oil injection (9.45 PV), a new set of slices was taken, and the ports were closed. Then, at 21 hours and 39 min the oil injection was stopped, and water injection at the maximum pump rate (9.99 cm^3/min) was started.

The fourth step of the experiment was the water displacing oil stage. Injecting 9.99 cm^3/min of water, images were taken at 5 min (0.04 PV), 15 min (0.13 PV), and 30 min (0.23 PV). At 1hr 10 min (0.53 PV), water injection was stopped, the inlet and outlet lateral ports were also closed, leaving all of the core holder's ports closed. One more set of images was taken after two days of closing the core holder to observe if capillary equilibrium had been reached. Table 1 summarizes the flow rates used and the timing of each.

The second experiment was performed using the core holder that contained a system with two Boise sandstone blocks with a 1 mm thick fracture in between. The same experimental procedure was followed. Essentially, we wanted to obtain CT images, and then saturation values for equivalent times, so we could compare the differences between the two systems. The rates and timing for the case of two blocks with a wider fracture are shown in Table 2.

Data Analysis

Using the CT numbers obtained from the experiments, porosity and saturation distributions along the core were determined. The most common way to calculate porosity from CT Scanner images is by using the following expression (Withjack, 1988):

$$\phi = \frac{CT_{cw} - CT_{cd}}{CT_w - CT_a} \quad \text{.....(1)}$$

where CT_{cw} is the CT number for a 100% water saturated core at a matrix location, CT_{cd} is the CT number for a dry core at a matrix location, CT_w is the CT number for water, and CT_a is the CT number for air. The CT number for water (8%NaBr solution, for this work) is around 360, while the CT number for air is -1000.

The water and oil saturations were also calculated from the CT images. The following equations show how to evaluate water saturation for the water displacing air case, and for the oil displacing water or water displacing oil case.

$$S_w = \frac{CT_{aw} - CT_{cd}}{CT_{cw} - CT_{cd}}. \quad \text{.....(2)}$$

where CT_{aw} is the CT number for water and air saturated core at a matrix location. Similarly, for the case of oil-water systems:

$$S_w = \frac{CT_{ow} - CT_{cw}}{\phi(CT_o - CT_w)}. \quad \text{.....(3)}$$

where CT_{ow} is the CT number for a water and oil saturated core at a matrix location, and CT_o is the CT number for oil. The CT number for oil (decane, for this work) is around -272.

Experimental Results

First, we computed the values of porosity using Eq. 1 at each location indicated in **Fig. 4**. The porosity images for both systems are shown in **Fig. 5**, where the values below each square correspond to the mean and the standard deviation, respectively, of the porosity values obtained from CT numbers. This step was essential for both experiments because from these images and their corresponding values we differentiated the regions with higher or lower porosity. The range of values is shown in the color bar in the right hand side in **Fig. 4**. There, we can also see that the system with the thin fracture has a little higher porosity than the system with the wide fracture, especially in the top block, where values up to 0.13 were observed. We found that the average value for porosity calculated from the scans was 14.5% which matches with the average value 14.35% reported by Hughes (1995); however, this value differs from the average porosity measurements of 25.4% obtained by Guzman and Aziz (1993) and 29.3% obtained by Sumnu (1995). All of these previous studies have also shown areas in the rocks, which have lower permeability.

Water-Air Imbibition. Following the aforementioned procedure, and the flow rates, times and water injection conditions listed in Table 1, several sets of images like those shown in **Fig. 6** corresponding to 1.5 hours of water injection (0.67 PV) were obtained. Similar to the porosity images, each square corresponds to water saturation values obtained at one location. The pair of values presented below each square corresponds to the mean and standard deviation of the top, bottom, and both blocks, respectively. The gray scale on the right hand side shows the range of water saturation values. Different profiles, corresponding to different pore volumes of water injected were plotted. The profiles are more or less stable and they appear to be quasi one dimensional. The same procedure was followed for the wide fracture system and CT saturations were obtained. **Fig. 7** gives water the saturation distribution at 0.67 PV of water injected. Different profiles, corresponding to different pore volumes of water injected were also plotted. The profiles are less stable than those for the thin fracture system as observed from the 8th through 12th slices. We observed similar profiles for all times.

Oil-Water Drainage. Similar images were obtained for the second stage of the experiments (oil injection). **Fig. 8** shows a set of images corresponding to 2.5 hours (1.13 PV) of oil injection. Here, the pairs of values below each square indicate the mean and the standard deviation of oil saturation, respectively. Shades were also assigned to the oil saturation values. Thus, the gray scale on the right hand side shows the

range of values and their corresponding lightness or darkness. In all the images shown in **Fig. 8** darker shades indicate lower oil saturation. For instance, black means zero oil saturation. This stage was finished after 4 hours of oil injection when we opened the lateral ports of the core holder to reach the maximum possible oil saturation. The corresponding images for the wide fracture system are shown in **Fig. 9**.

Water-Oil Displacement. Images for the third stage of the experiment (water displacing oil) were also obtained. Due to problems with one of the pumps, we could not analyze properly the rest of the data for the case of thin fracture system. Images for the third stage of the second experiment (water displacing oil in the wide fracture system) were also obtained. The most interesting sets are shown in **Fig. 10** and **Fig. 11** corresponding to 16 hours (7.2 PV) and 17 hours (7.7 PV) of water injection, respectively. One can see that the displacement of oil is completed almost perfectly.

Analysis of Experimental Results

Due to the fact that the experiments ended differently, we were able to compare the results up to the second stage of both experiments. This section shows the comparison graphically.

Three-dimensional (3-D) reconstructions of the sets of water saturation images were calculated. All these images were obtained using a color map for values above 50% of water or oil saturation, respectively. These 3-D images show more clearly how the fluids actually flow through the fractured porous media. This work was intended to show the differences between the flow patterns for different fracture thicknesses. The reconstructed images are shown in **Fig. 12.** Each image corresponds to a specific time. Thus, the first image on the left-hand side of Fig. 12 is compared to the first one of the right hand side of the same Fig. 12. The second image on the left hand side was computed for the same time as the second image on the right hand side, and so on. There, we can see that the water front for the wider fracture system moves at almost at the same speed as the water front for the narrow fracture system does. For instance, one can see that after 1.5 hours of water injection, the water front of the narrow fracture system seems to be ahead of the front for the wide fracture system; however, after two hours of water injection water has filled up both systems.

Similarly, the 3-D oil injection history was also reconstructed. Since the oil saturations were low for both cases, it is a bit harder to see the differences. It is possible to see that the thinner fracture system has higher oil saturation close to the fracture. This is shown in **Fig.13.** One can see that the narrow fracture system has lighter colors close to the injection surface. We can also see that for the case of the wide fracture system, the oil does not penetrate. Furthermore, oil flows almost completely through the fracture. This is shown in all the images on the right hand side of Fig. 13 by the almost white horizontal line that corresponds to the fracture. Remember that for the case of oil injection stages, darker means lower oil saturation.

Numerical Simulation Results

Numerical simulations of the experiments using a commercial reservoir simulator were conducted to study fracture relative permeability and matrix/fracture interaction, to match previous experimental results, and to provide experimental-numerical based suggestions how to simulate multiphase flow in fractured porous media.

A cubic Cartesian gridding proportional to the cores was designed in such a way that we had three different "boxes". Two of them simulate the top and bottom blocks with matrix rock properties; i.e., matrix capillary pressure curves, matrix relative permeability curves, matrix absolute permeability, porosity, and the other set of blocks simulate the horizontal fracture with fracture properties; i.e., large absolute permeability, fracture capillary pressure curves, and fracture relative permeability curves. It was assumed that relative permeability and capillary pressure in the matrix are constant.

For the water-air cases, we used the curves presented by Persoff et. al. (1991) for matrix relative permeability and the ones measured by Sanyal (1972) for matrix capillary pressure. For the oil-water cases, we used the matrix capillary pressure curves presented by Sanyal (1972). Unfortunately, no relative permeability curves for oil-water system in Boise sandstone have been reported, so we followed the procedure presented by Purcell(1949) to obtain the matrix relative permeability curves.

Fracture relative permeability and capillary pressure curves were obtained by history matching the experiments. Sensitivity analysis of parameters such as fracture relative permeability, capillary pressure in the fracture, and fracture width have been completed. We considered each parameter independently.

First, we studied capillary pressure in the fracture under the assumption that it is a linear function of water saturation. Different cases for capillary pressure curves and relative permeability curves for the fracture are shown in **Fig. 14.** It is important to note that for fracture relative permeability curves, the lower the slope of the straight line, the higher the resistance to flow through the fracture. Starting with a high capillary pressure in the fracture, we observed that the matrix front matched well, but the breakthrough time was faster compared to our experimental results. We decreased the slope of the straight line capillary pressure in the fracture up to a point in which the breakthrough time as well as the matrix front matched the experiments. For the sake of completeness, we also studied extreme cases that are often used in real practice such as very low and no capillary pressure in the fracture, although neither one resembled experimental data. The no capillary pressure case showed us that the blocks

worked independently, so the capillary continuity that we had seen in the experiments did not occur in the numerical studies.

After obtaining the proper description of capillary pressure in the fracture, we continued by studying the effect of fracture relative permeability curves. The assumption of fracture relative permeability equal to phase saturation is often used in numerical simulation. This assumption suggests, no resistance, ideal flow of fluids in the fractures, such that inside the fracture the phases can move past each other without hindrance. However, if relative permeabilities with a slope less than 1.0 are used, the effective total mobility is reduced. Pan and Wang (1996) discussed that higher resistance in the fractures must be used, such as 0.75 and 0.6 slope straight lines instead. Our results show that the best matches are achieved when an 0.6 slope is used. This indicates that the presence of a small amount of one phase interferes significantly with the flow of the other phase.

In order to obtain the best match, we also examined the heterogeneities present in the systems, especially in the wide fracture system. We ran different heterogeneous cases until we obtained better matches. We achieved this goal by assigning higher porosity (14%) to the bottom block and lower porosity (13%) to the top block. The results for this case are shown in **Fig. 15** which proves that, capillary pressure in the fracture can not be neglected and the heterogeneity must also be considered.

Similarly, we followed the same analysis for the system with no spacer in between the blocks. An interesting observation was that neither the capillary pressure in the fracture nor the relative permeability curves affected the results. That led us to the conclusion that the fracture is so thin that there is almost perfect continuity, and it acts like a solid block. **Fig. 15** also shows the comparison of the experimental results with the numerical simulation results for the system with no spacer. The fracture system without a spacer showed a more stable front and faster breakthrough than the other, as we had seen in the experimental results.

Similarly, we followed the same procedure for the oil injection stages. The matches for the thin fracture system were not very good, but the results for the wide fracture system, where we had seen in the experiments that most of the oil flowed though the fracture, are better. In this case, the assumption of zero capillary pressure in the fracture worked properly. These results are shown in **Fig. 16**.

Discussion and Recommendations

An apparatus that can be used to obtain detailed measurements of pressure, rate and saturation distribution was built and tested. It consists of a fractured core in an epoxy core holder, with six different locations for pressure measurements. Phase distribution in the matrix and inside the fracture were also determined by means of a (CT) scanner.

Multiphase flow runs were performed, and data were obtained. The experimental results were matched well by numerical simulation. Numerical simulations were also used to estimate the influence of variables such as fracture relative permeability, matrix/fracture capillary pressure, and fracture width. The results show that capillary pressure is a dominant parameter in this type of water displacement. Knowledge of the capillary pressure function is then critical.

The combined experimental and simulation study resulted in a much better understanding of the physical processes that occur when two or three phases flow in a fractured system, compared to previous reported studies (Guzman and Aziz (1993), Hughes (1995)).

This work allowed us to find areas with lower permeability and porosity, and then use them in the numerical simulations to obtain the best matches as shown in **Fig. 15**, for instance. All the CT images and the three-dimensional reconstructions obtained from them made the understanding of multiphase flow and the comparison with simulation results much easier, as shown in **Fig. 15** and **Fig. 16**.

Several authors (Kazemi and Merrill (1979), Beckner (1990), Gilman et al. (1994)) have assumed that fracture capillary pressures are negligible. Others have shown experimentally that capillary continuity becomes important when gravity provides a driving force (Horie et al. (1988), Firoozabadi and Hauge (1990), Labastie (1990), Firoozabadi and Markeset (1992). Kazemi (1990) stated that capillary continuity is prevalent in the vertical direction and has suggested that, to reduce the number of equations to solve, fractured reservoir simulations should use the dual permeability formulation for the z direction and the dual porosity formulation for the x and y directions.

This work showed that capillary continuity can occur in any direction, depending on the relative strengths of the capillary and Darcy terms in the flow equations; the thin fracture systems have a more stable front and slower breakthrough compared to wide fracture systems, and that capillary pressure has more effect when the fracture is narrow. We observed that neither the capillary pressure nor the relative permeability curves in the fracture affected the results for the narrow fracture system. That led us to the conclusion that the fracture is so thin and/or each half mated so well that there is almost perfect capillary continuity, and it acts very similar to a solid block.

With this work we were able to verify that larger recoveries can be obtained when fractures are wider, and that the assumption of zero capillary pressure in the fracture is incorrect especially for air and water. The assumption of fracture relative permeabilities equal to the phase saturation was tested. This work shows that straight-line fracture relative permeability can be used, but it is not necessarily equal to the phase saturation. X-type relative permeability curves can be used for fractured system using larger flow resistances in the fractures, such as 0.75 or 0.6 sloped straight

lines instead. Our results show that the best matches are achieved when a slope of 0.6 is used.

This work has shown that both capillary and viscous forces dominate the flow in fractures. Moreover, a procedure for determining the parameters involved in transmissibility and the transfer terms that appear in the flow equations in finite difference form was established.

The reader should realize that experiments presented in this work were performed only once. We assumed that our results were correct because they were comparable to Hughes (1995) results, and we could reproduce the experiments very accurately by numerical simulations. However a repeatability test should be performed on these experiments to achieve a higher certainty of the conclusions presented here.

Conclusions

The results of the combined experimental and the simulation study show:

1.Areas with lower permeability and porosity can be identified and used in numerical simulation.

2. Thin fractures systems showed more stable fronts and slower breakthrough compared to wide fracture systems.

3. Capillary pressure has more effect when the fractures are narrow.

4. Larger recoveries can be obtained when the fractures are wider.

5. Assuming zero capillary pressure in the fracture is incorrect.

6. X-type relative permeability curves can be used for fractured systems using high resistance through fractures, but relative permeability is not equal to phase saturation.

Nomenclature

CT = CT scanner number
S = saturation
ϕ = porosity

Subscripts

a = air
aw = air and water saturated
cd = dry core
cw = 100% water saturated
ow = oil and water saturated
w = water

Acknowledgments

This work is supported by U.S. Department of Energy under contract No. DE-FG22-96BC14994, SUPRI-A Industrial Affiliates and Consejo Nacional de Ciencia y Tecnología (CONCACyT), México.

We thank Anthony Kovseck, Richard Hughes and William Brigham of Stanford University for valuable discussions and advice.

References

1. Ameri, H. and Wang, J.: "Effect of Temperature on Oil-Water Relative Permeability," SUPRI Heavy Oil Research Program, Eighth Annual Report, SUPRI TR-47, (April 1985), 11-24.
2. Beckner, B.L.: Improved Modeling of Imbibition Matrix/Fracture Fluid Transfer in Double Porosity Simulators, PhD dissertation, Stanford University (July 1990)
3. Buckley, S.E. and Leverett, M.C.: "Mechanisms of Fluid Displacement in Sands," Transactions American Institute of Mining and Metallurgical Engineers, 146 (1942), 107-116.
4. Eclipse 100 User's Manual, Intera Information Technology Limited, Oxfordshire, England, 1994.
5. Firoozabadi, A. and Hauge, J.: "Capillary Pressure in Fractured Porous Media," JPT (June 1990) 784-791.
6. Firoozabadi, A. and Markeset, T.: "An Experimental Study of Capillary and Gravity Crossflow in Fractured Porous Media," SPE 24918, presented at the 67th SPE Annual Technical Conference and Exhibition, Washington, D.C., October 4-7, 1992.
7. Gilman, J.R., Bowzer, J.L. and Rothkopf, B.W.: "Application of Short-Radius Horizontal Boreholes in the Naturally Fractured Yates Field," SPE 28568, presented at the 69th SPE Annual Technical Conference and Exhibition, New Orleans, LA, September 25-28, 1994.
8. Guzman, R.E. and Aziz, K.: Design and Construction of an Experiment For Two-Phase Flow in Fractured Porous Media, SUPRI TR-95, Stanford Petroleum Research Institute, Stanford, CA, (June 1993).
9. Horie, T., Firoozabadi, A. and Ishimoto, K.: "Capillary Continuity in Fractured Reservoirs," SPE 18282, presented at the 63rd SPE Annual Technical Conference and Exhibition, Houston, TX, October 2-5, 1988.
10. Hughes, R.G.: CT Measurements of Two-Phase Flow in Fractured Porous Media, Masters Report, Stanford University (December 1995).
11. Kazemi, H. and Merrill, L.S.: "Numerical Simulation of Water Imbibition in Fractured Cores," SPEJ (June 1979) 175-182.
12. Kazemi, H.: Naturally Fractured Reservoirs, Third International Forum on Reservoir Simulation, Baden, Austria (1990).
13. Labastie, A.: "Capillary Continuity Between Blocks of a Fractured Reservoir," SPE 20515 presented at the 65th SPE Annual Technical Conference and Exhibition, New Orleans, LA, September 23-26, 1990.
14. Pan, X. and Wong, R.C.: "Steady State Two-phase in a Smooth Parallel Fracture," presented at the 47th Annual Technical Meeting of The Petroleum Society in Calgary, Alberta, Canada, June 10-12, 1996.

15. Persoff, P., Pruess, K., and Myer, L.: "Two-Phase Flow Visualization and Relative Permeability Measurement in Transparent Replicas of Rough-Walled Rock Fractures," Sixteenth Workshop on Geothermal Reservoir, Stanford University (January 1991).
16. Purcell, W. R.: "Capillary Pressures - Their Measurement Using Mercury and the Calculation of Permeability Therefrom," *Trans, AIME, 186, 39* (1949).
17. Rangel-German, E.: Experimental and Theoretical Investigation of Multiphase Flow in Fractured Porous Media, Masters Report, Stanford University (June 1998).
18. Sanyal, S.K.: The Effect of Temperature on Electrical Resistivity and Capillary Pressure Behavior of Porous Media, Ph.D. dissertation, Stanford University (December 1971).
19. Withjack, E.M.: "Computed Tomography for Rock-Property Determination and Fluid-Flow Visualization", SPEFE (December 1988) 696-704.

TABLE 1. RATES AND TIMING FOR THE CORE WITH NARROW FRACTURE

Fluid Injected	Time (hrs)	Flow Rate (cm^3/min)	Ports
Water	**0.0 - 4.0**	**2.0**	**Top and bottom closed, lateral open.**
Water	**4.0 - 5.0**	**2.0**	**Top and bottom open, lateral closed.**
Water	**5.0 - 19.8**	**0.5**	**Top and bottom open, lateral closed.**
Water	**19.8 - 23.0**	**2.0**	**Top and bottom closed, lateral open.**
Decane	**23.0 - 27.0**	**2.0**	**Top and bottom closed, lateral open.**
Decane	**27.0 - 28.0**	**2.0**	**Top and bottom open, lateral closed.**
Decane	**28.0 - 44.7**	**1.0**	**Top and bottom open, lateral closed.**
Water	**44.7 - 46.0**	**9.99**	**Top and bottom closed, lateral open.**
	46		**Shut down everything**

TABLE 2. RATES AND TIMING FOR THE CORE WITH WIDE FRACTURE

Fluid Injected	Time (hrs)	Flow Rate (cm^3/min)	Ports
Water	0.0 - 5.0	2.0	Top and bottom closed, lateral open.
	5.0 - 21.0	0.0	Top and bottom closed, lateral closed.
Water	21.0 - 22.5	2.0	Top and bottom open, lateral closed.
Water	22.5 - 25.6	2.0	Top open, bottom closed, and lateral closed.
	25.6 - 45.0	0.0	Top and bottom closed, lateral closed.
Decane	45.0 - 48.0	2.0	Top and bottom closed, lateral open.
Decane	48.0 - 49.2	4.0	Top and bottom closed, lateral open.
Decane	49.2 - 51.0	4.0	Top and bottom open, lateral closed.
	51.0 - 52.0	0.0	Top and bottom closed, lateral closed.
Water	52.0 - 54.3	4.0	Top and bottom closed, lateral open.
Water	54.3 - 68.8	0.5	Top and bottom closed, lateral open.
Water	68.8 - 71.0	4.0	Top and bottom open, lateral closed.
	71		Shut down everything

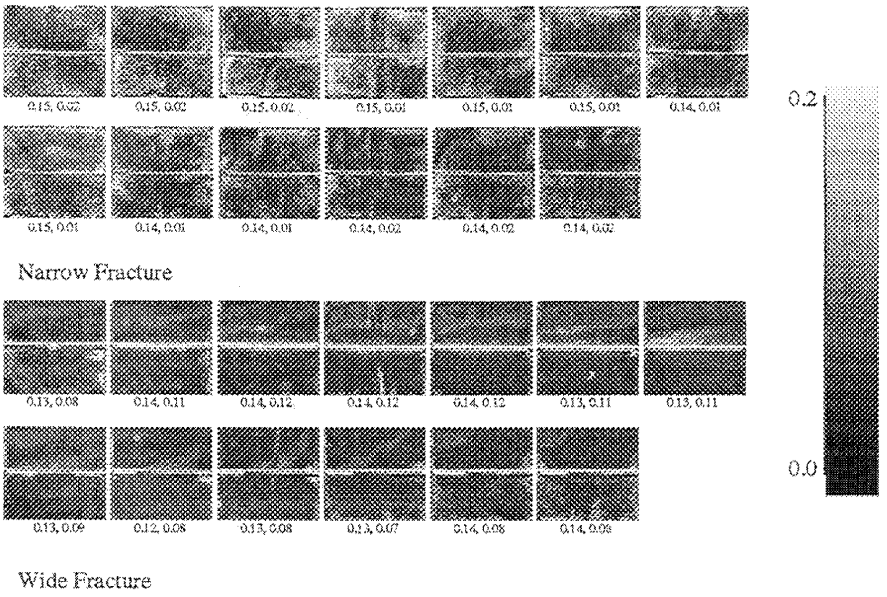

Fig. 5- Porosity distribution for the experimental system.

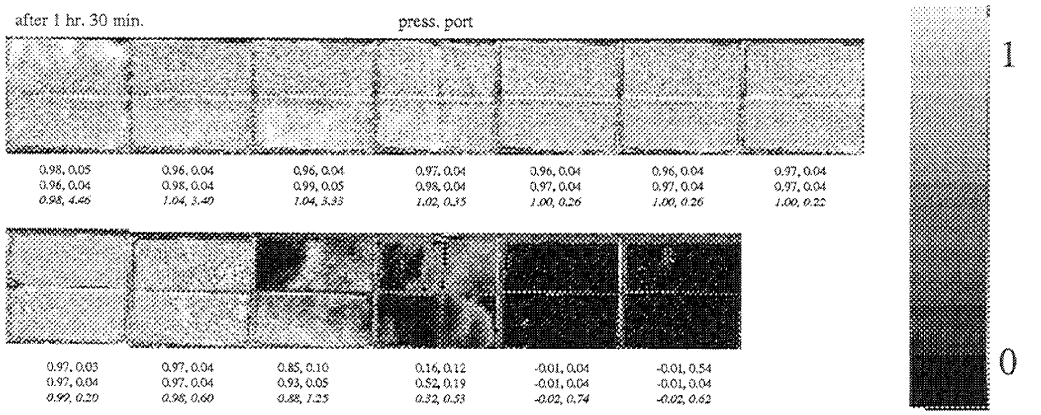

Fig. 6- CT Saturation images for the thin fracture system after 1 hr 30 min of water injection (0.67 PV.)

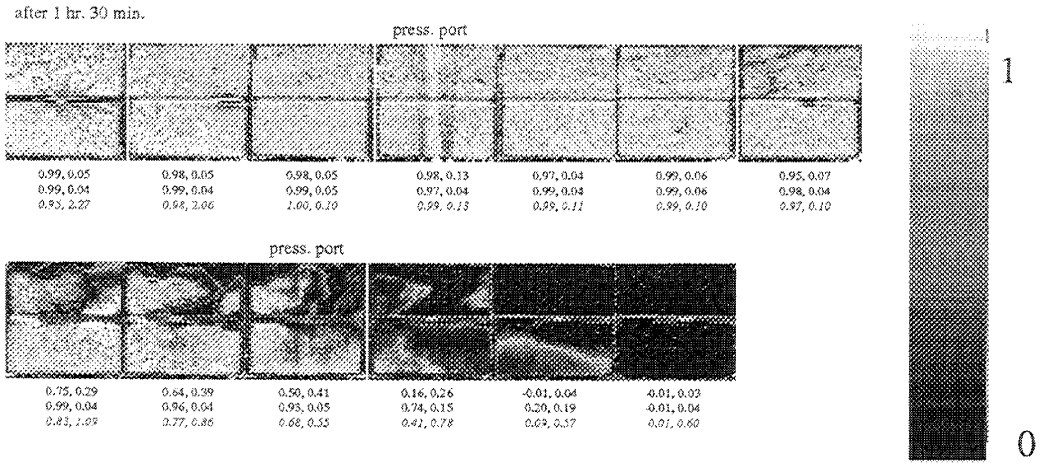

Fig. 7- CT Saturation images for the wide fracture system after 1 hr 30 min of water injection (0.67 PV.)

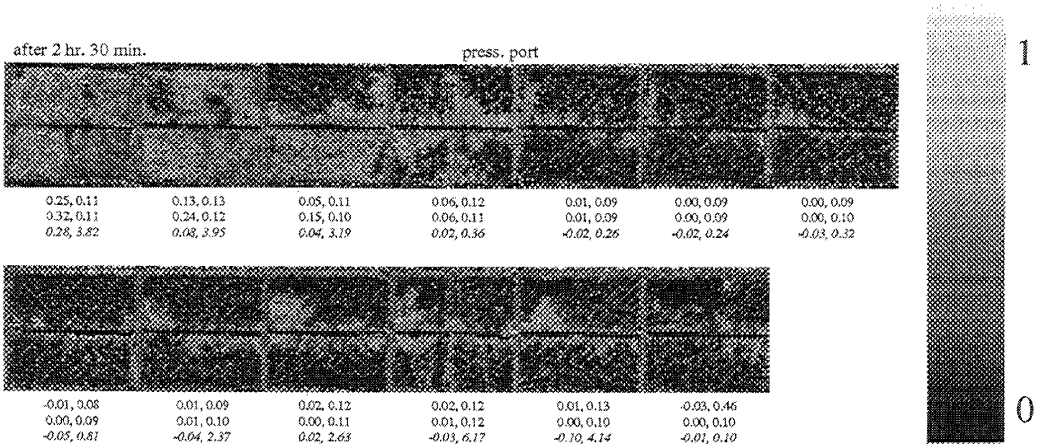

Fig. 8- CT Saturation images for the narrow fracture system after 2 hr 30 min of oil injection (1.13 PV.)

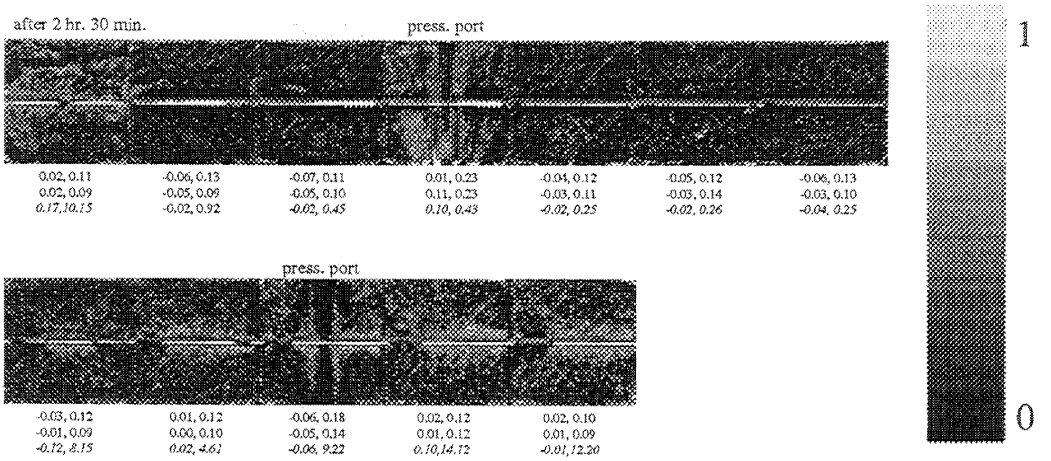

Fig. 9- CT Saturation images for the wide fracture system after 2 hr 30 min of oil injection (1.13 PV.)

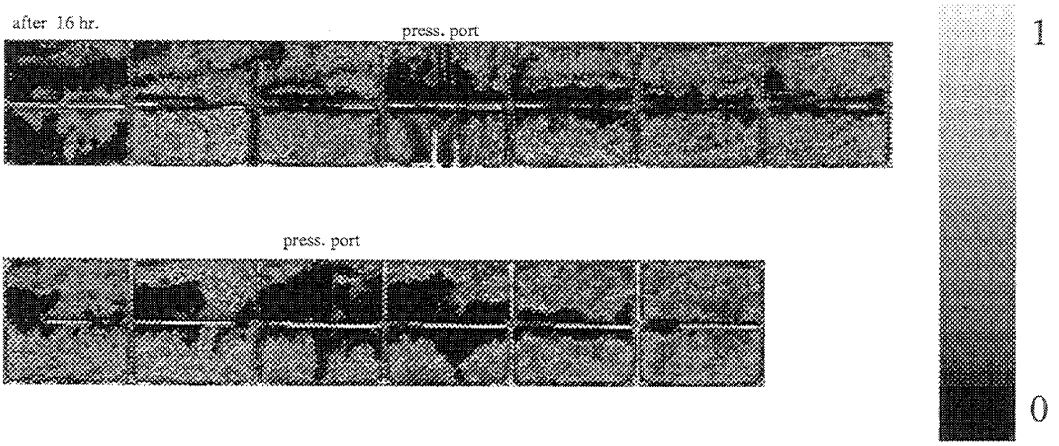

Fig. 10- CT Saturation images for the wide fracture system after 16 hours of water injection (7.2 PV.)

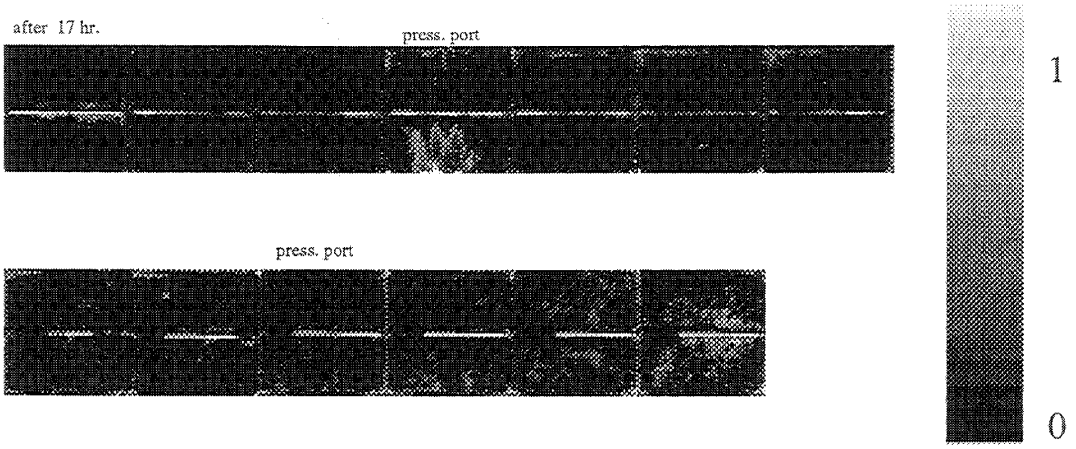

Fig. 11- CT Saturation images for the wide fracture system after 17 hours of water injection (7.7 PV.)

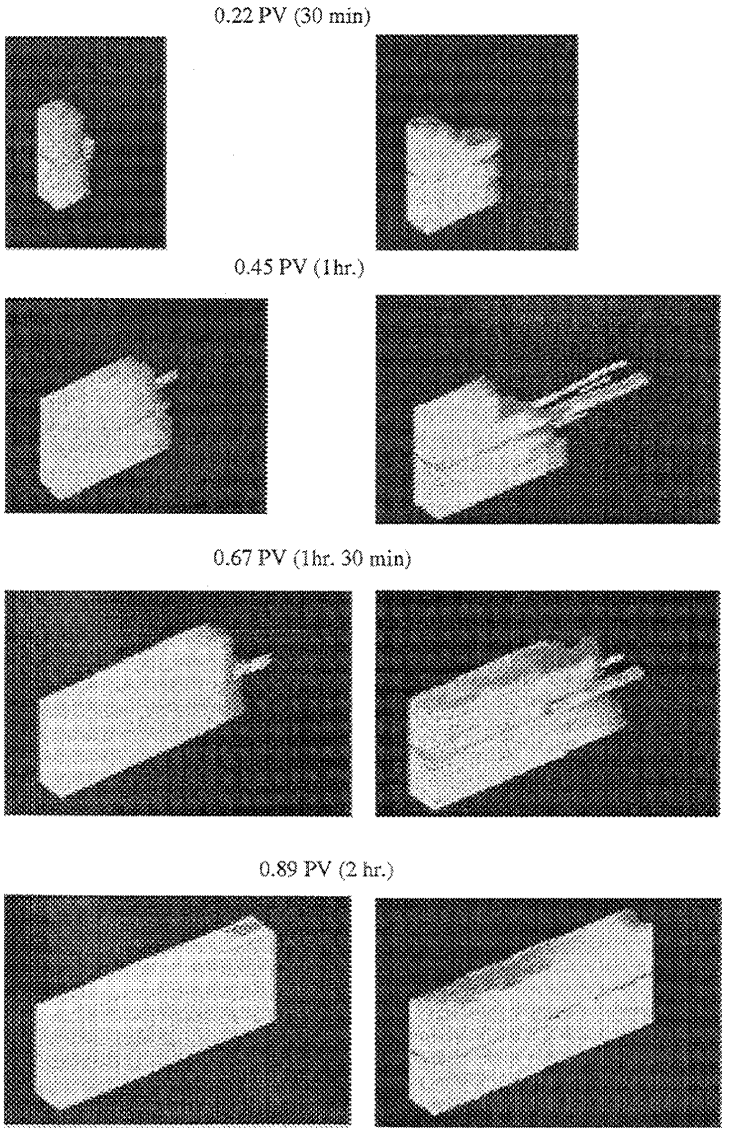

Fig. 12- 3-D Reconstruction for both systems for water injection.

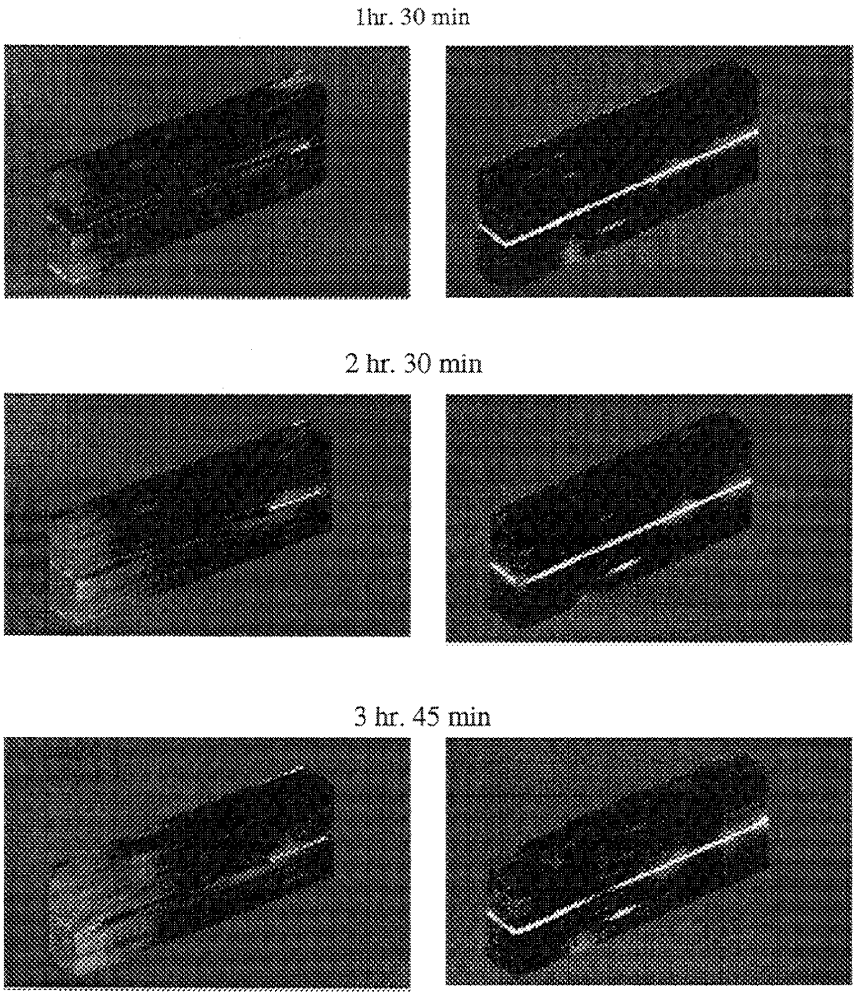

Fig. 13- 3-D Reconstruction for both systems for oil injection.

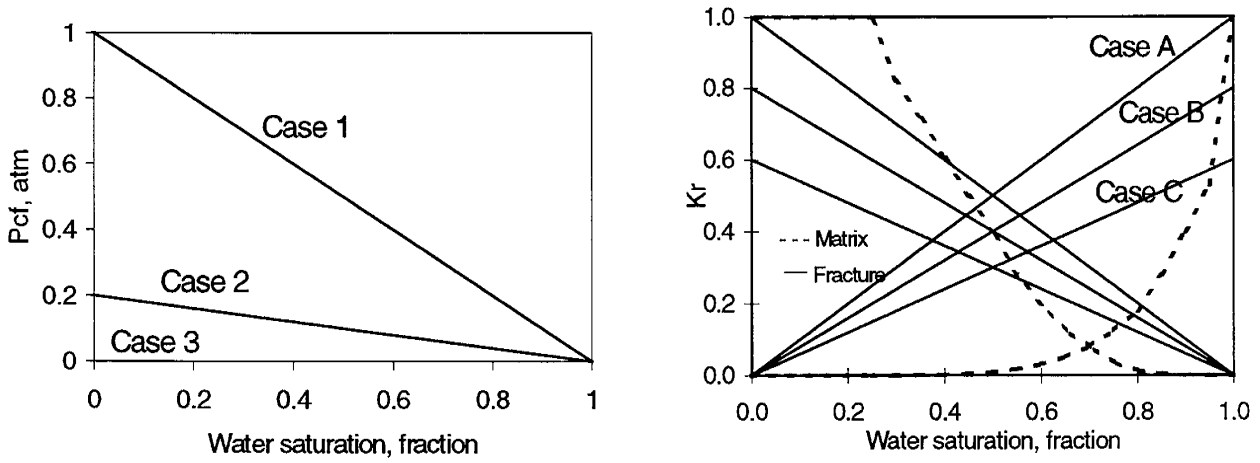

Fig. 14- Capillary pressure curves and relative permeability curves for the fracture.

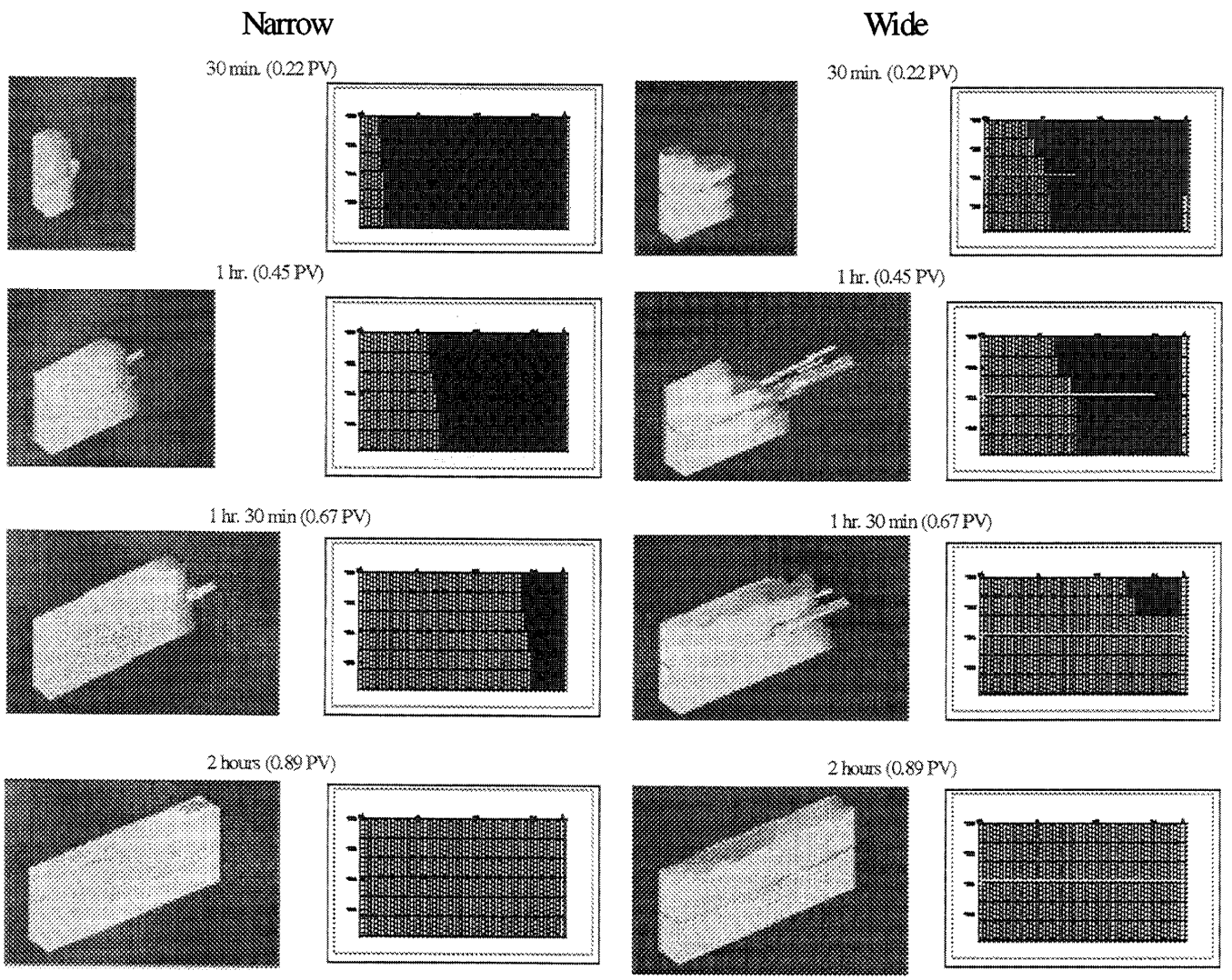

Fig. 15- Comparison between experiments and numerical simulations for narrow and wide fracture systems for different PV of water injection.

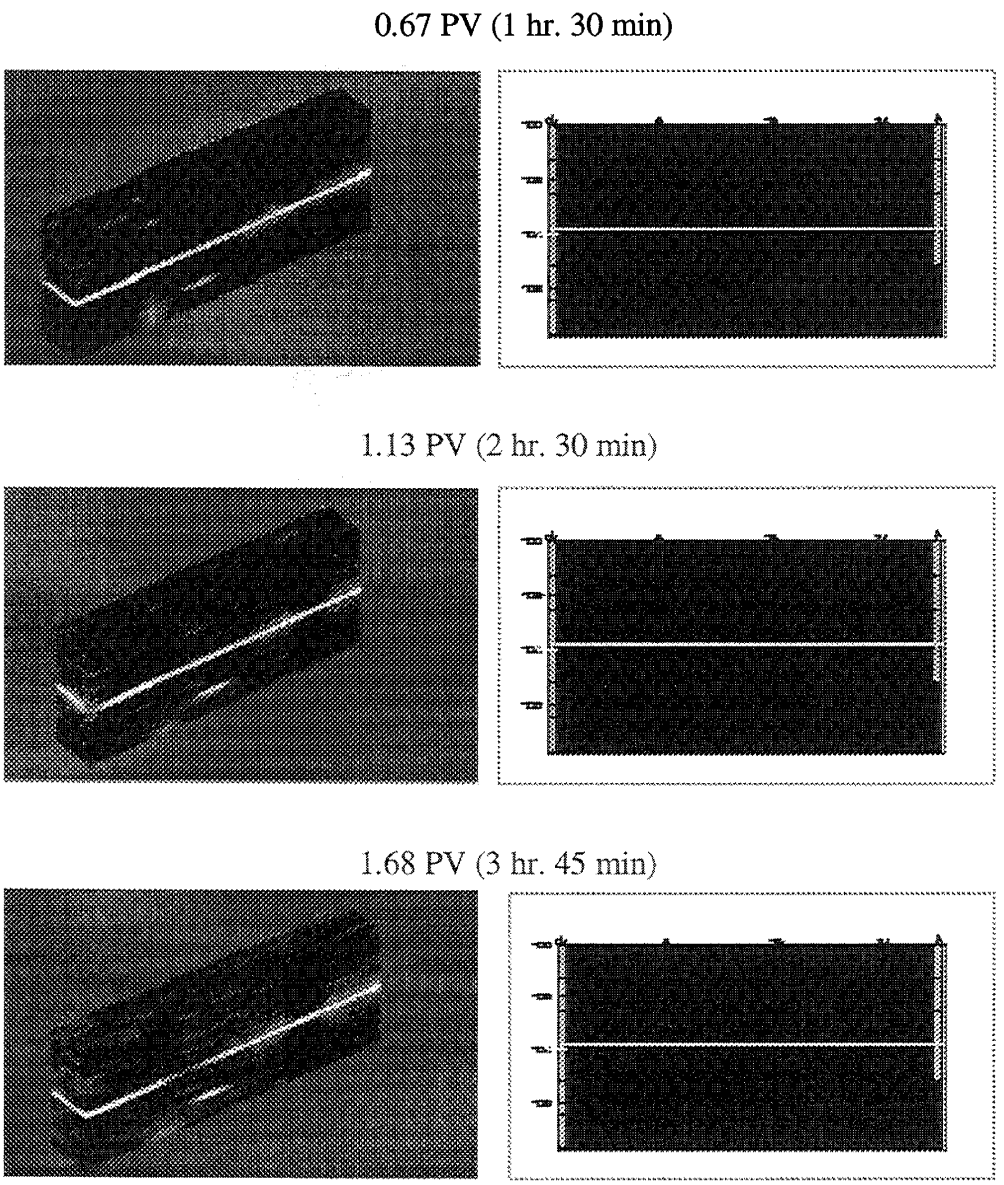

Fig. 16- Comparison between experiments and numerical simulations for narrow and wide fracture systems for different PV of water injection.

PROJECT 2: IN-SITU COMBUSTION

To evaluate the effect of different reservoir parameters on the in-situ combustion process. This project includes the study of the kinetics of the reactions.

2.1 IN-SITU COMBUSTION

(Louis Castanier)

2.1.1 INTRODUCTION: ADVANTAGES OF IN-SITU COMBUSTION

By far the most widely used recovery method for heavy oils is steam injection either cyclic or as a drive. Steam injection, however is not applicable to many reservoirs. Among the parameters affecting the success of steam injection are depth. If the reservoir depth is over 3,000 ft (1,000m) the heat losses in the injection well will make the steam injection inefficient. Insulated tubing can be used as a partial remedy, but it is expensive and difficult to install properly in the field. Downhole steam generators have been tried without success in the last 20 years. They suffer from reliability problems. Additional parameters include:

- Pressure: At high pressure the latent heat going from water to steam drastically decreases and high pressure also means high injection temperature causing less efficient heat transport and added heat losses.
- Permeability: Clays present in the reservoir may swell in presence of the fresh water produced by steam condensation. This can reduce injectivity and impair the process.
- Oil Saturation and Porosity: These two parameters are very important. If not enough oil is in place, the energy used to heat the reservoir can be more than the energy obtained by the oil produced. Steam injection is generally uneconomic in reservoirs where the product of porosity by oil saturation is less than about 0.1.

From the above discussion it is clear that despite its usefulness, steam injection is limited to a select group of reservoirs. Let us now turn our attention to in-situ combustion. In-situ combustion is not limited by reservoir depth. It is also applicable where wellbore heat transfer would severely limit steam injection. Two possible cases would be offshore fields and/or the presence of permafrost where steam is not applicable

but combustion would be feasible. Combustion is more energy efficient and less polluting than steam. This has been field proven in a number of countries. Combustion, however, suffers from poor sweep efficiency caused by the mobility contrast between the injected air (or oxygen) and the reservoir fluids. It also requires careful engineering and is less flexible and forgiving of errors than steam. Research on in-situ combustion is needed to better understand and engineer the process.

2.1.2 IN-SITU COMBUSTION WITH METALLIC ADDITIVES

This is part of an ongoing effort aimed at finding water soluble metallic additives to improve in-situ combustion. The planned program of research for this year involved several tube runs designed to obtain insight on the transport of metallic additives during in-situ combustion. After a control run that failed due to poor thermal insulation around the tube, we found out that the twenty year old carbon monoxide and carbon dioxide gas analyzers could not be properly calibrated. Despite attempts to repair them, they have to be replaced. We are presently investigating the analyzers available from different suppliers and will purchase new models. The experiment will be restarted with a new researcher next fall.

2.1.3 IN-SITU COMBUSTION AND SOLVENTS: POSSIBLE RESEARCH

Solvents can be used to reduce the oil viscosity and facilitate production. The solvents can be gases used in miscible or non-miscible mode, or liquids at reservoir conditions. Liquid solvents are usually expensive, while the sales price of the oil recovered is low. Consequently, the economics of liquid solvent injection are usually not favorable. Gases are used in miscible or non-miscible modes. Miscibility of gases with heavy oils require very high pressures. Again the economics of miscible flooding of heavy oils are not good. Non miscible gas injection has been tried with some success, especially in a cyclic fashion. Some of the technical problems involved with solvent injection arise from precipitation of asphaltenes or other compounds during the mixing of

the oil and the solvent. This phenomenon is well known and described in a number of publications. It leads to reduction in near well permeability, that can be very severe and cause technical failure of the process. We expect this problem to be acute with heavy oils.

A combination of several of the existing techniques could solve this problem. The economic aspects have been taken into account in our preliminary study and we feel that the proposed improved oil recovery ideas can be applied in the field with existing technology.

We propose cyclic injection of solvents, either gas or liquid, followed by in-situ combustion of a small part of the reservoir to increase the near-well temperature and also to clean the well-bore region of the residues left by the solvents. Alternate slugs of solvent and air will be injected, and production will occur after each solvent slug injection and after each combustion. The process can be repeated until the economic limit is reached. One important fact to note is that both solvent injection and in-situ combustion have been proven to be effective in a variety of reservoirs, the combination of the two methods has, however, never been tried to our knowledge.

At the end of the first solvent cycle, one can expect some damage to the near wellbore area. Most significant will be the precipitation and/or deposition of heavy hydrocarbons such as asphaltenes or paraffins. The produced oil is expected to be slightly upgraded by the solvent cycle.

Unlike the classic well to well in-situ combustion, we will only try to improve near well conditions by burning the solid residues left after the solvent cycle. The amount of air (or oxygen) to be injected can be determined by laboratory experiments and numerical simulation or by simple calculations. The benefits of using combustion at this stage are expected to include:

- Productivity improvement through removal of the precipitants left from the solvent cycle.
- Possible deactivation of the clays near wellbore caused by the high temperature of the combustion.
- Reduced viscosity of the oil due to temperature increase.

- Effect of CO_2 production causing swelling and viscosity reduction of the oil. This is expected to be important only when oxygen combustion is tried.
- Pressure maintenance

One must note that combustion burns only the heaviest part of the crude and hence, the upgrading already observed during the solvent cycle should be maintained and even improved. A soak period will probably be necessary at the end of the air/oxygen injection to ensure that all of the oxygen injected will have reacted in the reservoir and will not be produced during the subsequent production cycle. The process can be repeated by alternating solvent injection and near well in-situ combustion as long as the economics warrants it. Slug sizes and duration need to be optimized to ensure maximum economic efficiency. Reservoir conditions will, of course, dictate these parameters.

During the solvent injection, the main problem will be the efficient use of a limited amount of expensive injected fluid. Reservoir heterogeneities and density and mobility differences between solvent and reservoir oil will cause sweep efficiency problems. This in turn can cause concentration gradients and hence large viscosity differences among the fluids to be produced. As in any improved recovery technique, proper reservoir definition is needed. The fact that the process is cyclic in nature should ensure no waste of solvent. The other problems to be encountered in the solvent part of the process are well known and described in the literature. The type of work required prior to field application involves PVT studies and creation in the laboratory of various oil/solvent mixtures. Deposition of asphaltenes or other residues on rocks similar to reservoir rocks should also be studied. The following describes some simple tests that can be used as screening techniques for the method:

Heavy crudes such as Cold Lake, Kern River or Hamaca will be mixed with liquid solvents and viscosities of the mixtures will be measured. Filtration of the mixtures should determine whether or not solid precipitation or formation damage would occur. If it occurs, the mixtures will be injected through a sand pack of permeability and pore structure close to the field sands. Permeability variation will be recorded as a function of injection. When (and if) the ratio of the permeabilities before and after passage of the mixes have reached a given value, the sand pack will be subjected to an in-situ combustion tube run. Fuel concentration and composition as well as an estimate of

the air requirements will be obtained. Problems such as possible coking and plugging of the reservoir can be studied. At this stage, simple calculations will give estimates on the production in the field. Economic evaluation should start at this level. Laboratory tests for gas in solution type situations may be more difficult to implement. The literature is poor in PVT data for heavy oils and more complex experiments may be required. A significant research effort is being made on the "foamy oil" problem and data from those experiments can probably be used in our project. The database of heavy oil with CO_2 projects will also be used.

PROJECT 3: STEAM WITH ADDITIVES

To develop and understand the mechanisms of the process using commercially available surfactants for reduction of gravity override and channeling of steam.

3.1 SIMULATION OF EARLY-TIME RESPONSE OF SINGLE-WELL STEAM ASSISTED GRAVITY DRAIN (SW-SAGD)

(Keith Elliott)

3.1.1 SIMULATION OF EARLY-TIME RESPONSE OF SINGLE-WELL STEAM ASSISTED GRAVITY DRAIN (SW-SAGD)

(K.T. Elliott and A.R. Kovscek)

This paper, SPE 54618, was presented at the1999 SPE Western Regional Meeting held in Anchorage, Alaska, May 26-28, 1999.

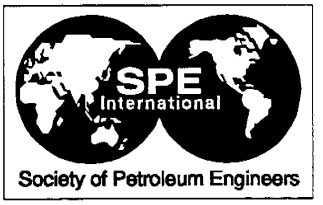

SPE 54618

Simulation of Early-Time Response of Single-Well Steam Assisted Gravity Drainage (SW-SAGD)

K.T. Elliott and A. R. Kovscek, Stanford University, SPE Members

Copyright 1999, Society of Petroleum Engineers Inc.

This paper was prepared for presentation at the 1999 SPE Western Regional Meeting held in Anchorage, Alaska, 26–28 May 1999.

This paper was selected for presentation by an SPE Program Committee following review of information contained in an abstract submitted by the author(s). Contents of the paper, as presented, have not been reviewed by the Society of Petroleum Engineers and are subject to correction by the author(s). The material, as presented, does not necessarily reflect any position of the Society of Petroleum Engineers, its officers, or members. Papers presented at SPE meetings are subject to publication review by Editorial Committees of the Society of Petroleum Engineers. Electronic reproduction, distribution, or storage of any part of this paper for commercial purposes without the written consent of the Society of Petroleum Engineers is prohibited. Permission to reproduce in print is restricted to an abstract of not more than 300 words; illustrations may not be copied. The abstract must contain conspicuous acknowledgment of where and by whom the paper was presented. Write Librarian, SPE, P.O. Box 833836, Richardson, TX 75083-3836, U.S.A., fax 01-972-952-9435.

Abstract

Steam assisted gravity drainage (SAGD) is an effective method of producing heavy oil and bitumen. In a typical SAGD approach, steam is injected into a horizontal well located directly above a horizontal producer. A steam chamber grows around the injection well and helps displace heated oil toward the production well. Single-well (SW) SAGD attempts to create a similar process using only one horizontal well. This may include steam injection from the toe of the horizontal well with production at the heel. Obvious advantages of SW-SAGD include cost savings and utility in relatively thin reservoirs. However, the process is technically challenging.

To improve early-time response of SW-SAGD, it is necessary to heat the near-wellbore area to reduce oil viscosity and allow gravity drainage to take place. Since project economics are sensitive to early production response, we are interested in optimizing the start-up procedure.

An investigation of early-time processes to improve reservoir heating will be discussed. We performed a numerical simulation study of combinations of cyclic steam injection and steam circulation prior to SAGD in an effort to better understand and improve early-time response. Results from this study, including cumulative recoveries, temperature distributions, and production rates display variances within the methods. It is found that cycling steaming of the reservoir prior to SAGD offers the most favorable option for heating the near-wellbore area and creating conditions that will improve initial SAGD response.

Introduction

Background. Steam assisted gravity drainage maximizes the role of gravity forces during steam flooding of heavy oils. Generally, it is applied with a pair of horizontal wells. Single-well steam assisted gravity drainage is similar in concept to conventional SAGD. As steam enters the reservoir, it heats up the reservoir fluids and surrounding rock, allowing hot oil and condensed water to drain though the force of gravity to a production well at the bottom of the formation. Heat is transferred by conduction, convection, and latent heat of the steam. In conventional SAGD, steam is typically injected through a horizontal injection well placed directly above a horizontal production well. Thus, a steam chamber forms directly above the production well. In SW-SAGD, we attempt to create the same recovery mechanism through the use of a single horizontal well. In a typical case, steam is injected at the toe of the well, while hot reservoir fluids are produced at the heel of the well.

In a reservoir where cold oil is very viscous and will not flow easily, initial production rates via SAGD are very low. Conceptually this makes sense when the SAGD process is visualized. In a strict definition of SAGD, steam only enters the reservoir to fill a void space caused by produced oil. However, if the oil is cold and will not gravity drain into the wellbore at appreciable rates, we must heat the oil to reduce the viscosity so that it will flow. Therefore, initial heating of the area around the wellbore is required so that SAGD can take place.

After SAGD is initiated, a steam chamber will grow in the reservoir. Butler notes that the steam chamber will initially grow upward to the top of the reservoir and then begin extending horizontally.[1] At the steam-chamber boundary, steam condenses to water as heat is transferred to the oil. Condensed water and hot oil flow along the steam chamber to the production well.[1]

Joshi found that under various injection/production well configurations, the steam chamber will eventually grow to cover a majority of the reservoir and the recovery efficiencies will be very good in all cases.[2] Therefore, we expect that early-time production results from SW-SAGD may vary from the conventional approach, but at late times we expect similar recovery efficiencies. Additionally, Oballa and Buchanan[3] simulated various scenarios to evaluate the difference between cyclic steam injection and SAGD. They focused, partially, on the interactions between the reservoir, the well completion, and the recovery of oil. It was concluded that the drainage process may be feasible provided that a proper operating strategy is identified.

Very few of the field tests of SW-SAGD are documented in the literature; however an overview of the completion strategy and some typical results is given by Falk *et al*[4]. For example, a roughly 850 m long well in a section of the Cactus Lake Field, Alberta Canada with 12 to 16 m of net pay was installed to produce 12 °API gravity oil. The reservoir is a clean, unconsolidated, 3400 md permeability sand. Oil production response to steam was slow and gradually increased to more than 100 m^3/d. The cumulative steam-oil ratio was between 1 and 1.5 for the roughly one-half year of reported data.

One advantage of SW-SAGD, as in the Cactus Lake example, is that it may allow us to apply SAGD to thinner reservoirs where it is not possible to drill two vertically spaced horizontal wells[4]. Furthermore, cost savings associated with drilling one horizontal well rather than two are substantial.

Problem Definition. This paper is focused on understanding operating conditions to improve the crucial early-time performance of SW-SAGD. This relates directly to understanding methods of heating the near-wellbore area at early-time. The central idea used throughout this paper is that the near-well region must be heated rapidly and efficiently for significant early-time response.

Methodology. We gained an understanding of early-time performance through building and comparing various computer simulations. The early-time processes examined include cyclic steaming, steam circulating, and an extreme pressure differential between the injector and producer sections of the well. Each initial operating period was followed by SAGD. Computer Modeling Groups's (CMG) STARS thermal simulator is used to perform the work.

Model Description

The base case is STARS example *sthrw009.dat* released with Version 98.01. It represents a typical Alberta reservoir[5]. The operating conditions and well completion are modified to develop additional cases.

Grid System. Fig. 1 displays cross-sections along the length of the well (Fig. 1a) and perpendicular to the well (Fig. 1b). The grid system is Cartesian with local grid refinement immediately around the 800 m long well. An element of symmetry, with one boundary lying along the wellbore, is used to represent the reservoir volume. We assume that wells will be developed in multiple patterns and thus all boundaries are no flux. The single horizontal well is modeled using two individual discretized wellbores, each equal in length and placed directly end to end. This gives us freedom to explore various completion strategies and operating conditions. **Table 1** lists the exact dimensions of the reservoir model, grid-block information, and reservoir properties. Initially, the average reservoir pressure is 2,654 kPa, the pressure distribution is hydrostatic, and the reservoir temperature is 16 °C.

Rock Properties. Reservoir properties are also given in Table 1. **Figs. 2 and 3** display graphically the water-oil relative permeability and gas-liquid relative permeability curves, respectively. **Table 1** displays the porosity and initial saturations of the reservoir. The horizontal permeability, K_h, is 3400 md, whereas the vertical permeability, K_v, is 680 md. Hence, the ratio K_h:K_v is about 5 to 1. The homogeneous porosity is 33%.

Fluid Properties. A live, black-oil model is used. The initial oil phase is made up of 90% by mole oil component and 10% gas component. Oil viscosity at the initial reservoir temperature is 4000 mPa-s. **Figure. 4** displays the viscosity versus temperature relationship. An increase of oil temperature to 100 °C decreases the oil viscosity to 30 mPa-s.

Operating Conditions. Table 2 lists the operating constraints for the four base cases created to explore a range of early-time procedures. Briefly the cases represent SAGD operating conditions, extreme pressure differential conditions where steam is injected near the fracturing or parting pressure, cyclic steam injection, and steam circulation through the well. Arbitrarily, 100 d was chosen as the duration of attempts to heat the near-well region. In all cases, SAGD conditions follow. Each of the constraints will be discussed in more detail in the *Results and Discussion* Sections.

Results

Overview. In an attempt to heat the near-wellbore area and improve the initial production response of SAGD, we combined the operating conditions displayed in Table 2 into the various cases displayed in **Table 3**. There are four operating condition scenarios and seven cases overall. In each case, an initial preheating phase precedes SAGD.

Fig. 5 displays recovery factor versus time curves for each case. Case 1 represents a base case in which SAGD was initiated from the beginning without a preheating phase. This case produced the lowest percent recovery curve. It is obvious from the curves that it is possible to improve drastically initial production response. In general, cyclic steaming leads to most rapid oil recovery. We discuss Cases 1—Continuous SAGD, 2—Extreme Pressure Differential, and 5—Cyclic Steam Injection in more detail to gain insight into the early-time behavior. The late-time production behavior is also examined.

Case 2 is a modified form of steam circulation in the well. We did not simulate true steam circulation where steam exiting the tubing is allowed only to flow in the well before it is produced. A true circulating case in which the near-wellbore area is heated only by conduction would be inefficient, and the other techniques that we explore present better options. Circulation here is similar to the SAGD case: steam may replace oil volume in the reservoir when oil is produced. Hence, our "circulating" condition is somewhat of a misnomer.

Case 1, Continuous SAGD. In Case 1 we immediately operate at SAGD conditions and do not include a preheat phase. In this case, and the cases to follow, production rates, well pressures and temperature profiles around the well are examined. **Fig. 6** displays the injection and production curves for Case 1. The darkest curve in Fig. 6 represents the oil production rate. As expected, the initial oil rate is low, but increases with time as a steam chamber slowly develops and more oil is heated. Oil production peaks at roughly 80 m^3/day

Note that our "SAGD" case is actually a combination of SAGD and pressure draw-down. Production well conditions are such that reservoir pressure must decline. It is clear from the similarity between the steam injection rate and water production rate in Fig. 6 that steam short-circuits from the injection well to the production well and the contact time for steam with the reservoir is short. Recall that in our model we represent the horizontal well with two separate sections placed end-to end. The pressure differential between the wells and the proximity of "injection" and "production" perforations causes steam to travel immediately the short distance through the reservoir from the injection well to the production well. Increasing the spacing between the injection and production points and/or reducing the pressure differential would certainly reduce the amount of short-circuiting. Albeit inefficiently, a steam chamber is created within the reservoir as heated oil drains to the production well and steam migrates up to fill the void space. Optimizing the well spacing and pressure drawdown represents another interesting problem that we are currently addressing.

Fig. 7 displays bottom-hole pressure curves for injection and production in Case 1. A large pressure differential of about 2000 kPa exists between the two sections of the well. Over time, the reservoir pressure decreases because we produce more fluids than we inject. This also causes the injection pressure to decrease.

Fig. 8 displays a temperature profile at 100 days for Case 1. Light shading corresponds to high temperature and dark shading to low temperature. At late times, a large steam chamber grows in the middle region of the system. At this point, however, the steam chamber is just beginning to grow above the short-circuiting area between the injection and production sections. We will see that the same profile at similar relative times in the other cases displays a much larger heated area. It is important to maximize the amount of net heat injection into the reservoir at early times, therefore, maximizing the size of the heated volume surrounding the wellbore.

Case 2, Extreme Pressure Differential Prior to SAGD. In the extreme pressure differential case we increase the injection rate constraint which thereby increases the pressure differential between the injection and production wells. **Fig. 9** displays the bottom-hole pressure versus time curves. For the first 100 d, steam is injected at roughly 7000 kPa forcing steam into the formation and increasing the average reservoir pressure. **Fig. 10** displays the production response for the extreme period in the first 100 days followed by SAGD operating conditions. Observing the oil rate in the first 100 days and comparing to Fig. 6, we see that the oil rate ramps up faster than Case 1. This is logical because Case 2 is an accelerated version of SAGD.

Fig. 9 also indicates that a very high injection bottom-hole pressure is obtained between 0 and 100 d of injection. High pressure results because the water production rate is substantially less than the steam injection rate, as shown in Fig. 10. Under the given conditions a limited amount of steam short-circuits, and an appreciable amount of steam enters the reservoir and increases the reservoir pressure.

If we view the oil production rate in Fig. 10 during and after the extreme period, it is obvious that we have improved response. Direct comparison of Cases 2 and 1 is somewhat misleading. Injection conditions have lead to high reservoir pressure at the beginning of SAGD, causing significant production through pressure depletion in addition to gravity drainage of heated reservoir heating fluids. A better comparison is the temperature profile along the length of the well displayed in **Fig. 11.** The profile represents a relative time similar to similar to the Case 1 profile, 100 days after SAGD inception. Again, light shading is high temperature and dark shading is low temperature. The profile for Case 2 is much more favorable. There is a larger heated area and the corresponding steam chamber is larger. The steam chamber forms in the middle of the well because pressure drawdown is large in this vicinity and in this region the steam flux into the reservoir is largest.

Case 5, One Cycle Prior to SAGD. Our cyclic case is very similar to typical cyclic operations common in many thermal recovery operations. We inject steam along the entire well for 50 days, let it soak for 10 days, then produce along the entire length of the well for 120 days. The injection and production profiles in **Fig. 12** summarize this cycle of steam injection, shut in, production.

Fig. 13 shows that the bottom-hole pressure increases to about 8000 kPa during the injection phase, but still remains within a feasible range. Because the oil is very viscous, this energy is rapidly depleted from the reservoir. From the oil production rate after the cycling period in Fig. 12, it is again obvious that we have improved SAGD response. The slow increase of production rate found in Case 1 is not evident here. The minimum production rate at roughly 200 d occurs because reservoir pressure is depleted somewhat following the cyclic

period, as shown by the plot of well bottom hole pressure in Fig. 13. Again, the maximum oil production rate is about 80 m^3/day. In this case, the reservoir pressure at SAGD inception is similar to that in Case 1. Therefore we conclude that SAGD performs better because the near-wellbore area is heated, creating favorable SAGD conditions.

Fig. 14 displays the temperature profile at a relative time similar to the Case 1 profile, 120 days after SAGD inception. The temperature distribution is more uniform along the entire wellbore. In this case, a large steam chamber is growing in the middle of the reservoir.

Contrary to the extreme pressure differential and SAGD cases where short-circuiting caused much of the steam to exit the reservoir immediately, the cyclic case is more efficient. All of the injected steam enters the reservoir and heats the near-wellbore area. One consequence of this is the uniform temperature distribution along the entire wellbore. Because of the increased thermal efficiency of the cyclic process, it appears that this procedure is the most appealing method of initiating SAGD. In the scope of our research up to this point, we have not optimized the cyclic process. The problem of optimizing cycle times, operating conditions, and the number of cycles should be studied in more detail.

Discussion

The problem of improving early-time performance of SW-SAGD transforms, essentially, into a problem of heating rapidly the near-wellbore area to create conditions that allow gravity drainage of oil to take place. More specifically, in order for a steam chamber to grow, oil viscosity must be low enough so that fluid drains to the wellbore creating volume that steam can fill and thereby migrate upward in the reservoir. After the conditions necessary for gravity drainage of oil have been initiated by preheating, the SW-SAGD process allows for continuous steam chamber growth and oil production.

After comparing various simulation results, cyclic steam injection appears to be the most efficient method of heating the near-wellbore area. The problem of optimizing the early-time cyclic procedure should be further studied.

An important general observation is that regardless of the process, early-time procedures should be carried out to maximize steam injection and heat delivery to the reservoir. The goal of any early-time procedure should be to heat the near-wellbore area as uniformly as possible. This goal is easier to achieve when operating at a maximum steam temperature. Later in the SAGD process, pressure can be reduced to a target operating pressure which optimizes efficiency and production rate.

As a final observation, there are obvious factors that will improve or inhibit SW-SAGD performance. For example, lower viscosity will certainly improve response, as will higher permeability and system compressibility. Our model, however, represents a base case from which we draw general conclusions. The actual variance in performance due to varying reservoir parameters is an interesting problem that should be studied in more detail. A sensitivity analysis of reservoir properties should be performed.

Conclusions

A primary conclusion reached here is that to improve early-time performance of SW-SAGD, it is necessary to heat the near-wellbore region rapidly and uniformly to create conditions favorable to the SAGD process. Cyclic steaming, as a predecessor to SW-SAGD, represents the most thermally efficient early-time heating method. Uniform heating along the length of the wellbore appears achievable with cyclic steam injection. Regardless of the early-time process, it should be performed to provide maximum heat delivery to the reservoir.

Finally, despite different initial procedures, the oil production rates after several years of steam injection are all very similar.

Further Areas of Study

This paper presents qualitative ideas on how to improve early-time performance of SW-SAGD. An obvious extension of this work is to optimize each procedure using quantitative results such as net heat injection and steam-oil ratio. Beyond early-time performance, there are also interesting issues regarding the SAGD process and steam-chamber development. One issue that we are currently studying is the problem of maximizing steam chamber growth by optimizing the pressure differential and spacing between the injection and production portions of the well.

The following list displays ideas for future areas of study:

1. Optimize early-time performance with quantitative results such as net heat injection and steam-oil ratio.
2. Determine optimum pressure differential and spacing between injection and production points to maximize steam chamber growth.
3. Perform a sensitivity analysis and determine a range of reservoir parameters in which SW-SAGD represents an effective enhanced oil recovery technique. Example parameters include reservoir thickness, relative permeability, absolute permeability, etc.
4. Optimize the late time performance by studying target SAGD pressures that will decrease the volume of steam that must be injected while maintaining oil production rate.

References

1. Butler, R.M., Thermal Recovery of Oil and Bitumen, Englewood Cliffs, N.J.: Prentice Hall, 1991, pp. 285-359.
2. Joshi, S.D., "A Laboratory Study of Thermal Oil Recovery Using Horizontal Wells," paper SPE/DOE 14916 presented at the 1986 SPE/DOE Fifth Symposium on Enhanced Oil Recovery held in Tulsa, OK, April 20-23.
3. Oballa, V., and Buchanan, W.L., "Single Horizontal Well in Thermal Recovery Processes," paper SPE 37115 presented at the 1996 International Conference on Horizontal Well Technology, Calgary, Canada, Nov. 18-20.
4. Falk, K., Nzekwu, B., Karpuk, B, and Pelensky, P., "Concentric CT for single-well steam-assisted gravity drainage," World Oil (July 1996), 85-95.

5. Computer Modeling Group, "STARS Version 98 User's Guide," Calgary, Alberta Canada, 1998.

Table 1 - Model Description

Grid System	
3D Cartesian System	
Hybrid Grid Surrounding Well	
Total Number of Blocks:	5,568
X-Dimension (m):	1,400
Y-Dimension (m):	80
Z-Dimension (m):	19.6
Well Length (m):	800
Reservoir Properties	
Initial Pressure (kPa):	2,654
Initial Temperature (C):	16
Initial So (%):	85
Initial Sw (%):	15
Rock Properties	
Porosity (%):	33
Kh (mD):	3,400
Kv (mD):	680
Relative Permeability	See Figs. 2, 3
Fluid Properties	
Live Oil	
Viscosity	See Fig. 4
Water, Oil, & Gas Components	
Initial Oil Phase Composition: 90% Oil, 10% Gas	

Table 2 - Description of Operating Conditions

Property	Operating Condition			
	SAGD	Extreme Pressure Differential	Cyclic	Circulating
Steam Temp. (C):	295	295	295	295
Steam Pres. (kPa):	8014	8014	8014	8014
Injection Well Max Rate Constraint (m3/D):	200	600	300	300
Injection Well Max Pres. Constraint (kPa):	10,000	10,000	10,000	10,000
Production Well Max Rate Constraint (m3/D):	300	600	300	300
Production Well Minimum Pres. Constraint (kPa):	500	500	500	500

Table 3 - Description of Simulation Cases

Case	Description
1	SAGD Operating Conditions from Start
2	Extreme Pressure Differential Conditions for 100 d, Followed by SAGD Operating Conditions.
3	Circulate 100 d, Followed by SAGD Operating Conditions
4	Circulate 100 d, Followed by Extreme Pressured Differential Conditions for 100 d, Followed by SAGD Operating Conditions.
5	Cycle 1X, Followed by SAGD Operating Conditions
6	Cycle 2X, Followed by SAGD Operating Conditions
7	Cycle 3X, Followed by SAGD Operating Conditions

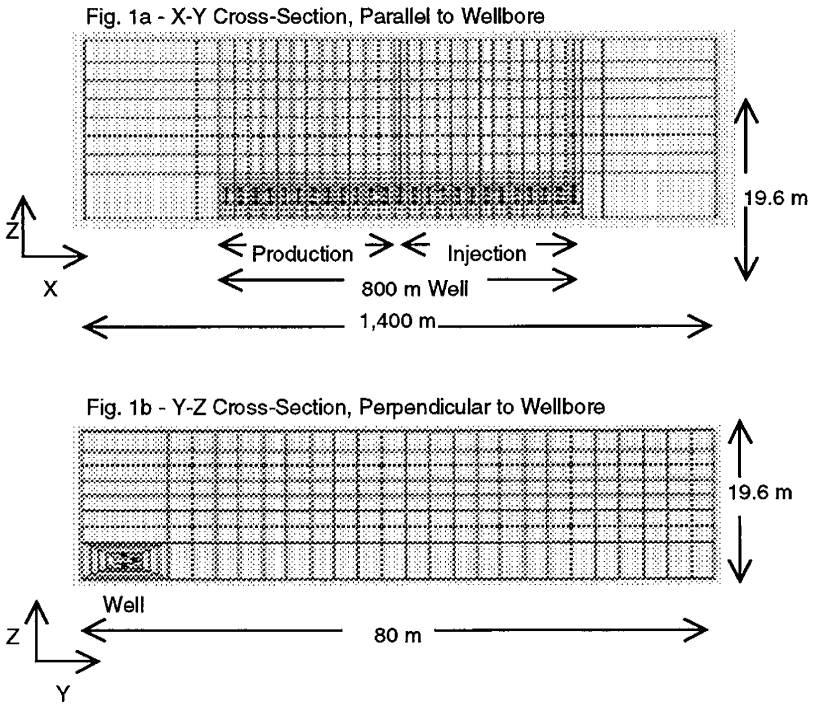

Fig. 1 - Visual Description of the Grid System

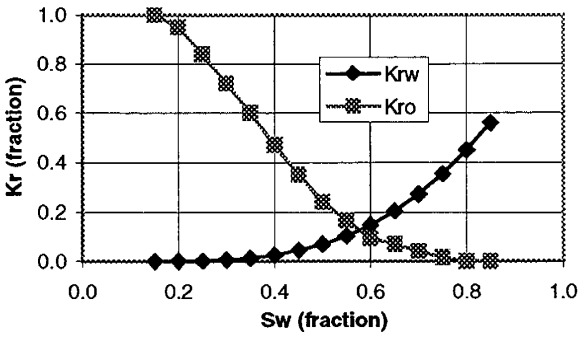

Fig. 2 - Water-Oil Relative Permeability Curve

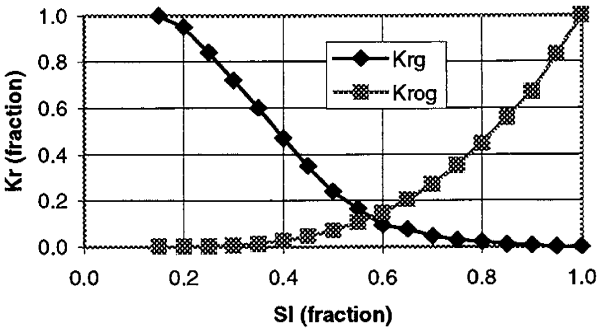

Fig. 3 - Gas-Liquid Relative Permeability

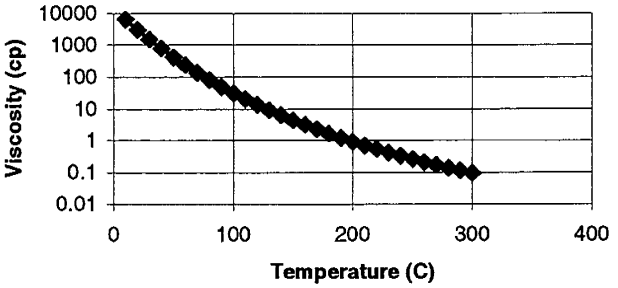

Fig. 4 - Viscosity/Temperature Relationship

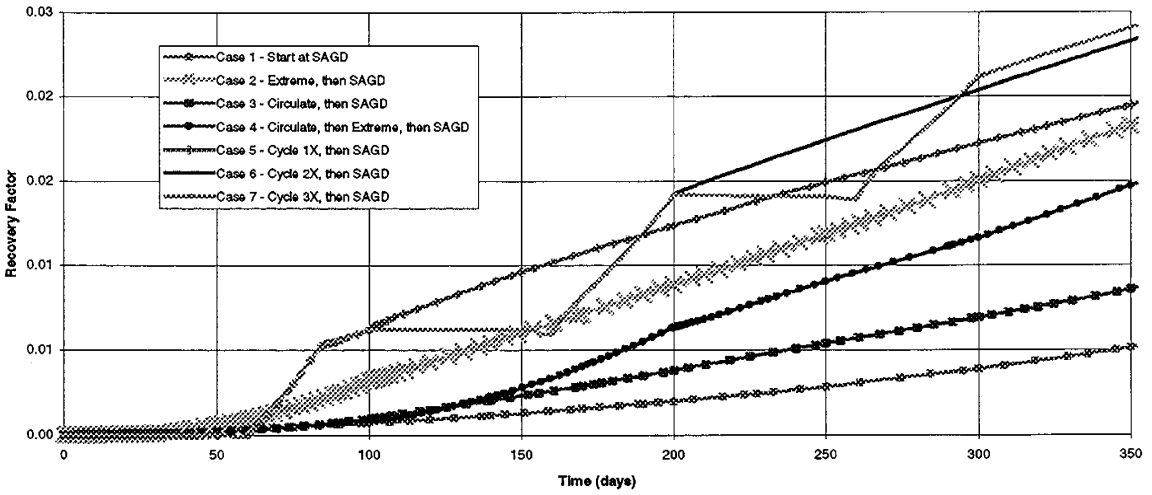

Fig. 5 - Recovery Factor vs. Time for All Cases

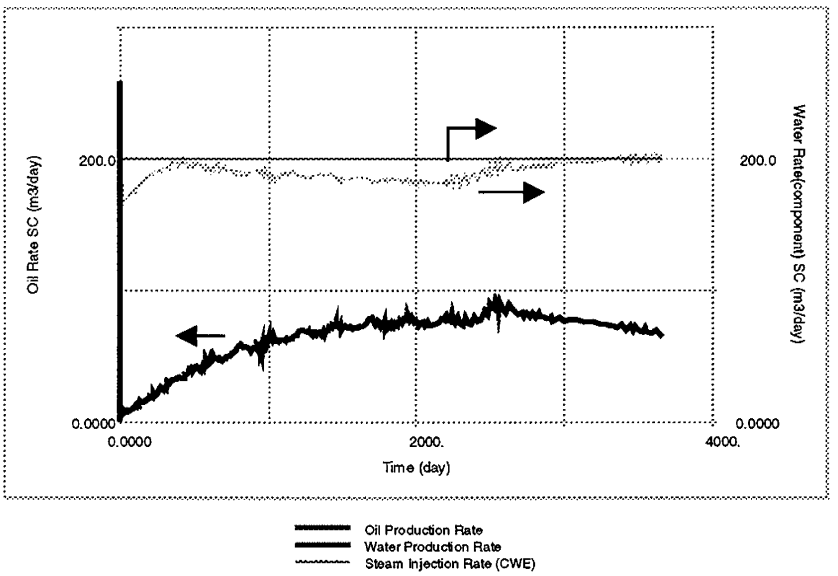

Fig. 6 - Production & Injection Rates vs. Time

Case 1, Continuous SAGD

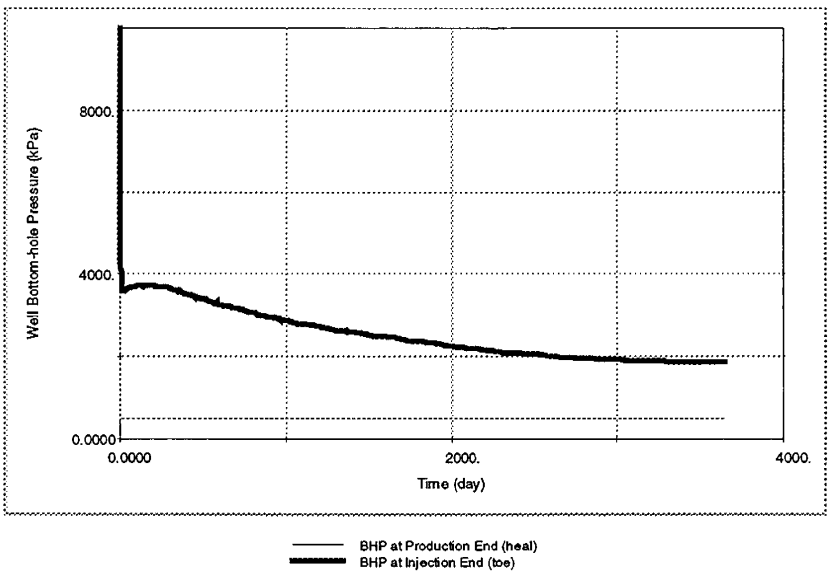

Fig. 7 - Well BHP vs. Time

Case 1, Continuous SAGD

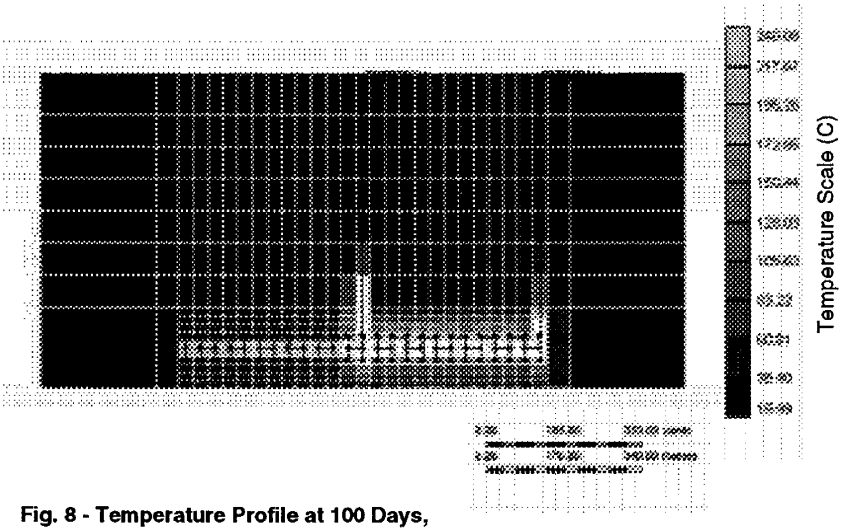

Fig. 8 - Temperature Profile at 100 Days, Case 1 – Continuous SAGD

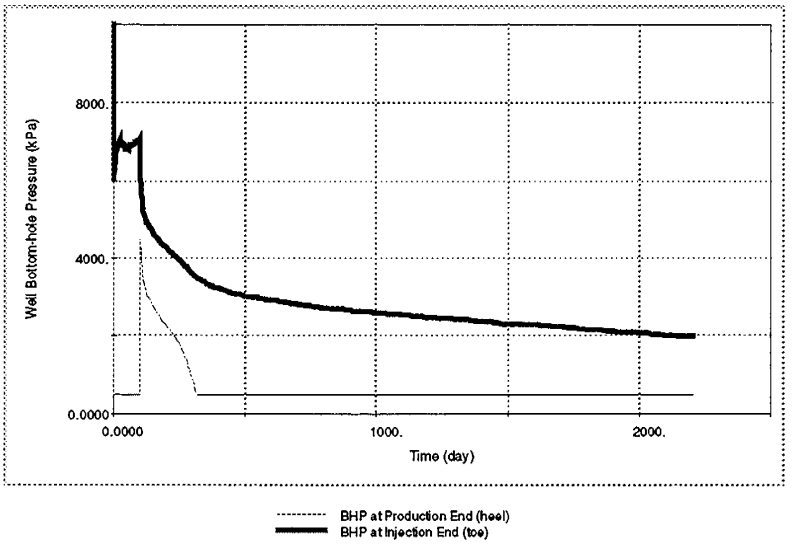

Fig. 9 - Well BHP vs. Time

Case 2, Extreme Pressure Differential, then SAGD

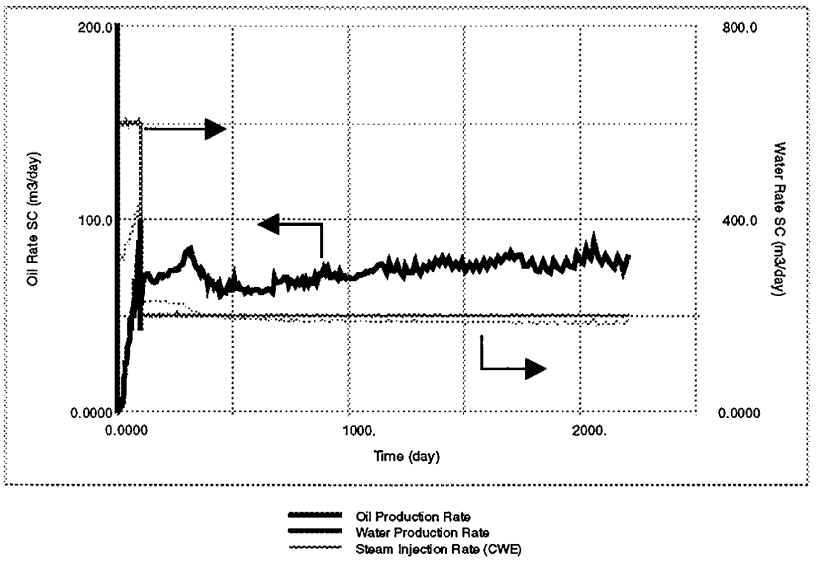

Fig. 10 - Production & Injection Rates vs. Time
Case 2, Extreme Pressure Differential, then SAGD

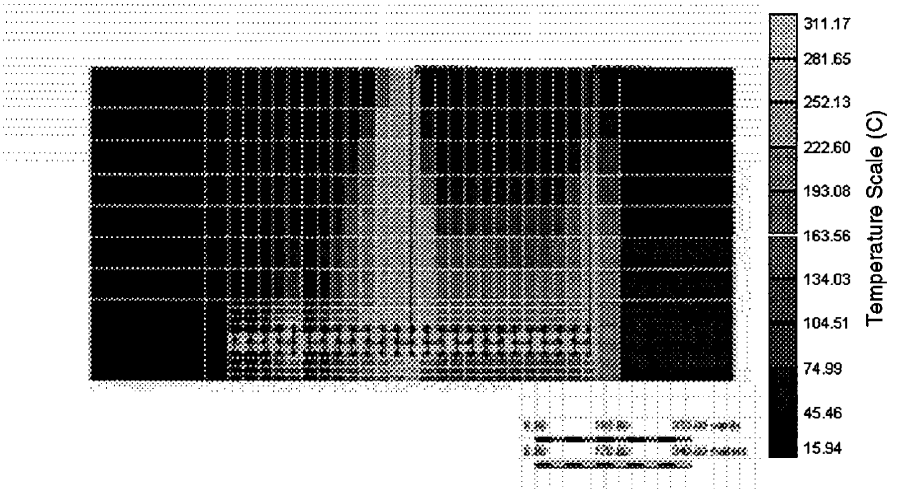

Fig. 11 - Temperature Profile at 200 Days (100 Days after SAGD began),
Case 2 – Extreme Pressure Differential, then SAGD

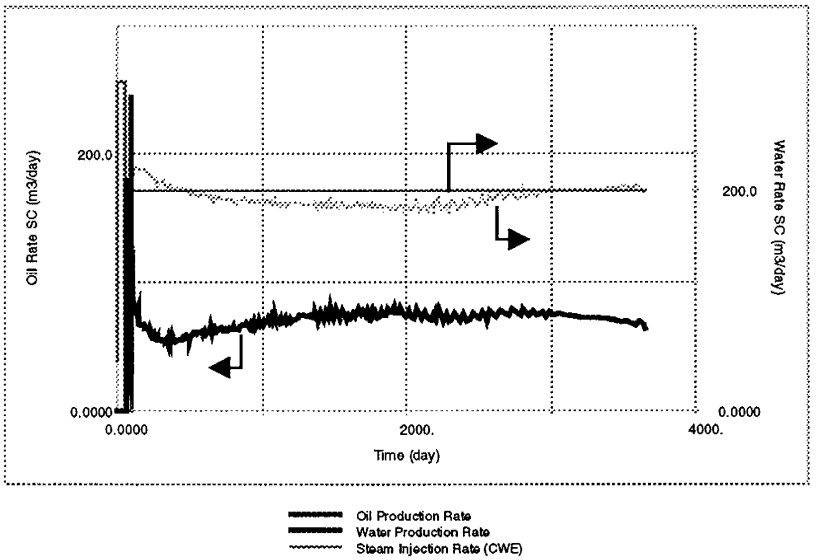

Fig. 12 - Production & Injection Rates vs. Time
Case 5, Cycle 1X, then SAGD

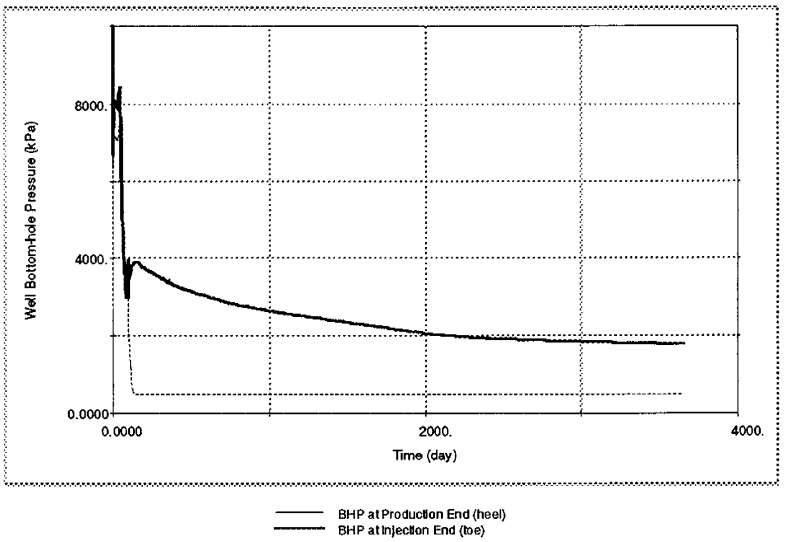

Fig. 13 - Well BHP vs. Time
Case 5, Cycle 1X, then SAGD

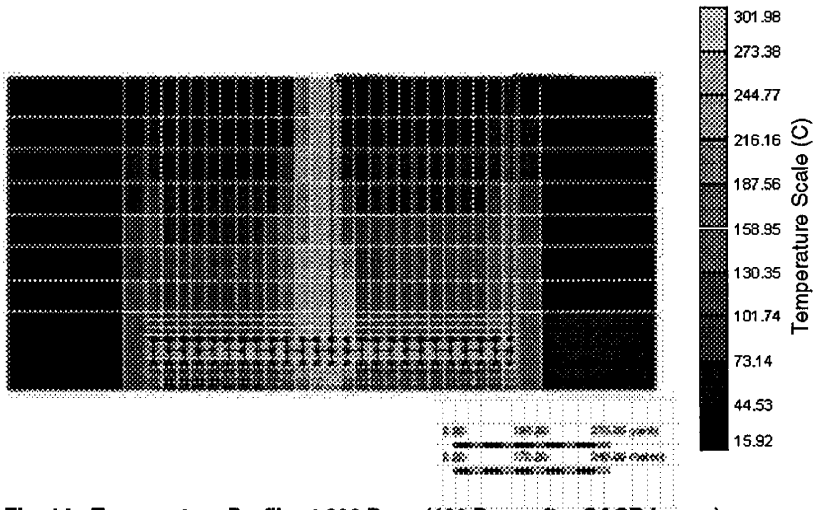

Fig. 14 - Temperature Profile at 300 Days (120 Days after SAGD began), Case 5 – Cycle 1X, then SAGD

3.2 VISUALIZATION OF SOLUTION GAS DRIVE IN MEDIUM TO HEAVY OILS

(David George)

3.2.1 ABSTRACT

Several experimental studies of solution gas drive have been performed, but almost all of the studies have used light oil. Solution gas drive behavior in heavy oil reservoirs is poorly understood. Efforts are being made to view pore-scale solution gas drive phenomena in medium to heavy oils. A pressure vessel has been designed to house silicon-wafer micromodels, which are used for the visual studies. The design of the experimental apparatus and plans for the future of this study are discussed.

3.2.2 INTRODUCTION

3.2.2.1 Solution Gas Drive

Research on solution gas drive is varied and spans roughly fifty years. Presented here is the research that is most relevant to the effort to observe and explain the mechanism of solution gas drive in porous media.

A solution gas drive reservoir is one in which most of the production is due to the expansion of oil and the originally dissolved gas phase. When the oil is undersaturated, the gas phase does not exist. When reservoir pressure is below the bubble point pressure the oil is saturated. Gas bubbles form, or nucleate, at the bubble point pressure and expand with continued decreasing pressure. The critical gas saturation (S_{gc}) is the percentage of pore space which must be occupied by the gas phase before the gas phase is mobilized.

Many solution gas drive laboratory studies have been performed in which gas bubbles do not nucleate in the liquid when the pressure has dropped below the bubble point. A liquid is supersaturated in such a case, in which the amount of gas in solution exceeds the equilibrium value for the particular pressure. The critical supersaturation is

equal to $p_e - p_{crit}$, where p_e is the liquid-vapor equilibrium pressure at the initial liquid composition and temperature and p_{crit} is the liquid pressure at which nucleation first occurs. Few solution gas drive studies have been performed using heavy oils. Most of the literature cited below describes work with light oil.

Kennedy and Olson (1956) used a window cell to observe the formation of bubbles in a mixture of kerosene and methane in the presence of silica and calcite crystals. The time before the first nucleation was short for high degrees of supersaturation, and was lengthened with decreasing supersaturation. For supersaturations of 30 psi or less no nucleation occurred. Thus, for higher pressure decline rates, greater numbers of bubbles formed. The number of bubbles formed was also observed to depend on the gas diffusion rate through the oil. Bubbles formed on the surface of the silica and calcite crystals.

Stewart, *et al.* (1953, 1956) performed pressure depletion tests using limestone cores to recover a $C_1 / C_{10} - C_{12}$ mixture by solution gas drive. They estimated the number of bubbles formed for various decline rates, and determined that greater pressure decline rates result in greater numbers of bubbles.

Wood (1953) repeated the experiment performed by Kennedy and Olson (1956) using oil and rock from the Rangely field and found that for a supersaturation of 27 psi no gas bubbles would nucleate.

Wieland and Kennedy (1957) determined the bubble frequency in cores that underwent pressure decline in a steel bomb. A mixture of East Texas crude oil and methane was used in the experiments. The study showed that greater pressure decline rates result in greater numbers of bubbles, and that low supersaturations (about 25 psi and lower) could be maintained without the occurrence of bubble nucleation. The authors concluded that the properties of different types of reservoir rocks affected the bubble frequency. They hypothesized that this could be due to the differences in grain surface areas of the different reservoir rocks and the surface tensions of the oils used.

Hunt and Berry (1956) applied models for gas-phase growth in bulk liquids in a study of gas-phase growth in porous media. Handy (1958) observed supersaturations of

over 200 psi in methane/kerosene mixtures and mixtures of highly refined white oil and methane during solution gas drive tests using low permeability sandstone cores.

Chatenever, *et al.* (1959) made the first microscopic observations of solution gas drive behavior, using a butane-saturated mineral oil in glass bead packs and thin sections of sandstone and limestone. They observed that capillary forces significantly affected bubble growth, and concluded that the displacement of oil in a solution gas drive is caused by existing microscopic gas structures instead of by the formation of new gas bubbles. They also observed that after a gas bubble was formed, it coalesced with other gas structures, eventually forming a long, narrow, continuous gas bubble.

Dumore (1970) performed solution gas drive experiments in transparent models filled with glass beads, using a C_1/kerosene/novasol mixture. According to the data the maximum supersaturation occurred after the occurrence of nucleation. It was concluded that S_{gc} depends on capillary effects.

Visual studies performed by Wall and Khurana (1971, 1972) indicated that nucleation in porous media begins in a supersaturated liquid. High pressure decline rates were observed to lead to high degrees of supersaturation. Gas bubbles were observed to grow and coalesce after nucleation.

Abgrall and Iffly (1973) measured S_{gc} using reservoir crude oil in vuggy and intergranular rock. They developed a model that predicts the supersaturation that is necessary for the occurrence of nucleation. In the model this critical supersaturation is not dependent on the pressure decline rate. One experiment performed by Madaoui (1975) indicated that (S_{gc}) was nearly unrelated to the pressure decline rate.

Danesh, *et al.* (1987) performed solution gas drive experiments on North Sea separator crude oils recombined with a nine-component gas mixture. A high-pressure etched-glass micromodel was used. The pressure had to be lowered well below the bubble point for nucleation to occur. The first bubbles to nucleate appeared in pore bodies or wide channels. Actual nucleation events, however, could not be observed. After nucleation bubbles grew by diffusion, and were eventually mobilized, moving by jumps and snap-off. Moulu and Longeron (1989) reported that for a C1/C3/C10 mixture the pressure decline rate affected the degree of supersaturation and S_{gc}.

Yortsos and Parlar (1989) conducted a study of gas formation in porous media. They made a distinction between the processes of nucleation and gas-phase growth. The nucleation of gas in porous media was modeled as heterogeneous nucleation, a process in which gas bubbles form from specific nucleation sites that contain trapped gas (pre-exisent or nucleated) on pore walls. Nucleation occurs when the local supersaturation pressure becomes greater than the capillary pressure at the site, causing the liberation of a gas bubble. The authors stated that this process occurs at various nucleation sites, all of which are activated as a function of supersaturation. They found that nucleation is most likely to occur in the largest pores first. For the first time it was stated that nucleation does not depend on the kinetics of homogeneous nucleation or heterogeneous nucleation, but only on the concentration of the volatile species and on the liquid pressure. Furthermore, an analysis of the growth of a single gas bubble after nucleation was performed. A percolation model for gas-phase growth that is valid for low pressure decline rates was developed. The authors determined that for low pressure decline rates, for which capillary forces are dominant, S_{gc} is a function of the nucleation characteristics of the porous medium, which are dependant on pore geometry. For cases in which capillary effects are not dominant, it was suggested that the growth of the gas phase could be modeled by diffusion-limited aggregation (DLA). For DLA-type gas-phase growth, no equilibrium states exist except complete saturation of the porous medium by gas, with the exception of the existence of trapped liquid.

Firoozabadi, *et al.* (1992) performed solution gas drive experiments using a $C_1/n-C_{10}$ mixture in Berea sandstone and chalk cores. In some of the experiments a light mixture of about 35%, C_{10} was used. In other experiments a heavier composition of about 70% C_{10} was used. A pump with a fixed expansion rate was used to avoid sudden pressure changes. The authors concluded that, even at high expansion rates, supersaturation in porous media could be negligible. They also found that pore structure could affect the degree of supersaturation such that rock with smaller grains could display less supersaturation than a rock with larger grains. They stated that the S_{gc} is a function of both supersaturation and pore structure.

Kortekaas and van Poelgeest (1991) measured S_{gc} for light, two-component hydrocarbon mixtures in clean, water-wet cores with the presence of connate water. They concluded that increasing pressure decline rates lead to an increase in S_{gc} and that pore structure is important during nucleation.

Li and Yortsos (1991) visualized gas formation by pressure decline in a carbonated water system using a Hele-Shaw cell and a glass micromodel. In the Hele-Shaw cell nucleation occurred at different sites, forming nearly radial bubbles that exhibited compact growth at early stages. As the bubbles grew they would frequently coalesce, eventually leading to the formation of a large, dominant bubble. Nucleation was observed to occur at various sites in the micromodel, but growth occurred in a ramified fashion. S_{gc} was found to decrease with increasing pressure decline rates, an observation that conflicted with several results reported in the literature (Firoozabadi, *et al.*, 1992; Kortekaas and van Poelgeest, 1991; Firoozabadi and Kashchiev, 1996). A numerical pore network model was developed to simulate nucleation and growth of the gas phase in porous media. The model accounted for nucleation, gas expansion, mass transfer growth, concentration gradients, and finite size effects. The numerical results were found to approximate the experimental results.

Li and Yortsos (1993) further developed the theoretical analysis and pore network simulation of bubble growth in porous media, this time considering the growth of both single and multiple gas clusters.

Li and Yortsos (1994) studied the stability of a single bubble growing in an effective porous medium with constant supersaturation. A new stabilization mechanism was identified based on convective transport in the growing phase. This stabilization mechanism was found to be stronger for higher mobility ratios. Experiments using Hele-Shaw cells were performed to support the findings of the study.

Li and Yortsos (1995a) observed the growth of the gas phase in a carbonated water system in etched-glass micromodels and Hele-Shaw cells. They found that the growth of the gas phase in micromodels led to ramified patterns in gas clusters, while the growth of the gas phase in Hele-Shaw cells was much more compact. A pore network simulator was developed which predicted growth patterns of the gas phase in porous

media. The simulator showed reasonable agreement with the experimental results. Satik, *et al.* (1995) described scaling behavior for single bubble growth in porous media in three dimensions. The authors determined that for conditions of low supersaturation, the rate of growth scales to $t^{1/(D_f-1)}$, where D_f, a value less than 3, is the pattern fractal dimension, instead of the classical scaling to $t^{1/2}$. The scaling behavior described by the authors predicts a slower bubble growth rate than classical scaling behavior.

Li and Yortsos (1995b) performed a systematic theoretical analysis of bubble growth in porous media, with a strong emphasis on modeling S_{gc}. Three different regimes of gas-phase growth behavior were identified for the growth of multiple gas clusters. For cases in which the pressure decline rate is sufficiently low, such that growth is completely controlled by capillarity, global percolation was identified as the growth mechanism. During growth by global percolation the largest throat fills with gas, without regard to the size or location of the gas cluster of which it becomes a part. For higher pressure decline rates a combination of percolation rules governing the advance of each gas cluster and DLA rules governing the mass transfer was used to model the growth of the gas phase. This growth regime is called "percolation-DLA." A third regime, "percolation-modified-DLA," was also identified. S_{gc} was found to be completely dependent on the nucleation fraction when growth is controlled by global percolation. Furthermore, S_{gc} was also found to be independent of the pressure decline rate in cases for which the pressure decline rate was high. The authors theorized that a larger nucleation fraction, caused by a higher pressure decline rate, is what causes an increase in S_{gc}. The authors stated that solution gas drive depends on the underlying growth pattern.

Firoozabadi and Kashchiev (1996) developed a simple model to describe gas-phase growth in porous media that challenged the classical theory of heterogeneous nucleation. They claimed that their experimentation, along with experimental results found in the literature, support an instantaneous nucleation model instead of a heterogeneous nucleation model. The instantaneous nucleation model was derived from theories related to the growth of the gas phase in bulk liquids. According to the authors,

nucleation at all sites occurs instantaneously, and supersaturation is affected by the pressure decline rate.

Yortsos (1997) defended the heterogeneous nucleation model, arguing that the results of his work are consistent with experimental results and that instantaneous nucleation was not observed in his experimental work. He argued that Firoozabadi and Kashchiev (1996) modeled the critical gas saturation using theory that was developed for the growth of a single isolated bubble in a bulk fluid, as opposed to multiple bubbles in a porous medium.

Firoozabadi (1997) in turn questioned the experimental methods of Li and Yortsos, and he reiterated his opinion that critical supersaturation is not the supersaturation pressure needed to activate an individual nucleation site on a pore wall by overcoming capillary pressure. He also disagreed with the model of S_{gc} proposed by Li and Yortsos, asserting that it is based on constant bubble density and is independent of rate.

El-Yousfi, *et al.* (1997) studied the liberation of CO_2 from supersaturated carbonated water in resin and glass micromodels. They concluded that neither heterogeneous nucleation nor instantaneous nucleation could explain their results. To explain the results a new model of capillary trapping was developed, by which drawdown balances capillary trapping, resulting in the activation of a nucleation site. The authors determined that instantaneous nucleation was not a satisfactory explanation of what happens at the pore scale during nucleation, but that it provides a suitable approximation of the experimental results. Unfortunately, bubbles could not be observed until they grew to a size of 30 μm, well after the corresponding nucleation sites were activated. The authors also noted the tendency for the gas phase to develop ramified (branching) patterns.

Bora, *et al.* (1997) conducted a high-pressure micromodel study of solution gas drive behavior in heavy oil reservoirs. Five different natural and synthetic oils were used, one of which was Lindbergh heavy crude oil. They observed that the presence of asphaltenes tended to hinder bubble coalescence, and noted that wettability did not appear to be a critical parameter for solution gas drive processes.

3.2.2.2 Micromodels

Micromodels are produced with the objective of directly observing fluid flow through porous media. Micromodels contain an etched flow pattern that can be viewed with a microscope. The flow pattern can be a lattice of straight or constricted channels, or the pore network can be modeled after the pores found in naturally occurring rock. Fluid enters a micromodel, flows through the porous medium, and exits the micromodel. A limitation that is inherent to all micromodels is the fact that they are only two-dimensional. Numerous studies have been performed using etched-glass micromodels. Attempts were made to replicate naturally occurring pore patterns with etched-glass micromodels, but the necessary etching processes resulted in large pore sizes and the necessary annealing processes resulted in a loss of surface roughness.

Mattax and Kyte (1961) developed the first etched-glass micromodel. The model consisted of a network of straight, interconnected flow channels. The channels were etched with hydrofluoric acid. The micromodel provided a superior means for viewing interfaces in porous media. The micromodel was used to study the effect of wettability on waterfloods.

Davis and Jones (1968) applied an etching technique that resulted in the construction of superior micromodels. A photosensitive resist that becomes resistant to many solvents after exposure to ultraviolet light was coated on a glass surface. Any black and white pattern could be projected onto the photosensitive resist, rendering part of the glass impervious to etching. This provided the ability to etch complex patterns in glass, resulting in micromodels with complex pore structures.

The etched-silicon-wafer micromodels developed by Owete and Brigham (1987) allow for increased control of etch depth. A flow pattern is etched on a silicon wafer, which is then oxidized to reproduce a water-wet porous medium. The flow area is sealed with a glass plate that is anodically bonded to the silicon wafer.

The micromodels developed by Hornbrook, *et al.* (1991) are superior to etched-glass micromodels. An almost exact replica of a thin section of Berea sandstone is reproduced on a silicon wafer. These micromodels possess roughness and wettability characteristics that are approximately equal to those of the original sandstone.

Furthermore, when the micromodels are produced the depth of the pore and channel network can be controlled with great accuracy.

Since 1985, several micromodel studies have been performed at elevated pressures. The studies focus on a variety of phenomena that are affected by pressure, and various types of pressure vessels have been designed to allow the observation of micromodels at high pressure.

Campbell and Orr (1985) performed a high pressure visualization study of the displacement of crude oil by CO_2. An etched-glass micromodel was placed in a pressure vessel, and experimentation was performed at pressures of up to 1200 psia.

Peden and Husain (1985) built a pressure vessel that housed etched-glass micromodels and provided a confining pressure of 6000 psi. They used the vessel to visualize multiphase flow through porous media and CO_2 flooding. Danesh, *et al.* (1987) used the vessel described by Peden and Husain (1985) to observe solution gas drive processes at the pore scale.

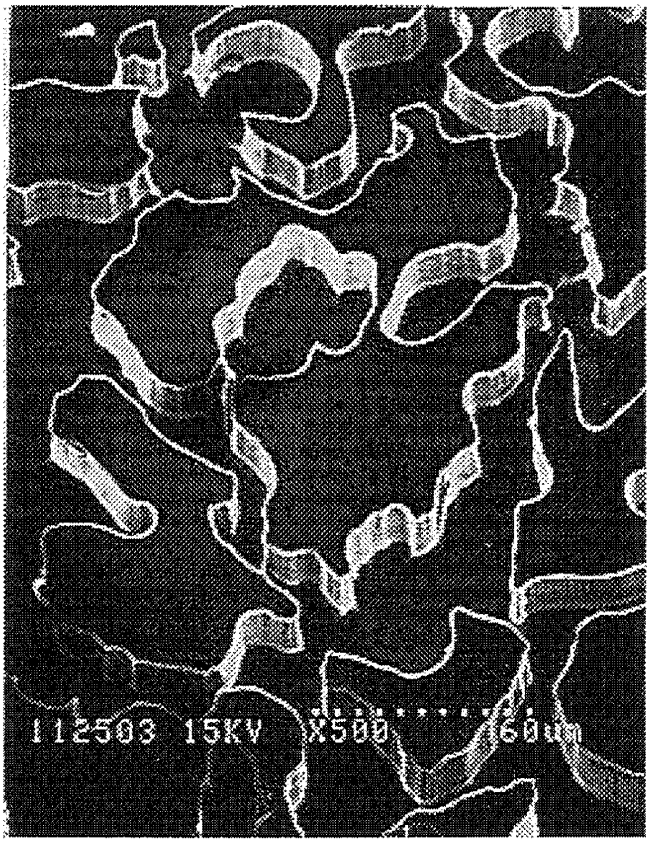

Figure 1. SEM of silicon-wafer micromodel. Features of grain roughness are reproduced with accuracy on the order of 1 μm.

Kuhlman (1990) designed a high-pressure cell that housed etched-glass micromodels in order to observe interactions between foam and oil.

Coşkuner (1997) used a pressure vessel similar to that of Kuhlman (1990) that housed etched-glass micromodels. High pressure experiments were performed to study gas condensate flow in porous media.

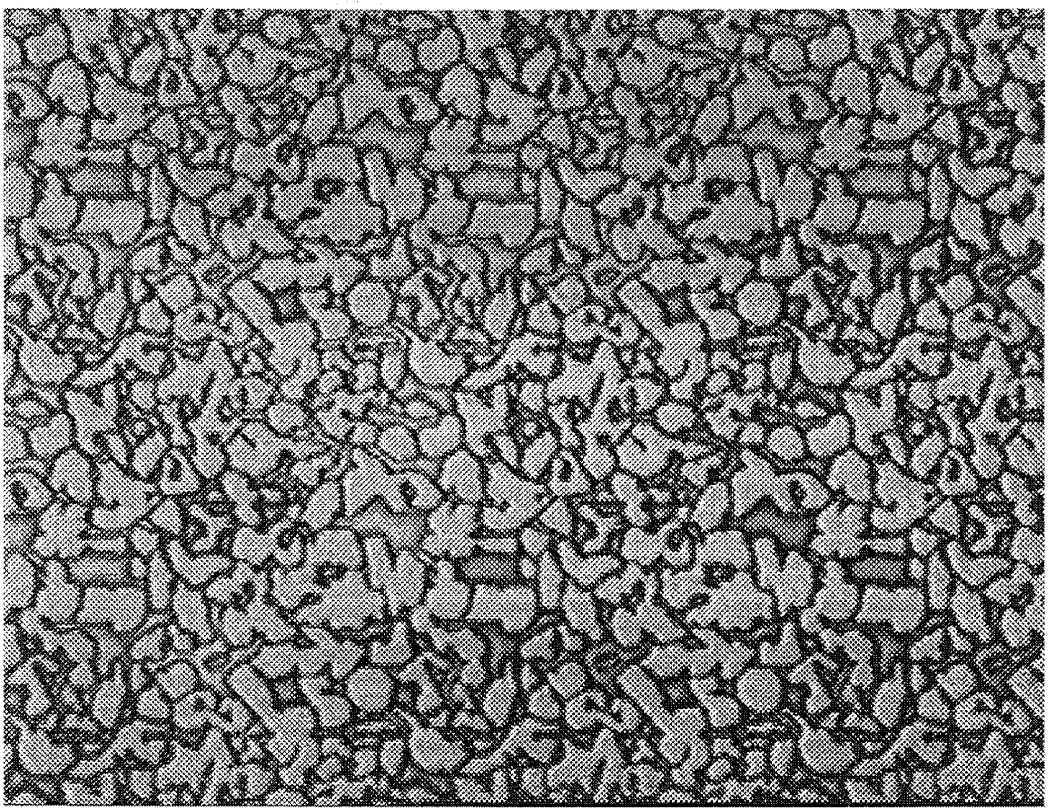

Figure 2 . Photograph of the repeated etch pattern on the silicon wafer.

Bora, *et al.* (1997) used a high-pressure micromodel to observe solution gas drive processes in heavy oil. An etched-glass plate was held against a smooth glass plate by overburden pressure inside a windowed pressure vessel.

3.2.2.3 Objectives

It is important to note that with the exception of some work performed by Firoozabadi, *et al.* (1992) and Bora, *et al.* (1997), solution gas drive experiments have been performed using light oils. Furthermore, only Bora, *et al.* (1997) has performed a micromodel visualization study using heavy oil. There is clearly a need for solution gas drive experimentation using more viscous oils. Silicon-wafer micromodels of the type described by Hornbrook, *et al.* (1991) (Figs. 1 and 2) are used in this study. The goal of this work is to observe solution gas drive phenomena at the pore scale in oils of medium and heavy viscosity using silicon-wafer micromodels.

3.2.3 EXPERIMENTAL APPARATUS

3.2.3.1 Pressure Vessel

The bond that holds an etched-silicon wafer to a glass cover plate may fail when the difference between internal and external pressure is greater than about 30 psi. In order to achieve the goal of performing solution gas drive experiments in silicon-wafer micromodels, a pressure vessel in which a micromodel can be housed has been designed and constructed. The pressure vessel has a maximum operating pressure of 1000 psig. The temperature of the vessel can be controlled, ranging from $15^{o}C$ to $100^{o}C$. Because the surface of the silicon-wafer micromodel is oxidized, the use of silicon-wafer micromodels at higher temperatures demands some reconsideration. Silicon dioxide (SiO_2) is appreciably soluble in water at elevated temperatures.

The pressure vessel is made of 6061 T6 aluminum. The micromodel sits inside of the body of the pressure vessel. Holes that serve as fluid inlet/outlet ports are drilled in the bottom of the micromodel. These holes rest directly above machined channels that carry fluid to and from the micromodel. O-rings are used to create a seal where the tubes meet the inlet/outlet ports of the micromodel (Figure 3). Confining liquid is used to provide pressure support to the micromodel. If temperature control is not needed, the confining liquid can remain static. The vessel is designed, however, to allow the confining liquid to circulate through the interior of the pressure vessel, entering and exiting through tubes that are located on opposite sides of the vessel. If a circulating confining liquid is used it can be pumped through a temperature control bath before entering the pressure vessel, allowing the temperature to be controlled. A 0.185 in thick sapphire window is located directly above the micromodel. Sapphire was selected because of its superior mechanical and optical qualities. The window is held between the micromodel and the pressure vessel lid in a manner such that its edges are considered to be fixed (Figure 4). This leads to maximum mechanical strength. An O-ring between the lid and the window seals the space. The pressure vessel lid is shaped like an annular ring. The lid fits over both the body of the pressure vessel and the window, such that the window, and thus the micromodel, is viewed in the center of the annular ring.

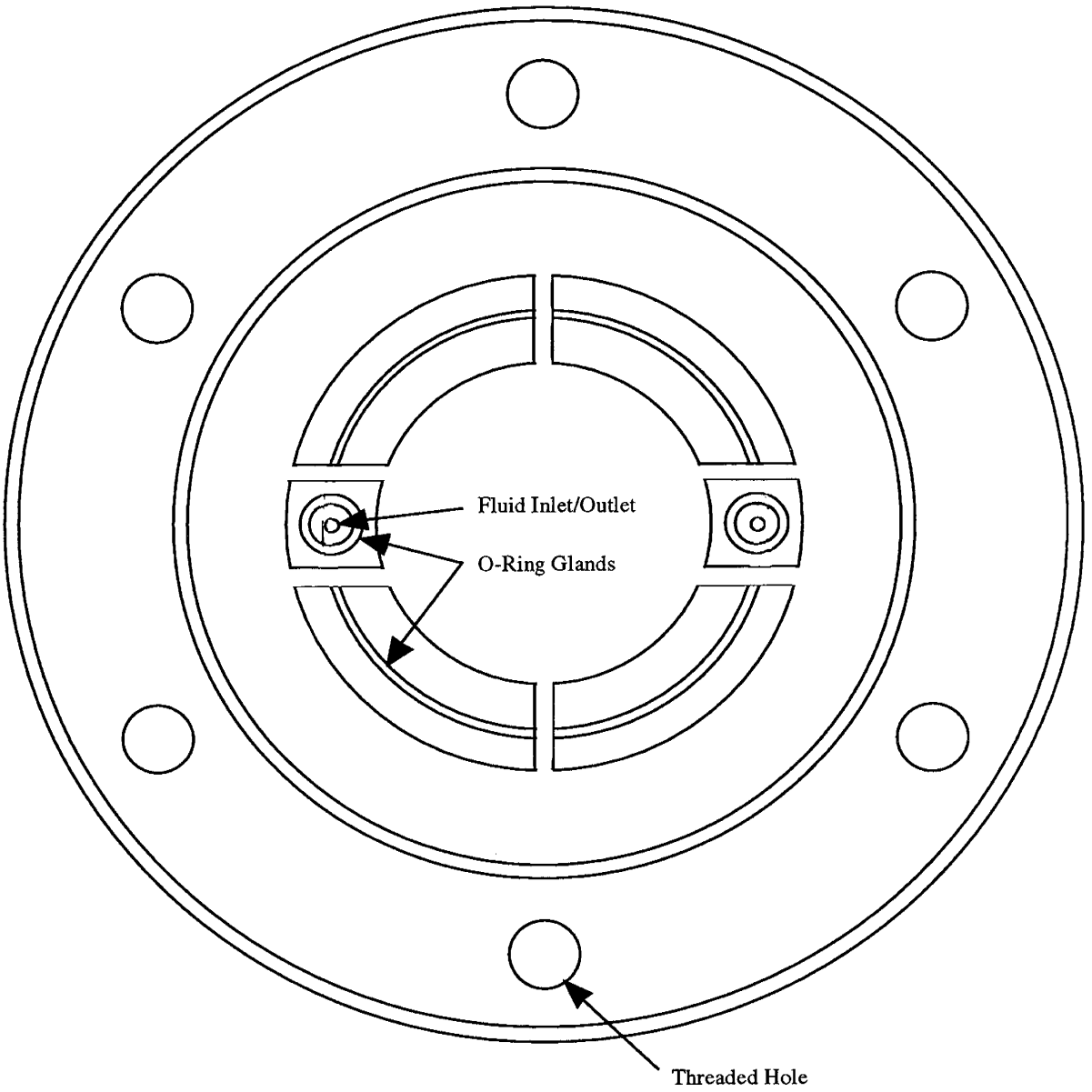

Figure 3. Top view of the interior of the pressure vessel.

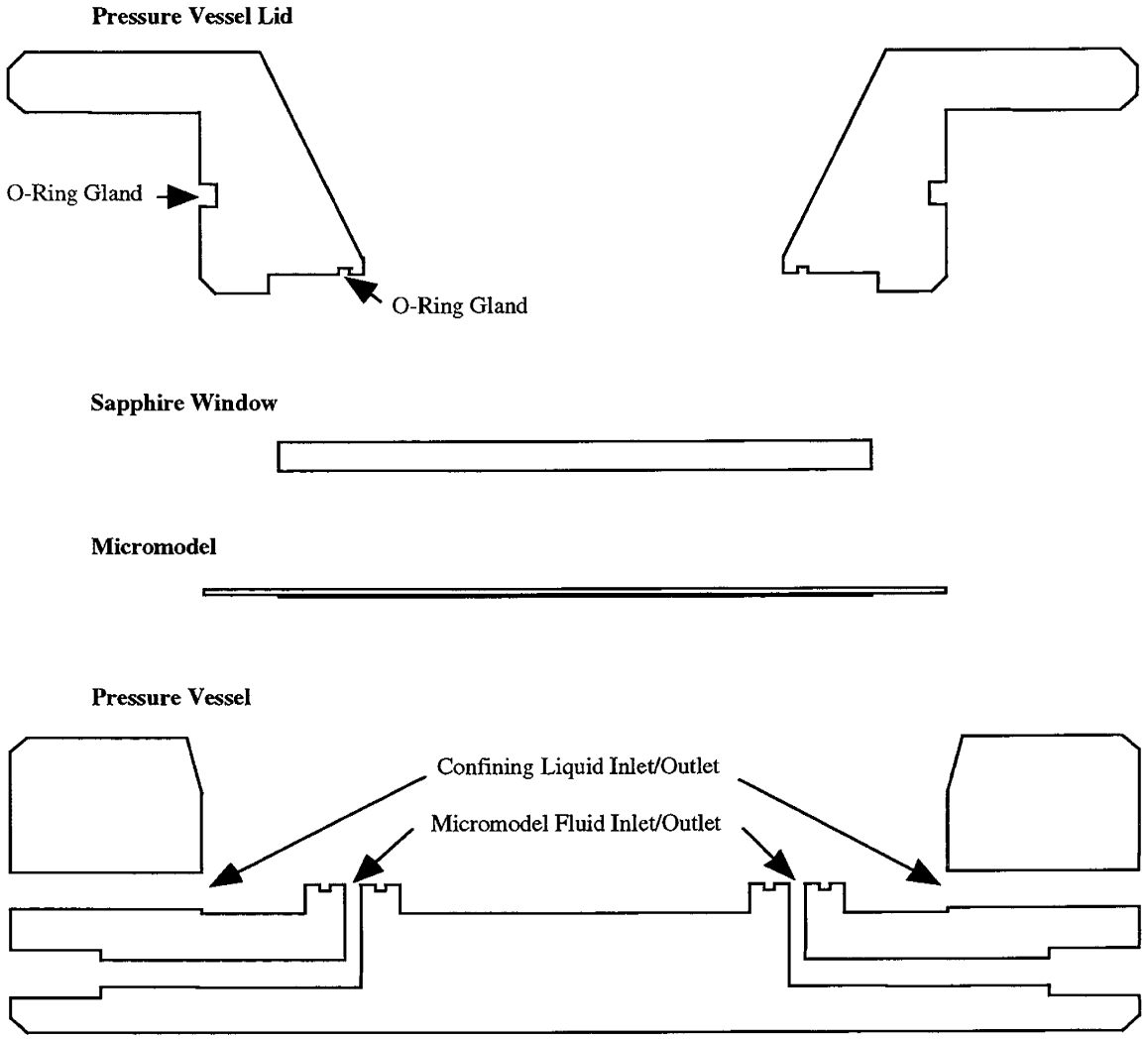

Figure 4. Exploded cross-sectional view of the pressure vessel.

In order to prevent failure of the pressure vessel and to protect users, some safety features are implemented. A confining liquid is used because liquid will not expand nearly as much as gas in the event of failure. A modified hydraulic cylinder is used to pressurize the confining liquid without allowing the liquid to contact the pressurizing gas. This prevents the liquid from saturating with gas. In order to assure that no gas enters the confining liquid chamber, the pressure vessel is assembled under water. The pressure system was designed for 1500 psi, even though the maximum operating pressure of the system is nominally 1000 psi, thus a factor of safety of 1.5 was established. The pressure

vessel successfully withstood a pressure test, containing water that was pressurized to 940 psi for one hour. No leaks or structural failure occurred.

3.2.3.2 Pressure System

Compressed CO_2 is used to pressurize water, which was selected to be the confining liquid. The confining water is pressurized in a modified hydraulic cylinder. A piston in the hydraulic cylinder separates the pressurized gas from the confining water (Figure 5). Because the gas is not in contact with the liquid, the liquid cannot become saturated with the gas. If the liquid were saturated with gas and failure occurred, pressure would drop immediately and gas would instantly come out of solution. This gas would expand rapidly, and potentially causing an explosion. If the confining liquid is not in contact with the gas, then no gas will form in the confining liquid in the event of failure. The piston is free to move across the length of the hydraulic cylinder. When pressure is applied to the piston by the gas, the piston applies pressure to the confining liquid. A pressure gauge indicates the pressure of the confining liquid.

The system that is used to control flow through the micromodel is separate from the system that pressurizes the confining liquid. A CO_2 cylinder provides both forward-pressure and back-pressure for the micromodel. The fluid that is pumped into the micromodel is pressurized by CO_2 in a bomb. This fluid can be given time to saturate with CO_2 before flowing into the micromodel. A three-way valve controls whether oil or CO_2 is pumped through the micromodel. A plug valve can isolate the micromodel from upstream fluids. On the downstream side of the micromodel, a three-way valve is used to select whether the pressure downstream from the micromodel will be atmospheric, allowing flow through the micromodel, or whether back-pressure will be applied. The back-pressure is controlled by the pressure regulator on the CO_2 cylinder. Pressure gauges indicate the pressures upstream and downstream from the micromodel.

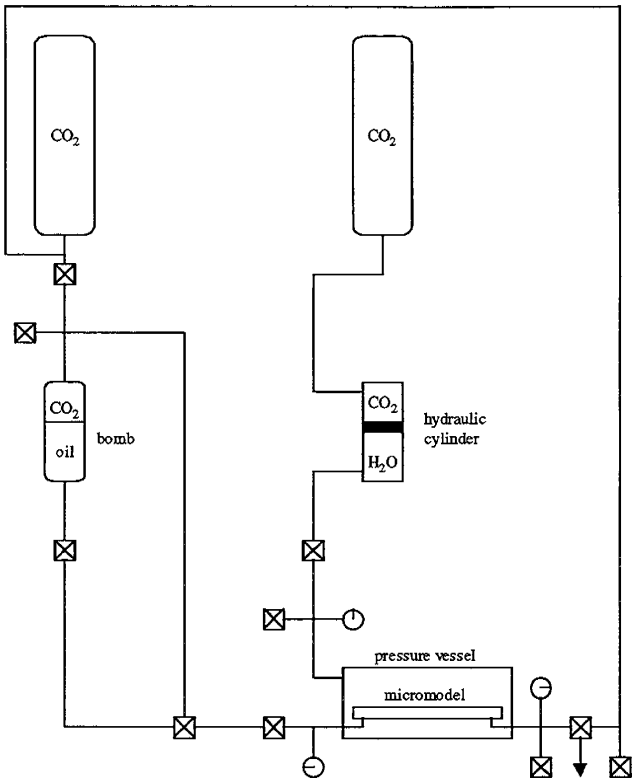

Figure 5. Pressure System.

3.2.3.3 Optics

A Nikon Optiphot-M microscope with a photo tube that allows for the connection of a video camera was used. Because the silicon-wafer micromodels are opaque, a light source inside of the microscope sends light through the objective lens in order to illuminate the micromodel. Light is reflected off the micromodel, providing an image of the micromodel. The image enters the objective lens, and is sent to the ocular lenses and to the photo tube. The ocular lenses of the microscope provide 10X magnification. A video camera is connected to the photo tube. Images are sent from the video camera to a VCR for recording. An

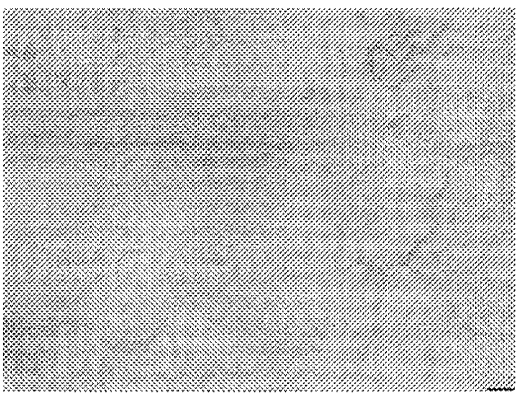

Figure 6. This image of a micromodel in the pressure vessel exhibits noticeable "ghost" images (200X magnification).

extra-long working distance objective lens, a Nikon 0.4ELWD with a 4 mm working distance, was used for this study. The thickness of the sapphire window (4.7 mm), combined with the thickness of the micromodel's cover glass (1 mm), results in a cover glass thickness of 5.7 mm. This thickness is greater than the working distance of the objective lens. A loss of image quality, which mainly consists of a loss in contrast, occurs as a result.

The superior mechanical strength and optical qualities of sapphire provide the advantages of a short working distance and high transmission of light. The fact that sapphire has anisotropic optical properties, however, causes double refraction images that reduce image quality. The image of the micromodel that is transmitted by the objective lens contains "ghost images" that are due to double refraction (Figure 6). The double refraction images are much lighter than the real images. Although there is a reduction in image quality, the image remains interpretable.

3.2.4 EXPERIMENTATION AND RESULTS

3.2.4.1 Foam Flow

An experiment was carried out in order to determine whether the observation of pore-scale flow events could be observed clearly using the experimental apparatus designed for this study. A 0.1 wt. % AOS 14-16 (alpha olefin sulfonate with a chain length of 14-16 carbons) solution was prepared and used as the surfactant solution for this experiment. A slug of surfactant solution was injected into a dry micromodel, and N_2 was then injected into the slug. This experiment was performed at injection pressures lower than 30 psig, so the use of confining liquid was not necessary. The formation of foam was observed, and microscopic events such as snap-off could be clearly observed.

3.2.4.2 Bubble Nucleation in a N_2/Water System

A second experiment was performed in which water was saturated with N_2 at about 900 psig. This liquid was allowed to enter the micromodel, after which the pressure

was allowed to drop to 0 psig. No attempt was made to record the point at which bubble formation began, but bubble nucleation and formation was successfully observed.

3.2.4.3 Solution Gas Drive

An attempt was made to observe solution gas drive processes in Kaydol, a 29°API gravity mineral oil. The experimental procedure was as follows:

1. Kaydol was saturated with CO_2 at 520 psig in a bomb for six hours. During this time, the micromodel was swept with CO_2 in order to displace air.
2. The flow of CO_2 through the micromodel was stopped, and the micromodel was allowed to saturate with the live Kaydol.
3. The upstream pressure was increased to 600 psig, and a back-pressure of 580 psig was applied.
4. The micromodel was shut in on both sides.
5. The back-pressure was decreased, and the pressures upstream and downstream from the micromodel were recorded at various times. The difference between upstream and downstream pressures, Δp, was calculated for each measurement.

There were two critical differences between the set-up used in this experiment and the set-up described earlier in this report. First, the back pressure was not constant with time because a valve was used to isolate the micromodel from the gas cylinder that provided the back-pressure. This led to increases in the back-pressure after the micromodel was shut in, until pressure equilibrium was reached ($\Delta p = 0$) and flow through the micromodel stopped. This variable downstream pressure is a poorly posed boundary condition. When equilibrium was reached, the back-pressure was decreased by releasing CO_2 from a needle valve. This occasionally resulted in large, sudden decreases in downstream pressure. The second major difference between this experiment and future experiments was that the confining water was pressurized by CO_2 in a bomb, instead of in the modified hydraulic cylinder. This allowed the confining water, in which CO_2 was highly soluble, to become saturated with CO_2 at high pressures.

Throughout the experiment the pressure in the micromodel gradually decreased. The value of Δp increased at early time because of a slow leak in the pressure system. The leak was repaired, and then Δp decreased as expected. On two occasions, pressure equilibrium was reached before gas phase formation was observed. On these occasions, the back-pressure was lowered, resulting in sudden increases of Δp. The experiment was halted by a failure of the pressure vessel window before bubble nucleation was observed. It is certain, though, that a significant degree of supersaturation was reached before the experiment was stopped. At the time of the explosion, the average pressure in the micromodel was 420 psig. The Kaydol was saturated with CO_2 at 520 psig, so a supersaturation of 100 psi was observed shortly before vessel failure.

An explosion occurred after the failure of the sapphire window because the confining water was heavily saturated with CO_2. Pressure in the vessel immediately dropped, leading to rapid liberation and expansion of gas that was previously in solution with the confining water. The sapphire window was irreparably destroyed, the micromodel that was housed in the pressure vessel failed due to the loss of confining pressure, and the objective lens sustained minor damage during the explosion.

At the time of the explosion, the confining water pressure was 600 psig. The sapphire window had previously withstood significantly higher pressures. Furthermore, the sapphire window was designed to withstand 1500 psig. It was concluded that the mechanical strength of the sapphire window was sufficient. An inspection of the pressure vessel lid revealed some burrs that could have point-loaded the sapphire window and caused damage. It is most likely that a microscopic crack formed in the sapphire window, and because sapphire is a crystalline solid, that crack could have propagated while under stress. At some point such a crack probably compromised the structural integrity of the sapphire window, resulting in failure.

3.2.5 PLANS

Another attempt will be made to observe solution gas drive in Kaydol, but in the future the experimental apparatus described in detail in this report will be used. A constant back-pressure will be applied during experimentation, leading to an improved

boundary condition. The pressure system is safer because of the addition of the modified hydraulic cylinder. The solution gas drive experiment in Kaydol will be repeated using a fixed expansion rate pump to avoid sudden pressure drops. Experiments may also be performed using heavy crude oil.

New laboratory equipment has been purchased. A high-resolution color video camera will be used in the future. A new Macintosh computer with audiovisual capabilities has been purchased and will be used to perform video editing and image analysis.

3.2.6 CONCLUSIONS

An experimental apparatus has been developed that allows for the observation of pore scale flow phenomena in micromodels at variable pressures and temperatures. An attempt was made to observe solution gas drive in Kaydol, in which a supersaturation of 100 psi was noted. Experimentation will resume with the objective of observing solution gas drive in Kaydol and in heavy oil.

3.2.7 REFERENCES

1. Abgrall, E. and Iffly, R.: "Etude Physique des Ecoulements par Expansion des Gaz Dissous," *Revue de L'Institut Français du Pétrole* (September-October 1973) 667-692.
2. Bora, R., Maini, B.B. and Chakma, A.: "Flow Visualization Studies of Solution Gas Drive Process in Heavy Oil Reservoirs Using a Glass Micromodel," Paper SPE 37519 presented at the 1997 SPE International Thermal Operations and Heavy Oil Symposium, Bakersfield, CA (10-12 February 1997).
3. Campbell, B.T. and Orr Jr., F.M.: "Flow Visualization for CO_2/Crude-Oil Displacements," *SPEJ* (October 1985) 665-678.
4. Chatenever, A., Indra, M.K. and Kyte, J.R.: "Microscopic Observations of Solution Gas Drive Behavior," *JPT* (June 1959) 13-15.
5. Coşkuner, G.: "Microvisual Study of Multiphase Gas Condensate Flow in Porous Media," *Transport in Porous Media* **28** (1997) 1-18.

6. Danesh, A., Peden, J.M., Krinis, D. and Henderson, G.D.: "Pore Level Visual Investigation of Oil Recovery by Solution Gas Drive and Gas Injection," Paper SPE 16956 presented at the 62nd Annual Technical Conference and Exhibition of the SPE, Dallas, TX (27-30 September 1987).
7. Davis Jr., J.A. and Jones, S.C.: "Displacement Mechanisms of Micellar Solutions," *JPT* (December 1968) 1415-1428.
8. Dumore, J.M.: "Development of Gas Saturations During Solution-Gas Drive in an Oil Layer Below a Gas Cap," *SPEJ* (September 1970) 211-218.
9. El-Yousfi, A., Zarcone, C., Bories, S. and Lenormand, R.: "Physical Mechanisms for Bubble Growth during Solution Gas Drive," Paper SPE 38921 presented at the 72nd Annual Technical Conference and Exhibition of the SPE, Dallas, TX (5-8 October 1997).
10. Firoozabadi, A., Ottesen, B. and Mikkelsen, M.: "Measurements of Supersaturation and Critical Gas Saturation," *SPE Formation Evaluation* (December 1992) 337-344.
11. Firoozabadi, A. and Kashchiev, D.: "Pressure and Volume Evolution During Gas Phase Formation in Solution Gas Drive Process," *SPEJ* (September 1996) 219-227.
12. Firoozabadi, A.: "Author's Reply to Discussion of Pressure and Volume Evolution During Gas Phase Formation in Solution Gas Drive Process," *SPEJ* (June 1997) 228-231.
13. Handy, L.L.: "A Laboratory Study of Oil Recovery by Solution Gas Drive," *Petr. Trans. AIME*, **213** (1958) 310-315.
14. Hornbrook, J.W., Castanier, L.M. and Petit, P.A.: "Observation of Foam/Oil Interactions in a New, High-Resolution Micromodel," Paper SPE 22631 presented at the 66th Annual Technical Conference and Exhibition of the SPE, Dallas, TX (6-9 October 1991).
15. Hunt Jr., E.B. and Berry Jr., V.J.: "Evolution of Gas from Liquids Flowing Through Porous Media," *AIChE*, **2** (1956) 560-567.
16. Kennedy, H.T. and Olson, R.: "Bubble Formation in Supersaturated Hydrocarbon Mixtures," *Petr. Trans. AIME*, **195** (1952) 271-278.

17. Kortekaas, T.F.M. and van Poelgeest, F.: "Liberation of Solution Gas During Pressure Depletion of Virgin and Watered-Out Oil Reservoirs," *SPERE* (August 1991) 329-335.
18. Kuhlman, M.I.: "Visualizing the Effect of Light Oil on CO_2 Foams," *JPT* (July 1990) 902-908.
19. Li, X., and Yortsos, Y.C.: "Visualization and Numerical Studies of Bubble Growth during Pressure Depletion," Paper SPE 22589 presented at the 66th Annual Technical Conference and Exhibition of the SPE, Dallas, TX (6-9 October 1991).
20. Li, X., and Yortsos, Y.C.: "Critical Gas Saturation: Modeling and Sensitivity Studies," Paper SPE 26662 presented at the 68th Annual Technical Conference and Exhibition of the SPE, Houston, TX (3-6 October 1993).
21. Li, X. and Yortsos, Y.C.: "Bubble Growth and Stability in an Effective Porous Medium," *Phys. Fluids A*, **6** (5) (May 1994) 1663-1676.
22. Li, X. and Yortsos, Y.C.: "Visualization and Simulation of Bubble Growth in Pore Networks," *AIChE* (February 1995) 214-222.
23. Li, X. and Yortsos, Y.C.: "Theory of Multiple Bubble Growth in Porous Media by Solute Diffusion," *Chem. Eng. Sci.*, **50** (8) (1995).
24. Madaoui, K.: "Conditions de Mobilité de la Phase Gazeuse lors de la Décompression d'un Mélange d'Hydrocarbures en Milieu Poreux," Thesis, Toulouse U., France (1975). [As cited by Firoozabadi, *et. al.* (1992)]
25. Mattax, C.C. and Kyte, J.R.: "Ever See a Water Flood?," *Oil and Gas J.* (16 October 1961) 115-128.
26. Moulu, J.C. and Longeron, D.L.: "Solution-Gas Drive: Experiments and Simulation," *Proc.*, 5th European Symposium on Improved Oil Recovery, Budapest (1989). [As cited by Firoozabadi, *et. al.* (1992)]
27. Owete, O.S. and Brigham, W.E.: "Flow Behavior of Foam: A Porous Micromodel Study," *SPERE* (August 1987) 315-323.
28. Peden, J.M. and Husain, M.I.: "Visual Investigation of Multiphase Flow and Phase Interactions Within Porous Media," Paper SPE 14307 presented at the 60th Annual Technical Conference and Exhibition of the SPE, Las Vegas, NV (22-25 September 1985).

29. Satik, C., Li, X. and Yortsos, Y.C.: "Scaling of Single-Bubble Growth in a Porous Medium," *Phys. Rev. E*, **51** (4) (April 1995) 3286-3295.

30. Stewart, C.R., Craig, F.F. and Morse, R.A.: "Determination of Limestone Performance Characteristics by Model Flow Tests," *Petr. Trans. AIME*, **198** (1953) 93-102.

31. Stewart, C.R., Hunt Jr., E.B., Geffen, T.M. and Berry Jr., V.J.: "The Role of Bubble Formation in Oil Recovery by Solution Gas Drive in Limestones," *Petr. Trans. AIME*, **201** (1956) 560-567.

32. Wall, C.G. and Khurana, A.K.: "Saturation: Permeability Relationships at Low Gas Saturations," *J. Inst. Pet.*, **57** (September 1971) 261-269.

33. Wall, C.G. and Khurana, A.K.: "The Effect of Rate Pressure Decline and Liquid Viscosity on Low-Pressure Gas Saturations in Porous Media," *J. Inst. Pet.*, **58** (November 1972) 335-345.

34. Wieland, D.R. and Kennedy, H.T.: "Measurement of Bubble Frequency in Cores," *Petr. Trans. AIME*, **210** (1957) 122-125.

35. Wood Jr., J.W.: "Bubble Formation in Rangely Field, Colorado," MS Thesis, Texas A&M U., College Station (1953). [As cited by Firoozabadi, *et. al.* (1992)]

36. Yortsos, Y.C. and Parlar, M.: "Phase Change in Binary Systems in Porous Media: Application to Solution Gas Drive," Paper SPE 19697 presented at the 64th Annual Technical Conference and Exhibition of the SPE, San Antonio, TX (8-11 October 1989).

37. Yortsos, Y.C.: "Discussion of Pressure and Volume Evolution During Gas Phase Formation in Solution Gas Drive Processes," *SPEJ* (June 1997) 223-227.

3.3 VISUALIZATION OF MULTIPHASE FLOW THROUGH POROUS MEDIA

(Bolivia Vega)

3.3 1 LITERATURE REVIEW

This literature review consists mainly of SPE papers published in the last fourteen years on topics related to foamy oil, the bubble nucleation process, and micromodel experiments. The contents of this section will cover the generalities collected from these topics through the work of the authors reviewed.

3.3.1.1 Foamy Oil

The oldest publication reviewed for this report dates from 1985, when *Callaghan et. al.* performed chemical analysis and component separation experiments on foamy oils. This analysis revealed that foam stability was removed from crude oil following alkali extraction. This could mean that the crude-oil surfactants responsible for the stabilization of crude-oil foams are of acidic nature, and also of molecular weight less than 400. They proposed that the amount of crude oil surfactants could be determined by extraction of acidic components in order to assess its likely foaming features.

One of the pioneers in the research of the phenomena known as "Foamy Oil" is Gerald Smith (1988), whose studies on the Lloydminster area of Canada crude oils led to the publication of a paper in 1988. In his paper, Smith states some basic features of foamy oil, namely: high primary production rates, low oil viscosity, high oil mobility, and the presence of a large number of mini bubbles that do not coalesce below the bubble point pressure.

Based upon several mechanical and thermodynamical principles, Smith's proposed hypothesis was that mechanical failure of the sand matrix around the well changes reservoir properties and leads to significant primary production of this heavy oil. Typically, primary recovery of heavy oil averages about 2-4% of the original oil, whereas

at Lloydminster primary recovery was estimated to be greater than 10 %. This complex fluid behavior is not understood yet.

Finally, he states one possible explanation for the existence of foamy oil. In very viscous oils, the bubbles of gas nucleated as a consequence of decrease in pressure can not overcome the viscous drag and coalesce. The bubbles remain mixed within the liquid and flowing with the oil.

Prats and Claridge (1995) propose another model and mechanism based primarily on the role of asphalteness in the preservation of small-radius bubbles. In this model, the asphalteness coat the gas bubbles with a semi-rigid layer, which prevents them from further growth and coalescence. Since the bubbles do not coalesce, they remain mixed and small enough to flow with the liquid phase. The asphalteness that remain in colloidal suspension in the oil phase is removed gradually for the coating process and reduces oil viscosity. This leads to the foamy-oil high primary recovery percentages. Finally, they propose the completion of several further research experiments in order to help in the verification of this model, and eventually the creation of a more reliable one.

Firoozabadi and Aronson describe the nucleation process in their paper as "an instantaneous process at the critical supersaturation pressure". The main goal of their work being to determine the efficiency of solution gas drive for light and heavy oils. Their experimental setup was composed of a visual coreholder, a high-pressure chromatography pump, pressure transducers, a constant temperature system, and a video camera. Through these experiments, they determined visually the bubble nucleation process and found out that solution gas drive becomes a very efficient process with a very high bubble density. The consequence: low gas mobility and high oil mobility. These features correspond to those described previously as foamy oil. Also they determined that the number of nucleated bubbles is a function of the rate of the pressure decline (the higher the rate of pressure decline, the higher the number of bubbles), and conclude that nucleation in porous media is an instantaneous nucleation process.

3.3.1.2 Hamaca Case

The Hamaca field in the Orinoco Belt in Venezuela has been studied because of its foamy-oil features. Huerta et. al. (1996), try to characterize foamy-oil behavior by a mechanism of bubbles entrained in the oil due to high viscosity, low gas diffusion coefficient and high asphaltene content. They conclude that the system has the ability to trap gas within the fluid due to these factors, and that it remains to be understood the role of asphaltenes and resins on the foamy oil behavior.

3.3.1.3 Micromodels and Nucleation

Regarding this topic, Ward and Levart (1984) published their studies of the conditions under which a gaseous phase would be in a stable equilibrium. They found out that this is possible in zones of roughness on the walls of the container and in the solid particles suspended in the liquid phase. And, this stability is preserved even in cases of the gas pressure being higher than the surrounding liquid pressure.

In their work, El Yousfi et. al (1997) reported the results of a set of experiments of bubble nucleation visualization designed to determine the nature of nucleation and bubble growth. They found no perfect correspondence of the actual phenomena with any of the proposed models of homogeneous and heterogeneous nucleation. They conclude that the microbubbles come from pre existing nucleation sites and their growth is developed through diffusion in a very large number of sites, and trapping occurs due to the capillary forces in the roughness of the solid.

Finally, Li and Yorstos (1995) propose the activation of nucleation sites due to the decline of pressure under a homogeneous process. They also ran a computer based pore network simulator, and by comparing experimental and simulated results, they confirmed most of their premises. Namely, the onset of nucleation from different sites, the growth of vapor clusters in ramified fashion, and the relevance of capillary effects in the growth process.

3.3 2 RESEARCH PROJECT

In petroleum engineering, the need for describing and modeling gas behavior at pressures below the bubble point inside a reservoir becomes a very important tool in the forecasting and improving of production.

As remarked by El Yousfi *et al.* (1997), "the understanding of the first step, bubble formation inside a porous medium, is quite poor". That is the main reason for which these experiments are meant to be performed, as a first step in the way of understanding such a case.

The micromodel is a device designed to simulate an actual core system in which the transport phenomena can be studied at a microscopic level, and in which it can be easier to estimate the pore network features for further considerations as an independent variable in the experiments performed.

A typical setup consists primarily of an etched square network pattern of pores and throats on a glass or silicon plate subsequently fused to another glass plate to create a 2-D system. It is enclosed in a vessel with two inlets and two outlets, which allow water and oil to penetrate the vessel and the micromodel, respectively. The water is provided to control external pressure of the micromodel, and eventually, the surrounding temperature. The oil is the wetting or immediate phase in the study, and it flows through the micromodel pattern due to a pressure differential provided by connecting the vessel to pressure sources that will control the pressure drop along the micromodel. The oil is expanded at a rate that allows us to reduce the pressure below the bubble point at a given temperature, triggering the nucleation process in the fluid.

The micromodel experiments allow us to obtain visual observations of the bubble nucleation processes that take place within the pore network. These observations are the initial step in the modeling of phenomena that occurs at the pore level, which requires a description of three basic steps in the gas production process, namely: rate of appearance and/or formation of gas bubbles; growth of these bubbles inside the pores and the development of a coalesced continuous phase that eventually occupies the medium.

The first fluid to be used in this research will be mineral oil (Kaydol). It was selected for its well-known and predictable properties; in order to get a comparison behavior against the results obtained later for heavy oil and/or other fluids.

In order to get a control parameter group for characterizing the mineral oil behavior along the experiments, the first step will consist of modeling the viscosity of mineral oil at a certain range of temperatures and pressures. This will allow us to obtain fluid data that can be subsequently related to the nucleation and the bubble-growth process. This work can also give an estimate of an approximate behavior of high viscosity oils, such as heavy oils, some of which present foamy characteristics such as those described previously in the review.

The scope of this research is to visualize the nucleation process along the pore network and check its relation with parameters such as pressure and temperature (this last parameter is directly related with the fluid's viscosity).

It is the goal of this investigation to be able to associate the parameters and properties of the fluid and its surroundings, with the mechanism under which the gas phase appears and flows with the liquid. If some kind of association could be made, it would contribute in the basics preliminaries for the construction of a model that accounts for all of the effects and features observed along the investigation and present in an actual reservoir.

3.3 3 CONCLUSIONS

Up to the present time, a number of experiments and hypothesis have been developed in order to understand and explain the process of bubble nucleation inside a porous medium. None of these have accounted satisfactorily for all of the features observed experimentally.

This research is intended to extend these investigations by means of micromodel experiments and visual observation of the phenomena. It also will try to associate the gas-phase behavior with the properties of the fluid and parameters of the experiment, in order to achieve a degree of predictability regarding this process.

3.3 4 REFERENCES

1. Callaghan *et al.* :"Identification of Crude Oil Components responsible for Foaming", *SPEJ* (April 1985) 171-174.
2. El Yousfi *et. al.*: "Physical Mechanisms for Bubble Growth During Solution Gas Drive," SPE 38921, paper presented at the SPE Annual Technological Conference and Exhibition (October 1997) 805-809.
3. Firoozabadi and Aronson: "Visualization and Measurement of Gas Evolution and Flow of Heavy and Light Oil in Porous Media," SPE 28930, 2-8, 14.
4. Huerta *et. al.*: "Understanding Foamy Oil Mechanisms for Heavy Oil Reservoirs During Primary Production", SPE 36749 (October 1996), 671-674.
5. Li and Yorstos: "Visualization and Simulation of Bubble Growth in Pore Networks", *AIChE Journal* **41**, No.2 (Feb.1995) 214-221.
6. Prats and Claridge: "A Proposed Model and Mechanism For Anomalous Foamy Heavy Oil Behavior", SPE 29243, paper presented at the International Heavy Oil Symposium (June 1995) 9-14, 17.
7. Smith: "Fluid Flow and Sand Production in Heavy-Oil Reservoirs Under Solution-Gas Drive", SPE Production Engineering (May 1988) 169-174, 176.
8. Treinen *et al.*: "Hamaca: Solution Gas Drive Recovery in a Heavy Oil Reservoir, Experimental Results," SPE 39031, paper presented at the 5th Latin American Petroleum Engineering Conference (September 1997) 1-5.
9. Ward and Levart: "Conditions for Stability of Bubble Nuclei in Solid Surfaces Contacting a Liquid-Gas Solution", *J.Appl.Phys.* **56** (2), (July 15,1984), 491-492, 499.
10. Ward *et. al.*: "Stability of Bubbles in a Closed Volume of Liquid-Gas Solution," *J.Appl.Phys.* **53** (9) (September 1982) 6084.

3.4 GAS DRIVE IN HEAVY OILS

(Prabhat Arora)

3.4.1 INTRODUCTION

A number of heavy-oil reservoirs around the world are currently being produced under primary depletion. These reservoirs show certain anomalous production patterns like high oil production rates, high recovery and low producing GOR. The oil at the well-head has the appearance of a 'chocolate mousse' with a high amount of gas dispersed in it. These oils have thus been popularly termed 'foamy oils'.

Foamy oils may be formally defined as heavy oils containing dispersed gas bubbles. The phenomenon of foamy oil production was first reported in the Lloydminster area in Canada which has been under production for around fifty years now. The anomalous trends in this area were initially attributed to extensive sand production from the reservoir. It was believed that large sand-cuts led to the formation of extensive horizontal holes and channels in the sub-surface causing the permeability of the reservoir to be artificially enhanced. These high permeability channels were termed 'wormholes'. However, similar production behavior was later reported in the Orinoco basin in Venezuela with no significant sand-cuts (Claridge and Prats, 1995). Moreover, although the 'wormhole' hypothesis could account for the high productivity, it could not explain other trends like a low producing GOR. In other foamy oil reservoirs, alternate explanations like water or compaction drive were proposed but none of them were consistent.

A number of models have been proposed in the literature to explain the production behavior of foamy oil reservoirs. Much experimental work has also been done in trying to characterize solution gas drive in these oils. However, foaming in heavy oil reservoirs and its consequences are still not well understood. The focus of the present work is to make a mechanistic population balance model for foamy heavy-oil flow in porous media. The long-term objective is to be able to predict the anomalous production trends seen in actual reservoirs of this nature.

3.4.2 LITERATURE REVIEW

Smith (1988) was the first to propose a model for foamy-oil reservoirs with emphasis on production in the Lloydminster area. The model incorporated effects of both fluid-flow and solid mechanics in trying to match the production trends. It was argued that the effective viscosity of the foamy oil was intermediate between that of the original oil and gas and this reduction in viscosity caused the high productivity. It was also concluded that the supposed phenomenon of enhancement of permeability due to wormholes was only minor and could not explain the large increases in apparent mobility.

Claridge and Prats (1995) built upon Smith's ideas to propose a model for foamy oil production. They attributed the stability of gas bubbles in oil to the formation of a semi-rigid coating of asphaltenes and resins around them. The resulting removal of the heavy asphaltene molecules from the oil caused a decrease in oil viscosity which led to the high productivity. Moreover the coating over the gas bubbles stabilized them against coalescence and this prevented a continuous gas phase from being formed.

Huerta *et. al.* (1996) carried out PVT analysis of Hamaca crude oil and observed a pseudo oil-bubble phase which was stable for a long time. They also measured the viscosity of oil under solution gas drive as it was depressurized. It was found that there was no decrease in oil viscosity with increasing evolution of the gas phase. These observations went against the viscosity reduction hypothesis of Claridge and Prats (1995).

Sheng *et. al.* (1997) carried out foam stability tests on Lindbergh crude and studied foam stability as a function of oil viscosity, dissolved gas content, pressure decline rate and asphaltene content. Their experiments could not conclusively characterize the effect of asphaltene content on foam stability. So the role of asphaltenes as surfactants for bubble stabilizing was also not clear.

The objective of the present study is to use the available experimental knowledge on heavy oil foaming, blend it with bubble nucleation and growth models for porous media and make a population balance model for foamy oil flow. The aim

will be to match results with heavy-oil solution gas drive experiments (Akin and Kovscek, 1999).

3.4.3 POPULATION BALANCE MODEL

A population balance is a number balance on a species and is similar in concept to a mass balance. Population balance models are thus easy to incorporate into commercial reservoir simulators. For the case of foam flow in a porous medium, the general population balance equation can be written as follows (Kovscek and Radke, 1994):

$$\frac{\partial}{\partial t}[\phi(Sfnf + Stnt)] + \frac{\partial}{\partial x}(ufnf) = \phi Sg(rg - rc) + Qb \tag{1}$$

In the above equation, t denotes time, x is the axial location, u_f is the Darcy velocity of the flowing foam, S_f is the gas saturation for flowing foam, S_t is the gas saturation for the trapped foam, n_f and n_t are the number of foam bubbles per unit volume of flowing and stationary gas, r_g and r_c are the foam generation and coalescence rates per unit total gas volume and Q_b is a source-sink term. Thus, the above equation incorporates both flowing and trapped foam. The first time derivative term represents the rate of texture change of both flowing and trapped bubbles. The spatial derivative term accounts for the convection of the flowing foam. The right hand-side (Eq. 1) gives the net rate of foam generation and accounts for any source or sink.

Mass balance equations for gas and oil are written as follows:

$$\frac{\partial}{\partial t}[\phi \rho_g S_g] + \frac{\partial}{\partial x}(\rho_g u_g) = Q_g \tag{2}$$

$$\frac{\partial}{\partial t}[\phi \rho_o S_o] + \frac{\partial}{\partial x}(\rho_o u_o) = Q_o \tag{3}$$

During the early-time evolution of bubbles in solution gas drive, there is no flowing component of foam and the corresponding terms of the population balance drop out.

Also assuming no source-sink, we get:

$$\frac{\partial}{\partial t}[\phi(Stnt)] = \phi Sg(rg - rc) \tag{4}$$

To complete the population balance model we need analytical expressions for the two rate terms r_g and r_c. For obtaining these expressions it is important to understand the origin of gas bubbles in a porous medium through nucleation and their subsequent growth. We can assume that there is no bubble death due to coalescence because of the formation of a rigid asphaltene coating on them; bubbles of a certain size 'die' by growing due to mass transfer. The next two sections discuss the current literature on bubble nucleation and growth in porous media.

3.4.4 BUBBLE NUCLEATION

Bubble nucleation in porous media is not very well understood and the existing models in the literature are contradictory. Bubble nucleation in a bulk liquid in the absence of a porous medium is termed homogeneous nucleation. It has been shown that homogeneous nucleation requires a very high degree of super-saturation and so is unlikely for the pressure decline conditions in a porous medium (Li and Yortos, 1993). However heterogeneous nucleation, which is nucleation in the presence of a solid surface, is possible as the free energy change of this mode of nucleation is less than that of homogeneous nucleation (Defay *et al.*, 1966). Further due to surface roughness, there are cavities inside pores that stabilize the gas nucleus by their geometry. The rate of heterogeneous nucleation is thus greater than homogeneous nucleation for the same supersaturation.

Yousfi *et al.* (1997) carried out an experimental study of bubble nucleation in glass and resin micromodels. They recorded the number of bubbles nucleated as a function of time for pressure decline in a CO_2-water system. It was found that there is a minimum critical supersaturation ΔP_c below which there is no bubble nucleation. Further, at any fixed supersaturation above ΔP_c there is continuous bubble evolution for a certain time period following which there is no new nucleation. These observations were contradictory to both heterogeneous and homogeneous nucleation

models. A new model of nucleation was thus proposed by Yousfi *et al.* (1997) which viewed bubble nucleation as a three step process:

1. Pre-existence of microbubbles in surface cavities inside pores or instantaneous nucleation of bubbles in cavities.
2. Growth of these microbubbles inside cavities where they are trapped due to capillary forces.
3. Release of the microbubbles when supersaturation exceeds the capillary barrier corresponding to the cavity size.

A similar 'capillarity controlled nucleation' approach was adopted by Li and Yortos (1995a) in their model for multiple bubble growth in a porous medium. They considered nucleation to be the release of trapped bubbles from a cavity. The nucleation condition for a conical cavity of mouth radius W was given by:

$$KC - P_l \geq 2\gamma / W \tag{5}$$

where C and P_l are the solute concentration and liquid pressure at the interface and γ is the interfacial tension. Thus, the nucleation characteristics for a given system are determined only by the cavity size distribution and the applied supersaturation.

In the present work, we will use the model given by Eq. 5 to determine the rate of bubble nucleation. For the case of a constant liquid withdrawal rate, the supersaturation of the system keeps increasing with time leading to more cavities being activated and thus there is progressive nucleation. The rate of foam generation will be obtained from the bubble generation rate.

3.4.5 BUBBLE GROWTH IN POROUS MEDIA

After a bubble is nucleated, it grows in size by mass transfer of solute from the surrounding liquid. Like nucleation, bubble growth in a porous medium is different

from that in bulk liquid. The bulk growth of a spherical bubble by diffusion is given by the expression (Yousfi *et. al.*, 1997):

$$r^2 = 2kRTDt(\Delta P / P) \tag{6}$$

where r is the bubble radius, k is the solubility constant, R is the gas constant, T is temperature, D is the diffusion coefficient and ΔP is the applied supersaturation. It can be seen that the bubble radius increases as $t^{1/2}$. For growth of a bubble in a porous medium, this model is valid only when the bubble size is small compared to the pore dimensions as there is no interaction of the bubble with the porous solid. The validity of this model for small bubble sizes has been confirmed experimentally by Yousfi *et. al.* (1997).

When bubble sizes approach pore dimensions, capillary forces become important and the growing bubble gets trapped at the throats of the pore. The penetration of the bubble into an adjacent pore occurs via the largest throat where the capillary forces are the minimum. Thus, bubble growth occurs via two repeating steps, pressurization of the bubble by solute diffusion and volume expansion of the bubble (Li and Yortos, 1995a). This kind of bubble growth is analogous to invasion percolation except that here invasion occurs from an internal source. Another important factor in the growth of bubbles in a porous medium is the presence of multiple growing clusters that compete for the same amount of solute. Thus, mass transfer rates to the different bubbles determine the growth rate of each.

Li and Yortos (1995a) carried out a systematic study of single and multiple bubble growth in a porous medium. Based on visualization studies (Li and Yortos, 1995b) and scaling analysis (Satik *et. al.*, 1995), they identified different bubble growth regimes and found the time dependence of bubble size in each regime. For a single cluster, growth occurred by penetration of one throat at a time when the cluster was small. This was termed the percolation regime. When the bubble size became sufficiently large, viscous pressure drops in the liquid became appreciable and there was simultaneous penetration of more than one throat. This regime was termed viscous fingering. These ideas were extended to the simultaneous growth of multiple clusters and it was argued that for this case growth occurs only by percolation. However, three distinct percolation patterns could exist depending on the conditions.

For the case of a constant liquid withdrawal rate, Li and Yortos came up with the following functionality for cluster radius of gyration,

$$R \propto (Qt)^{1/Df} \tag{7}$$

where Q is the liquid withdrawal rate and D_f is the fractal dimension of the gas cluster for both two and three-dimensional systems.

Expression (7) will be used to estimate the bubble growth size for the foam in the population balance expression.

3.4.6 SUMMARY

The objective of this project is to come up with a population balance model for heavy oil foam flow in a porous medium. This report has presented the first few steps towards achieving this goal. The basic idea is to formulate expressions for foam generation and coalescence from bubble nucleation and growth theory. The existing literature for bubble nucleation and growth in porous media has been evaluated and relevant models have been identified. It is important to point out that lack of coherent experimental data on foamy oils and the limited understanding of the process of solution gas drive makes the task ahead tough. Thus the first step in this study would be to effectively model solution gas drive for mineral oils. The model would then be extended to the case of foamy oil flow in reservoirs. The long term objective is to come up with a model that can be incorporated into current reservoir simulators and effectively predict the anomalous production trends in foamy oil reservoirs.

3.4.7 REFERENCES

1. Akin, S. and Kovscek, A.R.: "Heavy Oil Solution Gas Drive Reservoirs: An Experimental Study," in progress.
2. Claridge, E.L. and Prats, M.: 'A Proposed Model and Mechanism for Anomalous Foamy Heavy Oil Behavior" SPE 29243, presented at the International Heavy Oil Symposium , Calgary, Alberta (June 19-21, 1995) 9-20.
3. Defay, R., Prigogine,I. and Bellemans,A. (1966), :Surface Tension and Adsorption, translated by Everett,D.H., John Wiley and Sons, New York.

4. Firoozabadi, A. and Kasiev, D. (1996), 'Pressure and Volume Evolution during Gas Phase Formation in Solution Gas Drive Processes', *SPE J.* (Sept.), 219-227.
5. Huerta, M., Otero, C., Rico, A., Jimenez, I., de Mirabal, M. and Rojas, G.: "Understanding Foamy Oil Mechanisms for Heavy Oil Reservoirs During Primary Production," presented at the 1996 SPE Annual Technical Conference and Exhibition, Denver (October 6-9, 1996), 671-685.
6. Kovscek, A.R. and Radke, C.J.: "Fundamentals of Foam Transport in Porous Media," Foam: Fundamentals and Applications in the Petroleum Industry, Schramm, L.L., Ed., *Advances in Chemistry Series 242, American Chemical Society, Washington D.C.* (1994)
7. Li, X. and Yortos, Y.C.: "Critical Gas Saturation: Modeling and Sensitivity Studies," Paper SPE 26662, Houston (1993).
8. Li, X. and Yortos, Y.C.: 'Theory of Multiple Bubble Growth in Porous Media by Solute Diffusion', *Chem. Eng. Sci.*, **50**(8), (1995a) pp 1247-1271
9. Li, X. and Yortos, Y.C.: "Visualization and Simulation of Bubble Growth in Pore Networks," *AIChE J.*, **41**(2), (1995b) pp 214-222
10. Satik,C.,Li,X. and Yortos,Y.C.: "Scaling of Single-Bubble Growth in a Porous Medium', *Phys. Rev. E*, **51**(4), (1995) pp 3286-3295
11. Sheng, J.J., Maini, B.B., Hayes, R.E. and Tortike, W.S.: "Experimental Study of Foamy Oil Stability," *JCPT*, **36**(4), (1997) pp 31-37
12. Smith, G.E.: "Fluid flow and Sand Production in Heavy Oil Reservoirs Under Solution gas Drive," *SPE Production Engineering,* (May 1988) 169-180.
13. Yousfi, A. El, Zarcone, C., Bories, S. and Lenormand, R.: "Physical Mechanisms for Bubble Growth During Solution Gas Drive," SPE 38921, paper presented at the 1997 Annual Technical Conference, San Antonio (October 5-8, 1999) 805-809.

3.5 Reservoir Simulation of Foam Displacement Processes

(Anthony R. Kovscek)

This paper was presentation at the 7th UNITAR International Conference on Heavy Crude and Tar Sands, October 27 – 31, 1998, in Beijing, China,

UNITAR

Reservoir Simulation of Foam Displacement Processes

Anthony R. Kovscek, Petroleum Engineering Department, Stanford University, Green Earth Science Building, Stanford University, Stanford, California, 94305-2220 USA

This paper was prepared for presentation at the 7th UNITAR International Conference on Heavy Crude and Tar Sands, October 27 – 31, 1998 in Beijing, China,

This paper was selected for presentation by the Conference technical committee based on material submitted in the abstract. Contents of the paper may be edited for clarity and consistency of format. The material as presented, does not reflect any position of UNITAR, the UNITAR Centre for Heavy Crude and Tar Sands, its officers, or members. Views expressed in the paper are those of the authors and not necessarily those of their respective companies. In submission of this paper, authors convey copyright to the Unitar Centre for Heavy Crude and Tar Sands, where applicable. Electronic reproduction, distribution, or storage of any part of this paper for commercial purposes without the written consent of the UNITAR Centre is prohibited. Permission to reproduce in print is restricted to an abstract of not more than 500 words; illustrations may not be copied. The abstract must contain conspicuous acknowledgment of where and by whom the paper was presented. Write UNITAR Centre for Heavy Crude and Tar Sands, c/o NPTO, PO Box 3628, Tulsa, OK 74101-3628. Phone 918 699 2045, Fax 918 699 2048, or email unitar@unitarhots.org

Abstract

Steam injection has had a profound impact on the production of heavy crude oil. Steam, however, is inviscid compared to a viscous oil and is not the ideal displacement agent. Field studies and laboratory tests have shown that foaming the steam phase through the aid of a suitable surfactant in aqueous solution can achieve mobility control of injected gases and mitigate the effects of gravity override. Thus, production is improved. Unfortunately, simulation models and simulation tools that accurately gauge the effects of foam on gas mobility in porous media are not readily available.

Recent advances in modeling gas mobility in the presence of foam are reviewed. These include the so-called bubble population balance method, scaling arguments to obtain representative foam texture and hence gas mobility, and semi-empirical alteration of gas mobility. The bubble population balance is then illustrated by means of a few sample calculations.

Introduction

Field application of foam is becoming a proven technology, surfactant costs withstanding, to control the mobility of gaseous phases in porous media. Typical applications span from steam[1-4] and CO_2 foam[5] to alleviate gravity override and channeling, production well treatments to reduce gas-oil ratio (GOR)[6,7], to gelled-foams[8] for long-lasting plugging of high permeability channels. Foam processes have also been studied and field tested for use as groundwater aquifer clean up methods[9-11].

To date, there have been about 25 major steam-foam projects implemented[12]. The attributes of fields subjected to foam are varied. Fields range from thick, steeply dipping sands where the objective is to improve vertical sweep, to flat, moderately thick reservoirs where gravity override is a concern, to improving injection profiles in layered reservoirs so that steam is injected into unheated zones. Foams are also useful to improve the distribution of heat during steam soaks.

With this considerable body of field knowledge in regard to steam foam, it would seem that we should be able to chose and evaluate candidate fields effectively. However, the highly nonlinear flow properties of foam in porous media and the widely varying chemistry of surfactants with respect to temperature and sensitivity to oil make generalizations difficult. Thus, more efficient application of foam EOR processes, especially steam-foam, would result from a comprehensive model of the process. In particular, a mechanistic model would expedite scale-up of the process from the laboratory to the field and the extrapolation of results from one field to another.

Foams in Porous Media

It is widely accepted that foam bubble size controls the mobility of foam in porous media[13]. Finely textured foams (small bubble size) are much less mobile than coarsely textured foams (large bubble size). It is also well known that foam flow behavior is strictly non-Newtonian[13,14]. In order to understand the phenomena

that a foam simulator must be capable of reproducing, the configuration of foam within rock pore space and the pore-level events that alter the size and shape of bubbles are discussed briefly.

Figure 1 depicts schematically a picture of the pore-level distribution of foam that has emerged from micromodel observations, pore-level modeling, and core floods[14-17]. In this highly schematic picture, sand grains are cross-hatched. For illustrative purposes only, the largest channels lie at the middle of the figure whereas the smallest lie at the bottom. Wetting surfactant solution is denoted as the dotted phase. Foam bubbles are either unshaded or darkly shaded, depending upon whether they are stationary or flowing.

Due to strong capillary forces, wetting liquid occupies the smallest pore spaces and clings to the surface of sand grains as wetting films. The aqueous, wetting phase maintains continuity throughout the pore structure shown in Fig. 1 so that the aqueous-phase relative permeability function is unchanged in the presence of foam[18-23]. Minimal volumes of liquid transport as lamellae. Unshaded flowing foam transports as trains of bubbles through the largest and least resistive flow channels. Because the smallest pore channels are occupied solely by wetting liquid and the largest pore channels carry flowing foam, significant bubble trapping occurs in the intermediate-sized pores.

Bubble volumes are roughly the same as individual pore volumes, or larger, and lamellae span across pore cross sections completely. This configuration is denoted a confined foam, as opposed to a bulk foam[17]. This terminology acknowledges the role of the porous medium in constricting foam configuration and shaping bubbles.

Foam reduces gas mobility by decreasing gas relative permeability and increasing gas effective viscosity. Stationary or trapped foam blocks a large number of channels that otherwise carry gas. Gas tracer studies measure the fraction of gas trapped within a foam at steady state in sandstones to lie between 85 and 99% [15,24]. Bubble trains within the fraction that does flow encounter drag because of the presence of pore walls and constrictions[25], and because the gas/liquid interfacial area of a flowing foam bubble is constantly rearranged by viscous and capillary forces[13].

Bubble and trains of bubbles are in a constant state of rearrangement. Bubbles and lamella transport some distance, are destroyed, and then regenerated. Further, trains halt when the local pressure gradient is insufficient to keep them mobilized, and other trains then begin to flow.

Foam texture arises from a balance between varied and complicated foam generation and destruction mechanisms. Regardless of whether foam bubbles are generated *in situ* or externally, they are molded and shaped by the porous medium[14,16]. Foam generation is largely a mechanical process, and it is sensibly independent of the type of surfactant. Bubbles are created by snap-off and division at germination sites that are a function of pore geometry of fluid occupancy. Surfactant stabilizes the gas/liquid interface of foam bubbles and prevents coalescence. Hence, foamer concentration and formulation affect the rate of foam coalescence.

The interaction of foam bubbles and oil is also important to gas mobility. Some foams are stable in the presence of oil while others are not. Sensitivity to the presence of oil increases foam coalescence. Thus, foam bubble size increases, and subsequently the foam mobility increases also. While there is no general agreement and a theory consistent with all observations of stability, foam stability in the presence of oil does appear to correlate with the oil entering coefficient[26]. That is, if oil can enter the gas-surfactant solution interface the oil can destabilize the foam.

More thorough reviews of foam generation, coalescence, and transport on the pore level are given by Chambers and Radke[16] and Kovscek and Radke[17].

Simulator Attributes

It is unlikely that any simulation approach/simulator can reproduce all observations of foam phenomena. It is also not necessary that a process simulation model be mechanistic in order to be successful. However, there are certain attributes that appear to be important for successful foam modeling on the reservoir scale:

- Gas mobility must be reduced in the presence of foam. In a simulation approach, this may be accomplished by reducing the gas relative permeability, increasing the gas viscosity, or a combination of both.
- Computed foam mobilities should incorporate some notion of non-Newtonian foam flow behavior because flow rates vary between the well-bore region and deep in the reservoir. Moderate to finely textured foams are decidedly shear thinning.
- Foam properties vary with surfactant concentration and must be modeled. Likewise foam stability in the presence of oil varies with surfactant type and

must be modeled.

- Surfactant transport, partitioning, and adsorption must be accommodated accurately.
- The method should be predictive rather than merely history matching.

In summary, foam properties vary with space and time, and must be modeled accordingly. Likewise, surfactant/brine transport must be modeled in some fashion.

Foam Flow Simulation Methods

A variety of methods have been proposed to incorporate foam into reservoir simulators. They range from empirical and semi-empirical alteration of gas mobility to population balance methods. We discuss the methods and the simulators that result.

Empirical Methods. Perhaps the simplest means of including the effects of foam in a simulator is through the use of a constant mobility reduction factor, *MRF*. That is, the gas relative permeability is divided by a constant value

$$k_{rf}(S_g) = \frac{k_{rg}(S_g)}{1 + MRF} \qquad (1)$$

If the foam is very strong, the *MRF* is very large, and *vice versa*. To account for surfactant transport, a concentration threshold must be exceeded before the gas mobility is modified. Such a model has been employed in UTCHEM[10,11], a chemical flood simulator developed at the University of Texas at Austin.

The weakness in employing a constant *MRF* is that it varies with gas velocity, surfactant concentration, and the presence of oil. Furthermore, it is difficult to predict a single *MRF* that will describe an experiment or a field situation from first principles.

Another application of the mobility reduction factor concept is to tabulate *MRF* as a function of surfactant concentration, water and oil saturations, pressure, and gas velocity. The *MRF* appropriate to any condition is then found via table lookup. This is a flexible way to extend reservoir simulation to foam flow and could be applied to any variable that is found to influence foam generation and transport. Of course laboratory experiments or history-matching field results is necessary to obtain the relevant tabular data. Extrapolation outside the range of tabulation is also difficult.

This approach has been applied to ECLIPSE 200 (Geoquest). Unfortunately, the implementation is at odds with the physics of surfactant transport. Because foam affects gas-phase properties, surfactant is assumed to be a tracer in the gas-phase even though it is a solute dissolved in the aqueous phase,. Simulating surfactant transport correctly is a key to simulating transient foam processes. It is not clear how this aphysical assumption changes the predictive capabilities of the simulator.

Semi-Empirical Methods. A variety of techniques have been proposed for the semi-empirical alteration of gas mobility. Most have focused on modifying gas relative permeability, but gas-phase effective viscosity has been modified also. The essence of semi-empirical methods of foam simulation is to assign a functional form to the *MRF*. The form is based on experiments, field results, and conjecture.

The popularity of this method is, apparently, an outgrowth of the success with which results from the Kern River steam-foam pilots[3] were simulated. Patzek and Myhill used field and laboratory results to calibrate a model of performance in the Mecca pilot and then predicted the incremental oil recovery from the Bishop pilot without adjusting parameters[27]. Essentially, their simulator tracks the surfactant chemical species and accounts for surfactant partitioning from the aqueous phase. The surfactant partition coefficient is adjusted so that the simulated surfactant propagation rate is equal to the pilot foam propagation rate. It is assumed that foam exists whenever steam and aqueous surfactant are present in a grid block. The mobility reduction factor is an increasing function of aqueous surfactant concentration. Patzek and Myhill state that the model was coded into a predecessor of THERM (Scientific Software Intercomp), and it was never released generally.

The semi-empirical approach to foam modeling has also been used in STARS (Computer Modeling Group)[2,28]. Surfactant transport, adsorption, partitioning, and degradation are modeled rigorously. Foam is represented via Eq. (1) with explicit surfactant concentration, oil saturation, and gas velocity dependencies for MRF:

$$MRF = M\left(\frac{w_s}{w_s^m}\right)^{e_s}\left(\frac{S_o^m - S_o}{S_o^m}\right)^{e_o}\left(\frac{N_c}{N_c^m}\right)^{e_v} \qquad (2)$$

In Eq. (2), w_s is the aqueous concentration of surfactant, S_o is the oil saturation, e are exponents,

superscripts m refer to reference or maximum values of variables, and N_c is a capillary number

$$N_c = \frac{K\nabla p}{\sigma} \tag{3}$$

Here, K is the permeability, p the pressure, and σ the vapor/surfactant solution interfacial tension.

This formulation accounts for effects on performance due to surfactant concentration, the presence of oil, and via the capillary number portion, velocity effects on the mobility of foam. Interestingly, no liquid velocity dependence on *MRF* is shown in Eq. (2) nor is there a term for the effect of capillary pressure. Laboratory experiments have shown that these variables play an important role in foam performance. Presumably, Eq. (3) could be modified by including factors for liquid velocity and capillary pressure.

A partially mechanistic formulation based on the concept of a limiting capillary pressure for foam flow has also been proposed and incorporated into UTCOMP[29,30]. UTCOMP is a compositional simulator developed at the University of Texas at Austin. Essentially, if surfactant is present and capillary pressure is low, gas mobility is made small via a reduced gas relative permeability. There is no velocity dependence to the mobility reduction.

An alternative to modifying the gas-phase relative permeability is to employ an effective viscosity of the gas phase and thereby reduce gas-phase mobility when foam is present. Marfoe et al[31] employ such an approach with a relatively simple function of surfactant concentration, aqueous-phase saturation, and gas-phase velocity. Implicit in this formulation is that changes in foam bubble size, and thus mobility, correlate with foamed gas velocity and how far the porous medium is from irreducible water saturation.

A similar approach with a more complicated effective viscosity function including permeability and oil saturation has also been implemented [32]. It is postulated that foam effective viscosity varies according to

$$\mu_f = \mu_g \frac{\left[1 + Df_c(w_s)(S_w - S_{wr})f_k(k) + f_p(\nabla p)\right]}{\left(1 + ES_o^2\right)} \tag{4}$$

where μ is the viscosity, the subscripts f and g refer to foam and free gas, respectively, f_c is a function of surfactant concentration, S_{wr} is the irreducible water saturation, f_k is a function of absolute permeability, f_p is a function of the pressure gradient, and D and E are adjustable constants. In addition, it is assumed that the relative permeabilities of all phases are unique functions of the saturation of each phase. Strong foams that are effective in the presence of oil would have a large D and a small E. The various functions are determined by history matching and experimental observations.

Mechanistic Models. To date mechanistic models for foam simulation have lead to population balance approaches where the average number of foam bubbles per unit volume is tracked[24,33,34]. This balance is analogous to the usual mass and energy balances that comprise a simulator. Bubble texture is then used to predict foam mobility. For example, a conservation balance is written for the average concentration of bubbles

$$\frac{\partial}{\partial t}\left[\phi(S_f n_f + S_t n_t)\right] + \nabla \cdot (u_f n_f) = \phi S_g (r_g - r_c) \tag{5}$$

where ϕ is the porosity, S is saturation, n is bubble density or texture, u_f is the flowing foam velocity, and the subscripts f, t, and g refer to flowing foam, trapped foam, and gas, respectively. The total gas saturation is the sum of flowing and stationary portions. Hence, $S_g = S_f + S_t$. The first term on the left is the net change in foam texture, whereas the second is the convection rate of foam bubbles. On the right hand side, r_g and r_c are the foam generation and coalescence rates on a per volume of gas basis, respectively. Specific formulations for r_g and r_c are available in the literature[17,24,33,34]. These terms are important for they determine bubble texture, and through texture, gas mobility.

In addition to kinetic expressions for bubble generation and destruction, the conservation equations require flow rate relationships for each phase. For the flowing foam, the structure of Darcy's law is retained

$$u_f = \frac{-Kk_{rf}}{\mu_f}\nabla p_g \tag{6}$$

k_{rf} is the relative permeability to foam and μ_f is the foam effective viscosity. Although Eq. (6) is in the form of Darcy's law, it does not imply Darcy flow because foam effective viscosity is non-Newtonian.

In most population-balance formulations, foam effective viscosity is expressed as

$$\mu_f = \mu_g + \frac{\alpha n_f}{v_f^c} \qquad (7)$$

where α is a proportionality constant, v_f (= $u_f/\phi S_f$) is the foam interstitial velocity, and the theoretically based value of the exponent is 1/3. The validity of Eq. (7) is supported by the analysis of bubble flow in tubes.

Gas mobility in porous media in the presence of foam is also reduced by trapped foam blocking an appreciable amount of the pore space. This effect is usually incorporated through the relative permeability function. The clearest method of incorporating trapped gas saturation via relative permeability is to recognize that flowing foam selectively partitions to the largest pores and to adopt a "Stone-type" relative permeability model[17]. Hence, the flowing foam relative permeability is a function only of S_f [35]. Finally, a constitutive equation is needed to predict the fraction of gas that actually flows[24,34].

The strength of this approach is that a framework is provided to express numerically all of the relevant physics regarding foam flow. To date, a fully mechanistic, population-balance based simulator has not been available. However, Chevron did, apparently, use a proprietary population-balance based simulator to predict and evaluate the performance of a steam-foam pilot[12,36]. Additionally, it has been reported recently that the population balance equation was incorporated into a compositional, thermal reservoir simulator and the method was illustrated with sample calculations[37]. The simulator was called FOAM3D to illustrate its multidimensional capabilities.

A criticism of mechanistic, continuum approaches to foam simulation is that they require many variables and parameters. For example, the population balance approach of Kovscek *et al.*[17,34] employs 10 parameters in addition to the usual parameters describing multiphase flow. For comparison, the semi-empirical approach illustrated in Eq. (2) has seven adjustable parameters, whereas the semiempirical adjustment of foam effective viscosity given in Eq. (4) has two unknown parameters and three functions that remain to be specified. The advantage of the mechanistic approach is that most of these foam parameters have clear physical meaning and their values are set *a priori*.

Example Calculations

The implementation in STARS of semi-empirical reduction of gas mobility in the presence of foam has been illustrated in several papers[2,28,38]. Hence, no calculations are reported here. We do note that these authors report generally good performance of the simulator in regard to capturing features of foam performance in the field.

A simple example is used here to illustrate the application of the population balance method to field-scale, multidimensional reservoir simulation. Foam is injected into one-quarter of a confined five-spot pattern with 2.5 acre spacing. Hence, injector-to-producer spacing is 72 m (235 ft) and we simulate converging-diverging flow. The formation is assumed to be 20 m thick, have a homogeneous permeability of 1.3 d, a constant porosity of 0.25, and impermeable upper and lower boundaries. The system is specified to be isothermal, and air and foamer solution are injected simultaneously into the layer which is originally filled with brine. The injection well is partially completed across the lower 1/8 of the interval, whereas the production well is completed across the entire interval and maintained at a pressure of 4.8 MPa (700 psi). Injection rates for N_2 and aqueous solution are 15.5 and 0.85 m^3/d, respectively. The injection rates are such that the foam quality is roughly 95%. See ref [37] for more details.

To provide contrast with the highly efficient foam displacement to follow, simulations of unfoamed gas injection were completed first. Gas saturation contours in the vertical cross section are presented in Fig. 2 at 50, 100, 200 and 300 d. The gray-scale shading indicates the gas saturation. Unshaded portions of the graph refer to an S_g of zero, and progressively darker shading corresponds to larger S_g. Areas contacted by gas are poorly swept. Buoyancy quickly drives injected gas to the top of the formation, a gas tongue forms, and gas breakthrough at the producer occurs quite quickly.

After breakthrough, little desaturation occurs because pressure gradients are low and buoyancy prevents gas from contacting areas along the lower horizontal boundary. This is classical gravity override.

With simultaneous injection of N_2 and foamer solution, foam generates where surfactant and gas are present, and the results are dramatically different. Figures 3, 4, and 5 present S_g, n_f, and C_s, profiles respectively, in the vertical cross section at times of 50, 100, 200, and 300 days. In Fig. 3, the gas saturation contours indicate that both a strong displacement by foam is occurring and a weak displacement by the unfoamed gas ahead of the foam front. Near the injector, the high gas saturation region associated with the foamed gas

assumes a semi-spherical shape. The contours at later times in Fig. 4 illustrate that spherical growth and efficient displacement continue. The darkly shaded region immediately below the upper impermeable boundary indicates a tongue of unfoamed gas that forms due to gravity override.

Figure 5 illustrates foam texture as a function of time. The foamed regions correspond exactly with zones of high gas saturation. The bubble textures associated with black shading are 100 mm^{-3}, and the light-gray shading at the foam front is roughly 20 mm^{-3}. The most finely textured foams are found adjacent to the well bore where gas and liquid flow velocities are largest.

Interestingly, both Figs. 3 and 4 indicate a spherical zone of foam growth. A similar trend has been observed in the field. Specifically, compare to Fig. 14 of Ref. [27].

The most provocative result of this simulation is found in Fig. 5: surfactant is actually lifted in the formation above its injection point. Black shading indicates a concentration of 0.83 wt%. Foamed gas effectively desaturates the zone around the injector. Although the aqueous-phase relative permeability function is unchanged in the presence of foam, the low S_w results in low relative permeability and highly resistive flow for the aqueous phase. The flow of surfactant-laden water is rerouted and surfactant is pushed upward in the formation. In this example, gravity override has been effectively negated.

When foam reaches the upper boundary of the layer, displacement continues from left to right in the horizontal direction in a piston-like fashion that expels the resident liquid phase. Propagation is slow until the flow begins to converge.

Summary

A brief review of the physics of foam generation and flow in porous media was given in order to rationalize the attributes of a simulator that are necessary for successful calculation of foam flow on the reservoir-scale. Methods for predicting foam flow that have been incorporated into reservoir simulators were then discussed along with some limitations of each method.

Nomenclature

c = exponent in foam effective viscosity
e = exponent in expression for MRF
k_r = relative permeability
K = permeability
M = constant in expression for MRF
MRF = mobility reduction factor
N_c = capillary number
n = number density of foam
p = pressure
r = rate of foam generation/coalescence
S = saturation
v = interstitial velocity
w_s = surfactant concentration

Greek Letters

α = proportionality constant for foam effective viscosity
ϕ = porosity
μ = viscosity
σ = surface tension

Subscripts and Superscripts

c = coalescence rate
f = flowing foam
g = gas
g = generation rate
m = maximum
o = oil
s = surfactant
t = trapped foam
v = velocity

Acknowledgement

This work was supported by the Assistant Secretary for Fossil Energy, Office of Oil Gas and Shale Technologies of the U. S. Department of Energy under contract No. DE-FG22-96BC14994 to Stanford University.

References

1. Djabbarah, N.F., S.L. Weber, and D.C. Freeman: "Laboratory Design and Field Demonstration of Steam Diversion with Foam," SPE 20067, in Proceedings of the 60th California Regional Meeting, Ventura, CA April 1990).
2. Mohammadi, S.S., D.A. Coombe, and V.M. Stevenson: "Test of Steam-Foam Process for Mobility Control in S. Casper Creek Reservior," *J. Can. Pet. Tech.*, **32**(10) (1993) 49-54.
3. Patzek, T.W. and M.T. Koinis: "Kern River Steam-Foam Pilots," *J. Petr. Tech.*, **42**(4) (1990) 496-503.
4. Brigham, W.E. and L.M. Castanier: "Critique of a Steam Foam Pilot," FS 2, in Proceedings of the DOE/Niper Field Applications of Foam for Oil Production, Bakersfield, CA Feb. 1993).
5. Hoefner, M.L., E.M. Evans, J.J. Buckles, and T.A. Jones: "CO2 Foam: Results from Four Developmental Field Trials," SPE/DOE 27787, in Proceedings of the SPE/DOE Ninth Symposium on Improved Oil Recovery,

Tulsa, Oklahoma (April 17-20, 1994, Apr. 1994).
6. Krause, R.E., R.H. Lane, D.L. Kuehne, and G.F. Bain: "Foam Treatment of Producing Wells to Increase Oil Production at Prudhoe Bay," SPE/DOE 24191, in Proceedings of the SPE/DOE Eighth Symposium on Enhanced Oil Recovery, Tulsa, OK Apr. 1992).
7. Aare, M.G. and A. Skauge: "A Foam Pilot Test Aimed at Reducing Gas Inflow in a Production Well at the Oseberg Field.," Proceedings of the 8th European IOR Symposium, Vienna, Austria May 1995).
8. Friedmann, F., T.L. Hughes, M.E. Smith, G.P. Hild, A. Wilson, and S.N. Davies: "Development and Testing of a New Foam-Gel Technology to Improve Conformance of the Rangely-CO2 Flood," SPE 38837, in Proceedings of the SPE Ann. Tech. Conf. and Exhibition, San Antonio, TX Oct. 1998).
9. Peters, R.W., M.V. Enzien, J.X. Boulliard, J.R. Frank, V.J. Srivastava, J. Kilbane, and T. Hayes: "Nonaqueous-Phase-Liquids-Contaminated Soil/Groundwater Remediation Using Foams," Proceedings of the In-Situ Remediation: Scientific Basis for Current and Futre Technologies, Pasco, WA Nov. 1994).
10. Hirasaki, G.J., C.A. Miller, R. Szafranski, J.B. Lawson, D. Tanzil, R.E. Jackson, J. Londergan, and H. Meinardus: "Field Demonstration of the Surfactant/Foam Process for Aquifer Remediation," SPE 39393, in Proceedings of the SPE Ann. Tech. Conf. and Exhibition, San Antonio, TX Oct. 1997).
11. Hirasaki, G.J., C.A. Miller, R. Szafranski, J.B. Lawson, and N. Akiya: "Surfactant/Foam Process for Aquifer Remediation," SPE 37257, in Proceedings of the SPE International Symposium on Oilfield Chemistry, Houston, TX Feb. 1997).
12. Patzek, T.W.: "Field Application of Steam Foam for Mobility Improvement and Profile Control," *Soc. Pet. Eng. Res. Eng.*, **May**(1996) 79-85.
13. Hirasaki, G.J. and J.B. Lawson: "Mechanisms of Foam Flow in Porous Media: Apparent Viscosity in Smooth Capillaries," *Soc. Pet. Eng. J.*, **25**(2) (1985) 176-190.
14. Ettinger, R.A. and C.J. Radke: "Influence of Foam Texture on Steady Foam Flow in Berea Sandstone," *Soc. Pet. Eng. Res.Eng.*, 7(1) (1992) 83-90.
15. Gillis, J.V. and C.J. Radke: "A Dual-Gas Tracer Technique for Determining Trapped Gas Saturation During Steady Foam Flow in Porous Media," SPE 20519, in Proceedings of the 65th SPE Annual Technical Conference, New Orleans, LA September, 1990).
16. Chambers, K.T. and C.J. Radke: "Capillary Phenomena in Foam Flow Through Porous Media", in *Interfacial Phenomena in Petroleum Recovery*, N.R. Morrow, Editor. , Marcel Dekker Inc., New York, (1991) p. 191-255.
17. Kovscek, A.R. and C.J. Radke: "Fundamentals of Foam Transport in Porous Media", in *Foams in the Petroleum Industry*, L.L. Schramm, Editor. , American Chemical Society, Washington, D.C., (1994) p. 115-163.
18. Bernard, G.G., L.W. Holm, and L.W. Jacobs: "Effect of Foam on Trapped Gas Saturation and on Permeability of Porous Media to Gas," *Soc. Pet. Eng. J.*, **5**(4) (1965) 295-300.
19. Holm, L.W.: "The Mechanism of Gas and Liquid Flow Through Porous Media in the Presence of Foam," *Soc. Pet. Eng. J.*, **8**(4) (1968) 359-369.
20. Huh, D.G. and L.L. Handy: "Comparison of Steady- and Unsteady-State Flow of Gas and Foaming Solution in Porous Media," *Soc. Pet. Eng. Res. Eng.*, **4**(1) (1989) 77-84.
21. De Vries, A.S. and K. Wit: "Rheology of Gas/Water Foam in the Quality Range Relevant to Steam Foam," *Soc. Pet. Eng. Res. Eng.*, **5**(2) (1990) 185-192.
22. Friedmann, F. and J.A. Jensen: "Some Parameters Influencing the Formation and Propagation of Foams in Porous Media," SPE 15087, in Proceedings of the SPE California Regional Meeting, Oakland, CA April, 1986).
23. Sanchez, J.M., R.S. Schechter, and A. Monsalve: "The Effect of Trace Quantities of Surfactant on Nitrogen/Water Relative Permeabilities," SPE 15446, in Proceedings of the 61st SPE Annual Technical Conference, New Orleans, LA October, 1986).
24. Friedmann, F., W.H. Chen, and P.A. Gauglitz: "Experimental and Simulation Study of High-Temperature Foam Displacement in Porous Media," *Soc. Pet. Eng. Res. Eng.*, **6**(1) (1991) 37-45.
25. Falls, A.H., J.J. Musters, and J. Ratulowski: "The Apparent Viscosity of Foams in Homogeneous Beadpacks," *Soc. Pet. Eng. Res. Eng.*, **4**(2) (1989) 155-164.
26. Bergeron, V., M.E. Fagan, and C.J. Radke: "Generalized Entering Coefficients - A Criterion for Foam Stability Against Oil in Porous Media," *Langmuir*, **9**(7) (1993) 1704-1713.
27. Patzek, T.W. and N.A. Myhill: "Simulation of the Bishop Steam Foam Pilot," SPE 18786, in Proceedings of the SPE California Regional Meeting, Bakersfield, CA April 1989).
28. Mohammadi, S.S. and D.A. Coombe: "Characteristics of Steam/Foam Drive Process in Massive Multi-Zone and Thin Single Zone Reservoirs," SPE 24030, in Proceedings of the SPE California Regional Meeting, Bakersfield, CA April 1992).
29. Rossen, W.R., S.C. Zeilenger, J.X. Shi, and M.T. Lim: "Mechanistic Simulation of Foam Processes in Porous Media," SPE 28940, in Proceedings of the 69th Ann. Tech. Conf. and Exhibition of the SPE, New Orleans, LA Sept 1994).
30. Shi, J.X. and W.R. Rossen: "Simulation and Dimensional Analysis of Foam Processes in Porous Media," SPE 35166, in Proceedings of the Permian Basin Oil and Gas Conf., Midland, TX Mar. 1996).
31. Marfoe, C.H. and H. Kazemi: "Numerical Simulation of Foam Flow in Porous Media," SPE 16709, in Proceedings of the 62nd SPE Annual Meeting, Dallas, TX September, 1987).
32. Islam, M.R. and S.M. Farouq Ali: "Numerical Simulation of Foam Flow in Porous Media," *J. Can. Pet. Tech.*, **29**(4) (1990) 47-51.
33. Falls, A.H., G.J. Hirasaki, T.W. Patzek, P.A. Gauglitz, D.D. Miller, and T. Ratulowski: "Development of A Mechanistic Foam Simulator: The Population Balance

and Generation By Snap-Off," *Soc. Pet. Eng. Res. Eng.*, **3**(3) (1988) 884-892.

34. Kovscek, A.R., T.W. Patzek, and C.J. Radke: "A Mechanistic Population Balance Model For Transient and Steady-State Foam Flow in Boise Sandstone," *Chem. Eng. Science*, **50**(23) (1995) 3783-3799.
35. Stone, H.L.: "Probability Model for Estimating Three-Phase Relative Permeability," *J. Pet. Tech.*, **22**(2) (1970) 214-218.
36. Friedmann, F., M.E. Smith, W.R. Guice, J.M. Gump, and D.G. Nelson: "Steam-Foam Mechanistic Field Trial in the Midway-Sunset Field," *Soc. Pet. Eng. Res. Eng*, **9**(4) (1994) 297-304.
37. Kovscek, A.R., T.W. Patzek, and C.J. Radke: "Mechanistic Foam Flow Simulation in Heterogeneous Multidimensional Porous Media," *SPEJ*, **2**(4) (1997) 511-526.
38. Kular, G., K. Lowe, and D.A. Coombe: "Foam Application in an Oil Sands Steam Flood Process," SPE 19690, in Proceedings of the 64th Annual Technical Conf. of SPE, San Antonio, TX Oct 1989).

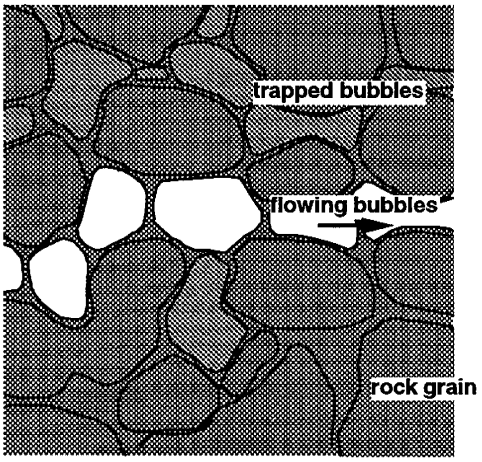

Fig. 1: Pore-level schematic of a flowing foam.

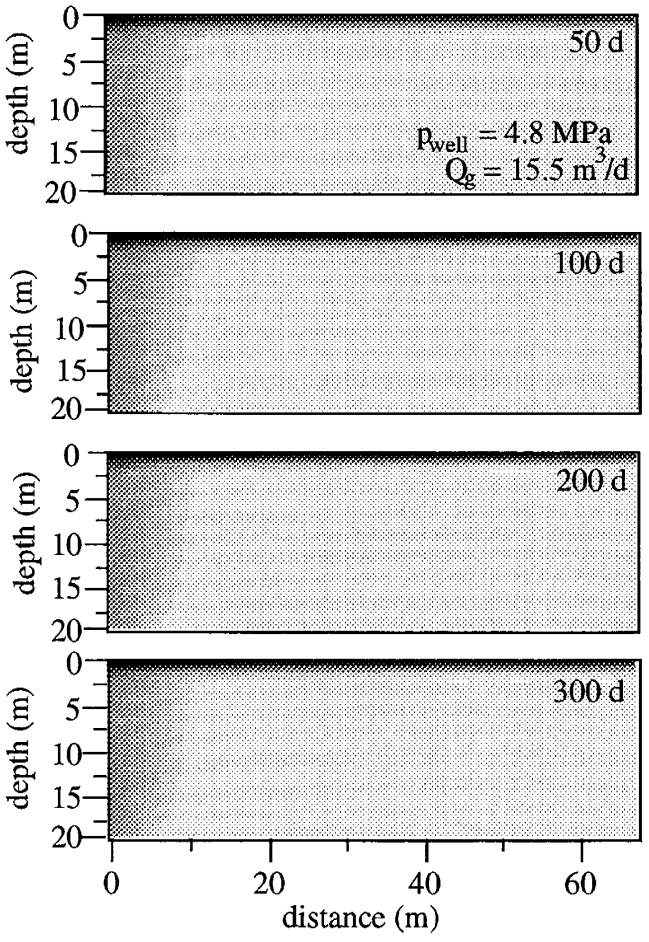

Fig. 2: Gas saturation profiles for unfoamed gas injection into a confined 5 spot.

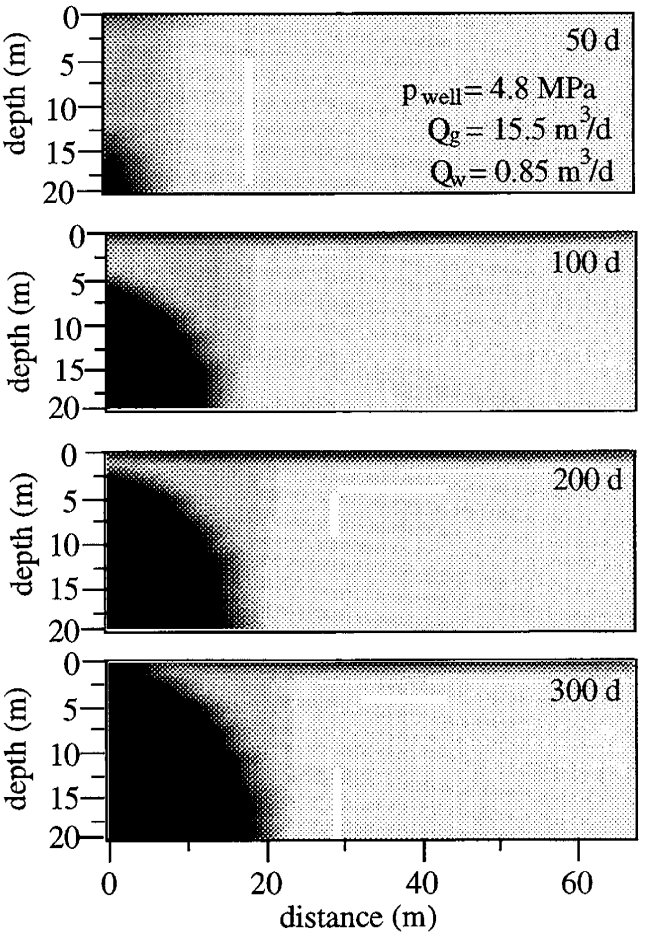

Fig. 3: Gas saturation profiles for the simultaneous injection of gas and foamer solution into a confined 5 spot.

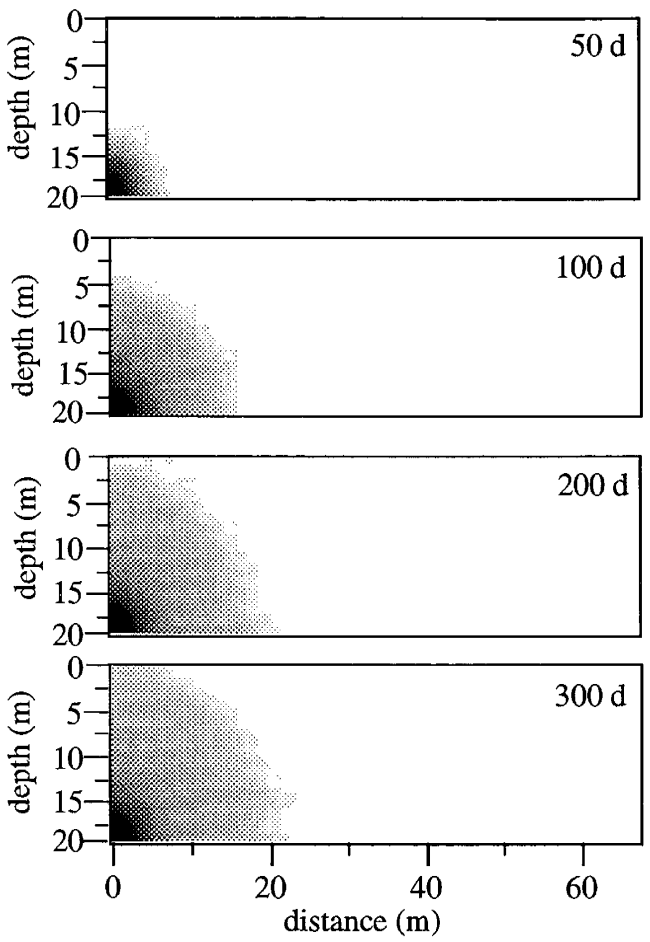

Fig. 4: Foam texture profiles for the simultaneous injection of gas and foamer solution into a confined 5 spot.

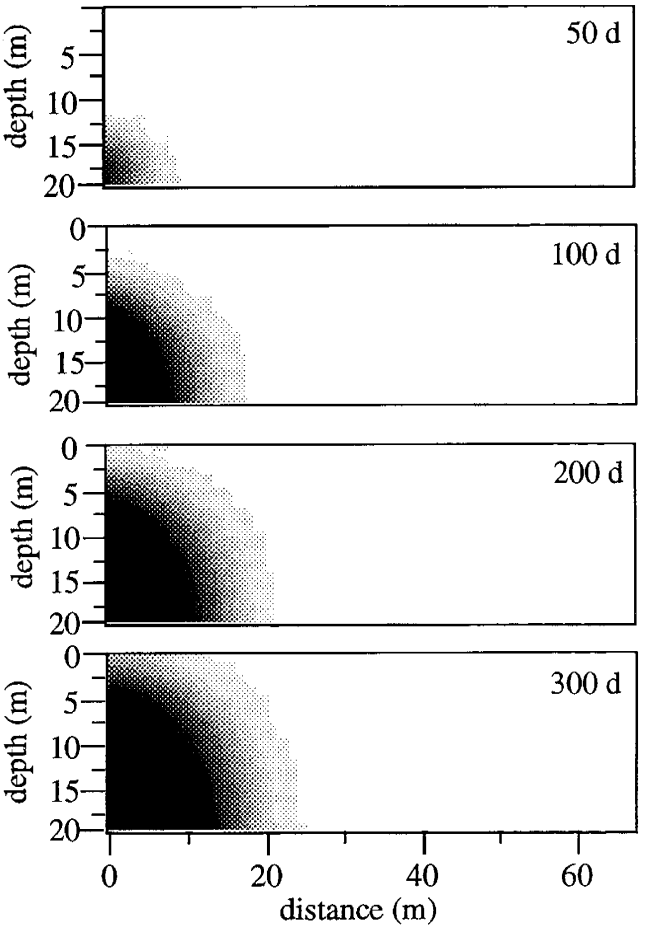

Fig. 5: Surfactant concentration profiles for the simultaneous injection of gas and foamer solution into a confined 5 spot.

PROJECT 4: RESERVOIR DEFINITION

To develop and improve techniques of formation evaluation such as tracer tests and pressure transient tests.

4.1 A STREAMLINE APPROACH TO INVERSE PROBLEMS

(Yuandong Wang)

4.1.1 INTRODUCTION

4.1.1.1 Brief Description of the Study

The current research topic is to apply the concept of streamlines to infer the permeability distribution of porous media based on production information. The production information includes the history of production rates, and the fractional flow of water and oil at the producer. Additional information includes injection rate and pressure.

Most approaches to this inverse problem manipulate parameters at the grid-block level and demand a great amount of computational work. By performing this process at the streamline level, the inverse process is speeded up tremendously and the cost is greatly reduced. In other words, streamline properties, such as permeability and porosity, are adjusted to match simulation and observation. By analyzing the sensitivity of the fractional flow at different times to permeability along the streamline, a method is developed to modify the permeability at the streamline level . Then, the modification at the streamline level can be converted to a modification at the grid-block level.

4.1.1.2 Example Problem to Solve

Assume that we are trying to retrieve the permeability distribution of a reservoir. What we know is the production and injection information. We may also have some information about the permeability distribution. For example, we may have some well logging data and geostatistical simulations provide realizations of the permeability distribution. However, the hard data such as the well logging data are very limited in amount and the geostatistical simulation is stochastic, encompassing many equi-probable realizations. By running flow simulations, we find that the production given the geostatistical permeability distributions does not necessarily match historical field

production. That is to say, the fractional flow curve or the flow rate in the simulation result does not match those in the field. That means the permeability field used for simulation is not correct, assuming other flow properties are properly represented in the simulation.

There are a number of ways to solve an inverse problem, such as simulated annealing, genetic algorithm, and sensitivity studies. As described in the literature review section, these approaches demand a great amount of computational work and, hence, are very time consuming. The proposed approach, by employing streamlines, is aimed at reducing the computational work by reducing the size of the inverse problem.

4.1.1.3 Importance of the Research

History matching plays an important role in reservoir engineering because of performance prediction and data interpretation. In many cases, we have water or tracer breakthrough, flow rate, and pressure information at the producers. If properly used, this information can be helpful in inferring the permeability distribution of a reservoir. Most approaches to this inverse problem manipulate parameters at the grid-block level because most simulators employ conventional finite difference techniques. Because there are many cells, and most of these approaches need to run flow simulation many times to get a satisfactory match, this inverse process involves a great deal of computational work. Therefore, it can be expensive depending on the problem. One approach is to develop very efficient optimization procedures for conventional simulators. Another approach is to conduct the optimization at the streamline level, where there is an opportunity to speed up the inverse inference of permeability distribution and also execution of the forward simulation.

4.1.2 LITERATURE REVIEW

This review discusses several methods for inventing reservoir production response.

4 1.2.1 Simulated Annealing

Simulated annealing (Gupta, *et al.*, 1994) is an analogue to the annealing of metal to improve the quality of metal. The objective is to minimize the "internal energy" of the system. When applied to our inverse problem, the quality that we seek to improve is the match between the observed and computed production data. The internal energy is the value of the objective function that indicates the error or mismatch. The parameters to be modified are the undetermined reservoir properties such as permeability.

For our inverse approach to infer the permeability distribution, the objective is to minimize the objective function as defined later in Section 6. The objective function is the error between the computed production data and the field production data. The parameter to manipulate is the permeability distribution. There are many grid blocks in this process. Starting from an initial permeability distribution, flow simulation is run to get the production data. Then the objective function is calculated. If the error is beyond the tolerance, then the permeability values are perturbed randomly in some grid blocks. The simulation is conducted again and the objective function is calculated. Then it is checked whether the objective function is reduced or not. If it is reduced, then the perturbed permeability field is accepted. If the objective function value increases, then the perturbation is accepted with a probability. The larger the objective function value, the less probable it is that we accept this modification.

The above process stops when the objective function is within the error tolerance or the objective function stops changing for several iterations. Each iteration includes perturbing the permeability, running flow simulation, and calculating the objective function.

This approach is time consuming and very expensive because each iteration involves running forward simulation and most of the time, many iterations are required for a good match. This is because there are many grid-blocks and the combination of a permeability distribution that can give us a good match to the production data is not easy to find within a few iterations. Sometimes, the solution can not be found because the method is stochastic. The solution of this approach is run-dependent. That means a different starting point may yield different results.

4.1.2.2 Sensitivity Coefficients

A sensitivity coefficient approach (Landa and Horne, 1997; Wen *et al.*, 1997) computes the sensitivity of the objective function(s) to the parameters being modified. In our case, the parameters are permeability values for each grid-block. The sensitivities can be expressed as the derivatives of the objective function(s) to each parameter. Then a system is solved.

$$M \bullet \Delta\vec{k} = -\vec{E} \tag{1}$$

where M is a matrix of the derivatives (the sensitivity matrix), $\Delta\vec{k}$ is a vector of the parameter modification, and $\vec{E}$ is a vector of objective functions.

This approach can be expensive if there are many grid-blocks and therefore many variables to manipulate. Computing the derivatives and solving the system requires great computational effort.

4.1.2.3 Geostatistical and Streamline Approach

A permeability field generated by geostatistics is not guaranteed to match the production data. Realizations may honor the measured permeability data and their spatial distribution and some other data correlated to permeability, such as porosity and seismic data. Geostatistics generates many stochastic realizations. When the flow simulation is run using these permeability distributions, some may match the production data, and others may not. If there are many realizations to test, this method can be expensive too.

Wen *et al. (1998)* presented a geostatistical approach to this inverse problem by integrating well production data. This approach includes two steps.

- Establish the spatial constraints on large-scale permeability trends caused by the production data using an inverse technique;
- Construct the detailed reservoir models subject to those spatial constraints by means of geostatistical techniques.

Their approach adapts the sequential self-calibration (SSC) inverse technique to single-phase multi-well transient pressure and production rate data. The SSC method is an iterative, geostatistically-based inverse method coupled with an optimization procedure that generates a series of coarse grid two-dimensional permeability realizations whose numerical flow simulations correctly reproduce the production data. This approach is said to be flexible, computationally efficient and robust.

However, this approach only applies for single-phase flow. For a two-phase flow with the displacing phase fractional flow data, it will be desirable to integrate those data. In fact, saturation information can provide information about the permeability distribution, such as flow channels and barriers. This is because the pressure equation is a transient response, and therefore, anything that happens in any location of the domain will propagate to the whole domain. However, the saturation equation provides local information. Fractional flow data is the representation of saturation information at the producer. Therefore employing the fractional flow data, integrates additional information into the inverse problem and helps to improve the match in the production data.

Vasco *et al.* (1998) applied streamlines to this inverse problem. They integrated dynamic production data into a reservoir model using streamline-based analytic sensitivity coefficients. This is essentially a sensitivity approach. The difference between this approach and other sensitivity approaches is the method to calculate the sensitivity coefficients. Other approaches may require a reservoir simulation to be run to obtain a sensitivity coefficient to a single parameter. The permeability value in each grid-block is a parameter. Therefore, the common way of calculating sensitivity is expensive. By employing streamlines and calculating the sensitivity analytically, the procedure for calculating the sensitivity is greatly speeded up. However, there is still a very big system to solve because the size of the system is proportional to the number of grid-blocks.

4.1.2.4 Streamlines and Mobility Ratio

A streamline is tangent everywhere to the velocity vector. Therefore, no flow can cross streamlines. In two-dimensional space, two streamlines form a stream tube. The flow rate in a stream-tube is the same as the flow rate in any other stream-tube (Thiele *et*

al., 1996). For streamlines, this equal flow rate property is also applicable. We use the terms stream-tubes and streamlines interchangeably. Streamlines are the representation of stream-tubes in three-dimensional space. There is a pore volume and a flow rate associated with each streamline. The flow rate associated with each streamline is the same. However, the pore volume of each streamline can be different from others. The difference in streamline pore volume results in different breakthrough times for different streamlines. The term, time of flight (TOF), indicates the pore volume of a streamline. The larger the pore volume associated with a streamline, the larger is its time of flight, and the later a displacement front in a particular streamline breaks through.

Because there is no flow across a streamline, we can represent the flow field by 1D-flow streams along each streamline. For a field with given permeability and saturation distribution, we can solve for the streamline distribution (pressure field). However, the saturation distribution changes with the progress of displacement. Therefore, the pressure field, as well as streamline distribution, might need to be solved many times to ensure accuracy. Whether it needs to be solved only once or many times depends on the mobility ratio of the displacement.

If the mobility ratio is unity, then the two phases have the same flow properties and the saturation distribution does not affect the pressure field. Therefore, the streamlines do not evolve with the displacement, and the streamline distribution needs to be solved only once. Every streamline has the same flow rate associated with it.

If the mobility ratio is very close to unity, then the streamline distribution may be solved only a few times to save the computational work and at the same time to ensure the required accuracy.

However, for non-unit mobility ratio, the streamline distribution evolves in the process of displacement. Then to achieve accuracy, the pressure distribution needs to be solved as many times. There are two ways to treat the evolution of streamlines.

1. Fix the flow rate and let the streamline position change. In this case, the flow rate is the same for every streamline and remains the same throughout the entire displacement process. However, the streamlines change position and

even the number of streamlines may change depending on the whether the total flow rate varies.

2. Fix the streamlines and let the flow rate associated with the streamlines change. When streamlines are fixed, the flow rate associated with a streamline changes depending on the mobility ratio.

4.1.2.5 Streamline Simulator (3DSL)

In most streamline simulators, we solve the pressure field for a given saturation distribution, obtain the streamline distribution, map the Buckley-Leverett solution along the 1D streamlines for a short time period, and then solve the pressure as many times as necessary. Because the pressure equations and saturation equations are decoupled, the simulation is speeded up significantly. We use the 3DSL streamline simulator by Batycky *et al* (1997). The accuracy and computational efficiency are satisfactory (Wang et al., 1999)

4.1.3 BASIC IDEAS

4.1.3.1 Streamline Breakthrough Versus Production Fractional Flow

Each streamline carries a certain amount of flow and has a specific pore volume associated with it. The breakthrough of each streamline contributes to the fractional flow at the producer(s). Assume there are N streamlines associated with a producer. For unit mobility ratio, the flow rate associated with each streamline is the same and remains constant throughout the displacing process. Each streamline contributes $1/N$ of total flow rate to the producer assuming incompressible fluid. Therefore, when each streamline breaks through, the fractional flow of the displacing phase increases by $1/N$. For non-unit mobility ratios, if the streamlines are assumed to be fixed but the flow rates can vary, then the increase of the fractional flow may not be $1/N$.

4.1.3.2 Permeability Modification along Streamlines

Assume that, in the example above, large differences are observed between the field and simulation fractional flow curves. If we know the order of the streamline breakthrough and how much a particular streamline contributes to the fractional flow, then, by examining where on the curve the differences lie, the streamlines that are responsible for the differences can be spotted.

Figure 1 shows an example. The dotted line is the observed fractional flow curve at the producer. The solid line is the simulation result. In the simulation result, the dimensionless time t_D for $f_w = 0.3$ is 0.6 (real time is 720 days) for Producer A. However, that same t_D in the field observation is 0.71 (real time 860 days) for the same producer. Then we know that the streamline responsible for that f_w in the simulation breaks through earlier than it should. By checking how many streamlines are connected to this producer, we can figure out how much a particular streamline breakthrough contributes to the fractional flow. Say, if there are 50 streamlines connected with this producer, then each streamline breakthrough contributes 0.02 to the fractional flow, assuming unit mobility ratio. Then we know that the 15^{th} streamline is responsible for the fractional flow $f_w = 0.3$. Therefore, to make that streamline breakthrough at the same time as in the field, the permeability along this streamline should be decreased to cause later breakthrough.

By computing the sensitivity of the fractional flow at different times to permeability along the streamline, a method to modify the permeability at the streamline level can be developed. This is discussed in detail in Equations.

The last step is to convert the modification at the streamline level to the modification at the grid-block level. More details are discussed in the Strategies of the Study.

4.1.4. STEPS OF THE STREAMLINE APPROACH TO THE INVERSE PROBLEM

1. Given a reference permeability field, use the 3DSL streamline simulator for forward simulation to obtain the reference water breakthrough curves at producers, the production rate, and pressure drop history between injectors and producers.
2. Generate an initial permeability field;
3. Run simulation. Check the match for breakthrough, flow rate and pressure drop. If it does not match the reference data, modify the permeability as in the following steps;
4. Work on the streamlines: Calculate the time of flight (or the associated pore volume) for all streamlines. Sort the streamlines in the order of the pore volume associated with the streamlines;
5. Locate the streamlines that need to be modified. Compute the difference in fractional flow, flow rate and pressure drop between the simulation result and the reference. For the breakthrough curve, check where the difference lies. Relate it to the corresponding streamline.
6. Modify the permeability value along the streamlines based on the difference of the t_D between the simulation result and reference for the same fractional flow.
7. Repeat Steps 3 to 6 until a satisfactory match is achieved.

4.1.5 STRATEGIES OF THE STUDY

4.1.5.1 Starting Simplifications

To start constructing the inverse method, the following assumptions are made to simplify the problem.

- Incompressible flow. If flow is compressible, then not all the streamlines connect an injector and a producer. Streamlines can begin anywhere in compressible flow. In

this case, we will have trouble tracing the streamlines, calculating their pore volumes, and predicting the breakthrough time of each streamline.

- Piston-like displacement. Along the streamline, flow is one-dimensional. In most of the cases, the 1-D flow is the Buckley-Leverett solution in which there is a shock followed by a spreading wave. By assuming piston-like displacement, we have a step change in displacing phase saturation. It will simplify the problem at the beginning of this study and we will relax this assumption later.
- Unit mobility ratio. Unit mobility ratio is where we start and we will consider non-unit mobility ratio later.
- Two dimensions. 2-D is simpler than 3-D, and the extension to 3-D should be straightforward.
- Single injector. For a single injector, all the streamlines start from the same location. For multi-injector cases, it is more difficult to trace, sort and work on the streamlines.
- No constraint of the permeability values or their distribution. Very small changes in porosity may result in large changes in permeability. When we modify the permeability in a grid-block, we do not modify the porosity, although they are co-related.
- Only permeability is to be modified.

Most of these assumptions will be removed later in the study to broaden its applicability.

4.1.5.2 Programming in C++

This study involves a great quantity of coding. It also involves many objects such as wells, streamlines, grids, production information (including fractional flow and flow rate) and petrophysical properties such as permeability. To more easily manage the code, it is written in an object oriented programming language, C++ serves this purpose.

4.1.5.3 Way to Modify the Permeability Distribution

The modification of permeability distribution is performed at two levels. As discussed above, by trying to match the fractional flow curve, we know which streamline to modify. By applying Newton's method and solving a linear system, the degree of modification to the effective permeability required along the streamline can be determined. This is at the streamline level.

However, this is the average permeability of the streamline and we need to modify the permeabilities of the cells. Sometimes a cell is connected with more than one streamline. For example, assume that streamlines i and j pass through the same cell, and that, for a good match, the permeability along streamline i is to be increased by a factor of 1.2, and that value for streamline j is 0.9. Then it is difficult to determine what value should be used to modify the permeability in this cell.

Therefore, when the modification is performed at the streamline level, the information about permeability modification along a streamline is saved for each cell it passes, but no modification of the cells are made. After all the information is collected, the decision can be made about the cell permeability. The exact procedures for making these decisions follow.

4.1.6 EQUATIONS

4.1.6.1 Objective Functions

In this problem, the objective function is a measure of the match between the simulation results and the field observation and its value is minimized. To be more precise, the objective function is a normalized error of the simulation results. Its value is minimized in this study. The objective function E is defined as

$$E = \sum_{i=1}^{N_p} E_i \tag{2}$$

where the subscript i is the index of producer. N_p is the number of producers. E_i is the error of producer i.

$$E_i = E_{tD,i} + E_{\Delta p,i} + E_{q,i} \tag{3}$$

$E_{tD,i}$ is the absolute error in dimensionless time for the same value of fractional flow, $E_{\Delta p,i}$ is the normalized error of the pressure drops between the injector and producers at producer i, and $E_{g,i}$ is the normalized of flow rate at producer i. They are defined below.

Error in Fractional Flow or Time

$$E_{t_D,i} = \frac{1}{N_{sl,i}} \sum_{j=1}^{N_{sl,i}} \left| e_{t,i,j} \right| \tag{4}$$

where $e_{t,i,j}$ is the normalized error in breakthrough time as defined below. $N_{sl,i}$ is the number of streamlines connected to producer i.

$$e_{t,i,j} = t_{D,i,j}^{C} - t_{D,i,j}^{R} \tag{5}$$

where $t_{D,i,j}^{C}$ and $t_{D,i,j}^{R}$ are the computed and reference dimensionless breakthrough time for j^{th} streamline at producer i, respectively. These are calculated from the fractional flow curve because streamline breakthrough is related to the fractional flow.

The quantity $e_{t,i,j}$ can also be expressed in terms of dimensional breakthrough time and normalized by reference breakthrough time, as in the alternative equation below.

$$e_{t,i,j} = \frac{t_{i,j}^{C} - t_{i,j}^{R}}{t_{i,j}^{R}} \tag{6}$$

All the terms are the same as defined above except that, without subscript D, t refers to dimensional time instead of dimensionless time in Eq. (4).

Error in Pressure

$$E_{p,i} = \left| e_{\Delta p,i} \right| \tag{7}$$

where $e_{\Delta p,i}$ is the normalized error in pressure at producer i as defined below.

$$e_{p,i} = \frac{\Delta p_i^C - \Delta p_i^R}{\Delta p_i^R} \tag{8}$$

where Δp_i^C and Δp_i^R are calculated and reference pressure drop between the injector and producer i, respectively.

The error in pressure is normalized by the reference pressure so that its absolute value will be within the range of 0 to 1 and it is of the same scale as the error in fractional flow.

Error in Flow Rate

$$E_{q,i} = \left| e_{q,i} \right| \tag{9}$$

where $e_{q,i}$ is the normalized error in flow rate at producer i as defined below.

$$e_{q,i} = \frac{q_i^C - q_i^R}{q_i^R} \tag{10}$$

where q_i^C and q_i^R are calculated and reference flow rate at producer i, respectively.

4.1.6.2 Systems to Solve for Modification of the Permeability along Streamlines

When permeability along one streamline is modified, not only the breakthrough time will change for this streamline, but also for other streamlines as well. Therefore, the modification of the permeability cannot be performed independently for each streamline. Instead, modification for all the streamlines should be performed simultaneously.

However, it will be convenient if the modification is decoupled for different producers. By doing so, a large system is split into several small systems. To solve several small sub systems is much easier and cheaper than to solve a large system.

Assume producer P is under study now. Connected to this producer are N streamlines. Each streamline breakthrough contributes $1/N$ to the fractional flow. Then the system to solve for this producer is

$$\begin{bmatrix} a_{11} & a_{12} & a_{13} & \cdots & a_{1N} \\ a_{21} & a_{22} & a_{23} & \cdots & a_{2N} \\ a_{31} & a_{32} & a_{33} & \cdots & a_{3N} \\ \cdots & & & & \\ a_{N1} & a_{N2} & a_{N3} & \cdots & a_{NN} \end{bmatrix} \begin{bmatrix} \Delta k_1 \\ \Delta k_2 \\ \Delta k_3 \\ \cdots \\ \Delta k_N \end{bmatrix} = \begin{bmatrix} e_{t,1} \\ e_{t,2} \\ e_{t,3} \\ \cdots \\ e_{t,N} \end{bmatrix} \tag{11}$$

where a_{ij} is the sensitivity of breakthrough time (dimensionless) of the i^{th} streamline to the permeability change along the j^{th} streamline. These are a_{ij}'s derivatives and can be computed as shown in the following subsection. The quantity t_{Dij} denotes the error of the breakthrough t_D (or normalized t) of the j^{th} streamline, as defined in Eq. 5 or 6.

It might be more convenient to modify the permeability by multiplying by a factor not by adding a value. Then the following equation will be more appropriate.

$$\begin{bmatrix} a_{11} & a_{12} & a_{13} & \cdots & a_{1N} \\ a_{21} & a_{22} & a_{23} & \cdots & a_{2N} \\ a_{31} & a_{32} & a_{33} & \cdots & a_{3N} \\ \cdots & & & & \\ a_{N1} & a_{N2} & a_{N3} & \cdots & a_{NN} \end{bmatrix} \begin{bmatrix} \delta k_1 \\ \delta k_2 \\ \delta k_3 \\ \cdots \\ \delta k_N \end{bmatrix} = \begin{bmatrix} e_{t,1} \\ e_{t,2} \\ e_{t,3} \\ \cdots \\ e_{t,N} \end{bmatrix} \tag{12}$$

4.1.6.3 Sensitivity Study – Computing of Derivatives

The element a_{ij} is the derivative of the breakthrough time of streamline i with respect to the permeability along streamline j.

$$a_{ij} = \frac{\partial t_{Di}}{\partial k_j} \tag{13}$$

This derivative can be computed by applying Dykstra and Parsons (1950) method for non-communicating layers. The method relates the breakthrough of different layers to the effective permeability for each layer. Changing the permeability of one layer changes the breakthrough time for all the layers. Streamlines can be treated as non-communicating layers. In this way, the derivatives above can be easily determined.

The breakthrough time for streamline n can be calculated by the following equation.

$$t_{D,n} = \frac{\sum_{j=1}^{N_{sl}} (\phi A x_D)_j}{(\bar{\phi} A_t)} \tag{14}$$

where $x_{D,j}$ is the dimensionless length of the displacing phase front of the j^{th} streamline when the n^{th} streamline breaks through. The porosity is ϕ, A_j is the cross-sectional area of streamline j, and A_t is the total cross-sectional area. For fast streamlines, $x_{D,j}$ can be greater than 1. Substituting $\frac{(\phi A)_j}{\bar{\phi} A_t}$ with $V_{D,l}$, Eq. 13 can be rewritten as

$$t_{D,n} = \sum_{j=1}^{N_{sl}} V_{D,j} x_{D,j} \tag{15}$$

where $V_{D,l}$ is the pore volume associated with streamline j.

In Eq. 14, t_D is a function of $x_{D,j}$, which can be expressed as a function of the permeabilities of all the streamlines. Therefore, to calculate the derivative of breakthrough

time of the n^{th} streamline to the permeability of the m^{th} streamline, we can apply the chain rule.

$$\frac{\partial t_{D,n}}{\partial k_m} = \sum_{j=1}^{N_{sl}} \frac{\partial t_{D,n}}{\partial x_{D,j}} \frac{\partial x_{D,j}}{\partial k_m} = \sum_{j=1}^{N_{sl}} V_{D,j} \frac{\partial x_{D,j}}{\partial k_m} \tag{16}$$

The Dykstra and Parsons (1950) method relates $x_{D,j}$ to the effective permeability of all the streamlines. The formula for calculating $x_{D,j}$ is different for unit mobility ratio and non-unit mobility ratios as described next.

Suppose there are N_{sl} streamlines connected to producer i . We are interested in how $x_{D,j}$ changes with the change of permeability at the m^{th} streamline.

For unit mobility ratio, the pressure field as well as the streamline distribution remains unchanged throughout the displacement process. Streamlines can be treated as non-communicating layers.

When breakthrough happens at streamline n, the front position at streamline j is calculated by

$$x_{D,j} = \frac{k_j}{k_n} \tag{17}$$

When the permeability of a streamline changes, the above derivative can be expressed as

$$\frac{\partial x_{D,j}}{\partial k_m} = \begin{cases} -k_j / k_n^2, & if\ m = n\ and\ n \neq j \\ 0, & if\ n = j \\ 1/k_n, & if\ m = j,\quad m \neq n \\ 0, & if\ m \neq j, m \neq n \end{cases} \tag{18}$$

Therefore,

$$\frac{\partial t_{D,n}}{\partial k_m} = \sum_{j=1}^{N_{sl}} V_{D,j} \frac{\partial x_{D,j}}{\partial k_m} = \begin{cases} -\dfrac{1}{k_n^2} \sum\limits_{j=1, j\neq n}^{N_{sl}} V_{D,j} k_j, & if\ m = n \\ 1/k_n, & if\ m \neq n \end{cases} \tag{19}$$

$$\frac{\partial t_{D,n}/t_{D,n}}{\partial k_m/k_m}=\frac{\partial(\ln t_{D,n})}{\partial(\ln k_m)}=\begin{cases}-\dfrac{1}{k_n^2}\displaystyle\sum_{j=1,j\neq n}^{N_{sl}}V_{D,j}k_j\frac{k_n}{\displaystyle\sum_{j=1}^{N_{sl}}V_{D,j}k_j/k_n}\approx -1, & if\ m=n\\ \dfrac{V_{D,m}}{k_n}\dfrac{k_n}{\displaystyle\sum_{j=1}^{N_{sl}}V_{D,j}k_j/k_n}=\dfrac{V_{D,m}k_n}{\displaystyle\sum_{j=1}^{N_{sl}}V_{D,j}k_j}\approx\dfrac{1}{N_{sl}}, & if\ m\neq n\end{cases} \tag{20}$$

$\partial t_{D,n}/\partial k_m$ is a function of permeability and streamline pore volume. However, $\dfrac{\partial t_{D,n}/t_{D,n}}{\partial k_m/k_m}$ are constants and much easier to compute.

When the n^{th} streamline breaks through, the front position in streamlines that broke through earlier than n are located at,

$$x_{D,j}=1+\left(\frac{k_j}{k_n}-1\right)\left(\frac{1+M}{2}\right) \tag{21}$$

For streamlines that break through later than the n^{th} streamline,

$$x_{D,j}=\frac{\left[M^2+\dfrac{k_j}{k_n}(1-M^2)\right]^{1/2}-M}{1-M} \tag{22}$$

where M is the end point mobility ratio of the displacing phase to the displaced phase.

With Eqs. 20 and 21, $\partial x_{D,j}/\partial k_m$ can be easily computed using the same method as in the unit mobility case. But now the derivative is not only a function of permeability but also a function of mobility ratio.

In the same way for the unit mobility case, we substitute $\partial x_{D,j}/\partial k_m$ into Eq. 15, compute $\partial t_{D,n}/\partial k_m$, and simplify the derivative by computing $\dfrac{\partial t_{D,n}/t_{D,n}}{\partial k_n/k_m}$.

4.1.7 PRELIMINARY RESULTS, PLANS AND EXPECTATIONS

4.1.7.1 Preliminary Results

I obtained promising results with this approach. In the reference field, there are one injector and two producers. Between the injector and Producer 1 there exists a high permeability channel, and between the injector and Producer 2 there is a low permeability barrier as shown in Fig. 2. Starting from a homogeneous permeability field, both the breakthrough and pressure drops are far away from the reference (see Figs. 3 and 4). After three iterations, a very good match both in pressure drops and breakthrough curves is obtained. This indicates that this approach converges rapidly, much faster than most of the other approaches to this inverse problem.

Figure 4 plots the errors versus the number of iterations. The solid line in Fig. 4(a) is the sum of the errors at the two producers. The dashed and dotted lines are for each producer, respectively.

Comparing the computed permeability field with the reference field in Fig. 2, we find that, with this approach, the high permeability channel is retrieved quite accurately. For the barrier, the resolution is not as accurate. However, we have good matches for the breakthrough curve and pressure drop.

4.1.7.2 Plans

Develop the Method, Design Code and Implement the Code

This is the main task of the study and is currently in progress.

Remove the Assumptions

The assumptions listed above in Section 4.1.5.1 limit the application. Therefore, the simplifications should be removed to broaden its application. Our plan is to relax

- Piston-like displacement to Buckley-Leverett solution;
- Unit mobility ratio to non-unit mobility ratio;
- Two dimensional to three dimensional;
- Single injector to multi injectors;

Apply Geostatistics

There is no constraint of the permeability values or their distribution as yet. Placing constraints on the permeability values and distributions with the use of other information such as well log data and seismic data may accelerate the process and improve the method. On the other hand, trends revealed by the well log data and seismic data and other resources should be honored. Geostatistical techniques should be integrated into this approach to make use of those data.

Make Comparison with Other Approaches

For comparison, we will develop examples that use a conventional history-matching approach to infer the permeability distribution. We will then compare accuracy, computational efficiency and applicability.

4.1.8. NOMENCLATURE

A	area, L^2
A_j	cross-sectional area of streamline j, L^2
A_T	total cross-sectional area, L^2
E	Absolute error
e	Relative error
f_w	fractional flow of water
h	bed thickness, L
k	permeability, L^2
k_{ro}	relative permeability of oil
k_{rw}	relative permeability of water
l	length, L
L_i	length of stream tube i, L
M	mobility ratio
p	pressure, $M/L \bullet T^2$
q	flow rate, L^3/T
S	saturation
S_w	water saturation
t_D	dimensionless time
V_D	dimensionless volume (pore volume)
x_D	dimensionless length
w	width of a stream tube, L
ϕ	porosity

4.1.9 REFERENCES

1. Gupta, A. D., Vasco, D. W., and Long J.C.S.: "Detailed Characterization of Fractured Limestone Formation Using Stochastic Inverse Approaches," SPE Ninth Symposium (1994).

2. Landa, J. L.; Horne, R. N., "A Procedure to Integrate Well Test Data, Reservoir Performance History and 4-D Seismic Information," SPE 38653, paper presented at the 1997 Annual Technical Conference, San Antonio (October 5-8, 1999).

3. Wen, X.H., Clayton, D.V., Cullick A.S.: "High Resolution Reservoir Models Integrating Multiple-Well Production Data," paper presented at the 1997 Annual Technical Conference, San Antonio (October 5-8, 1997).

4. Vasco, D.W., Yoon, S., Datta-Gupta, A.: "Integrating Dynamic Data Into High-Resolution Reservoir Models Using Stramline-Based Analytic Sensitivity Coefficients", SPE 49002, 1998.

5. Thiele, M. R., Batycky, R. P., Blunt, M. J. and Orr Jr, F. M., Jr.: "Simulating Flow in Heterogeneous Systems Using Streamtubes and Streamlines," *SPE. Reservoir Engineering* **11**, 5, (1996).

6. Batycky, R. P., Blunt, M. J., and Thiele, M. R.: "A 3D Field-Scale Streamline-Based Reservoir Simulator," *SPE Reservoir Engineering* **12**, 1997.

7. Wang, Y.D., Kovscek, A. R. and Brigham, W.E.: "Effect of Mobility Ratio on Pattern Behavior of a Homogeneous Porous Media", *In-Situ*, 1999.

8. Dykstra, H. and Parsons, R.L.: "The Prediction of Oil Recovery by Waterflood," Secondary Recovery of Oil in the United States, Principles and Practice, 2nd ed., American Petroleum Institute (1950), 160-174.

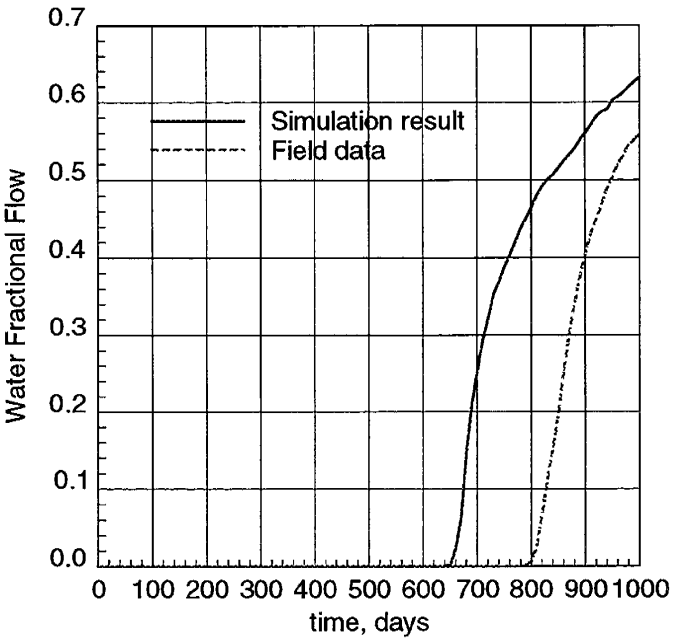

Fig 1. Streamline Breakthrough vs Fractional Flow

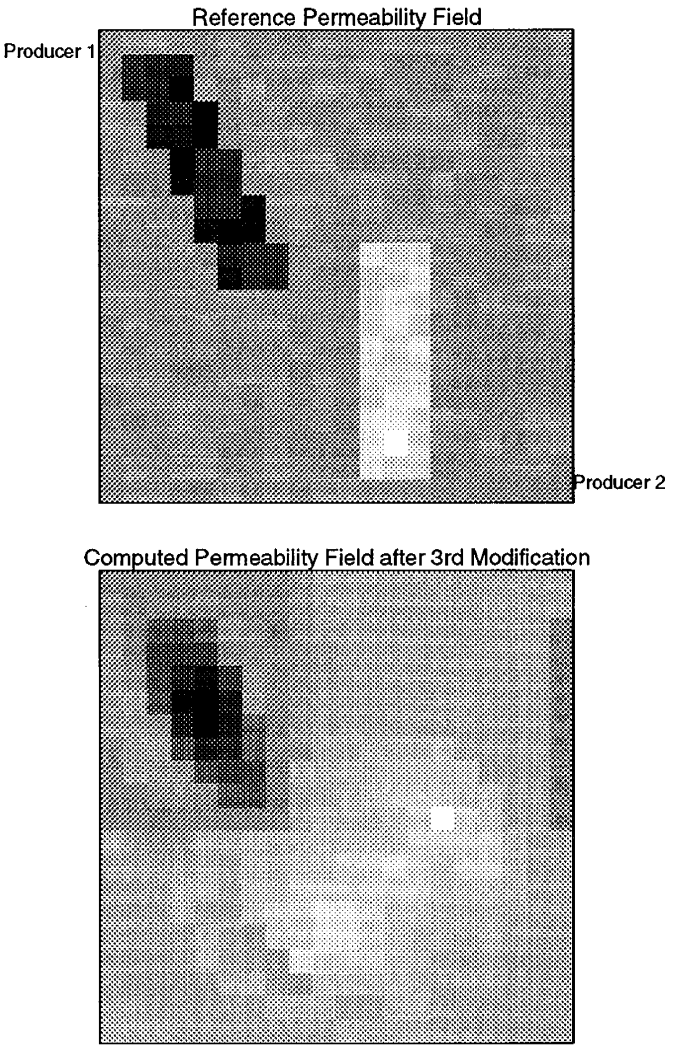

Fig. 2 Comparison on Permeability Field

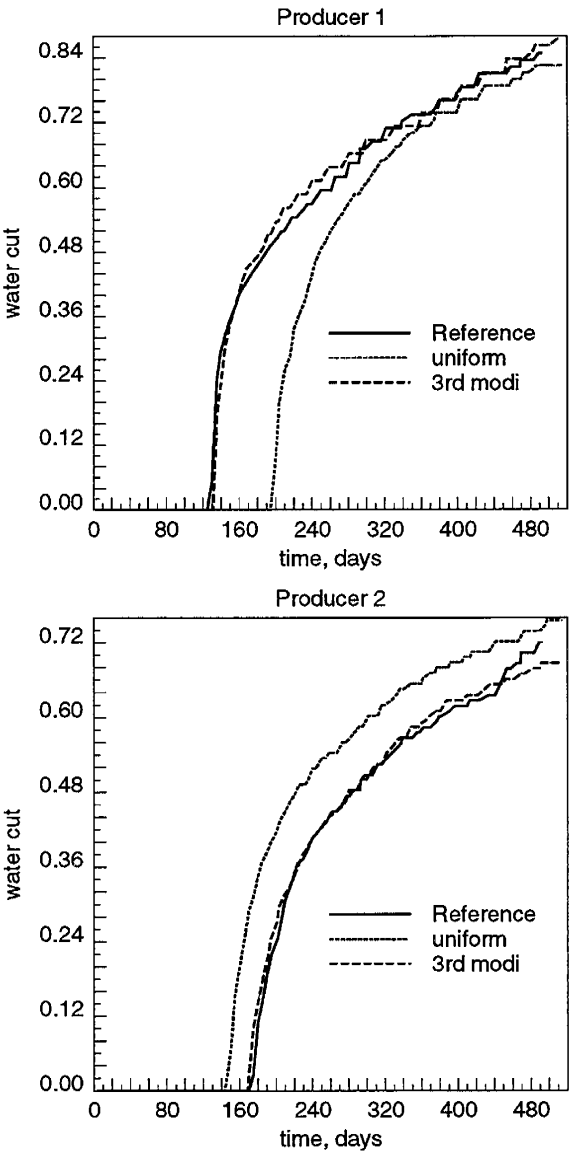

Fig. 3 Comparison on Breakthrough Curve

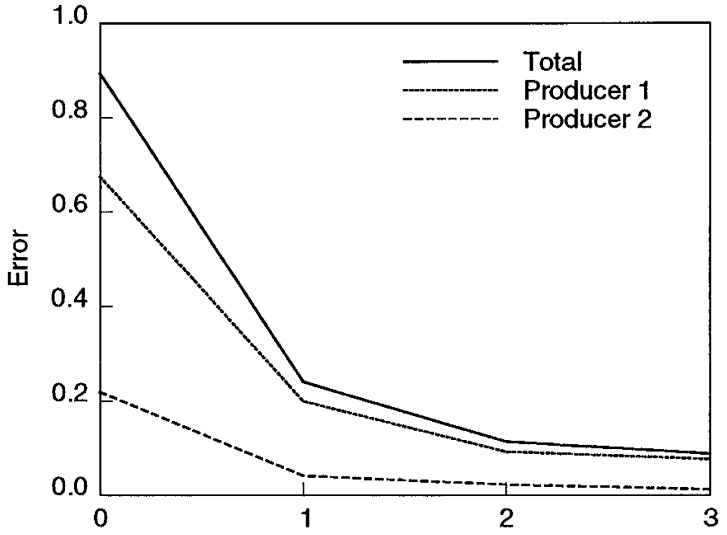

(a)

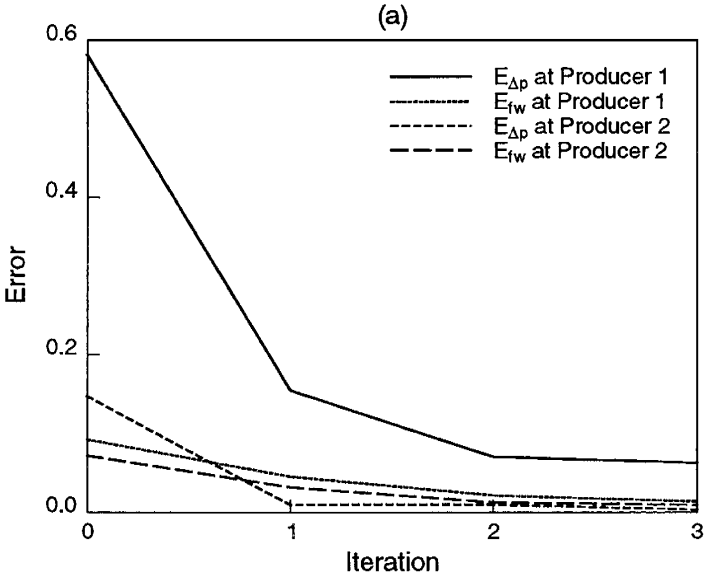

(b)

Fig. 4 Error vs Iterations

4.2 DISPLACEMENT EFFICIENCES FOR DIRECT-LINE DRIVE AND EDGE-WATER DRIVEWATERFLOODING USING STREAMTUBE MODELS

(Amos O. Kehinde)

4.2.1 SUMMARY

Waterflooding is one vital improved oil recovery option which has widespread application, but is yet to benefit fully from the modern reservoir management practices of prior- and post- implementation performance evaluation by simulation. This is because, generally, it is still difficult to model entire fields accurately. Streamtube modeling, which primarily involves flow profiling from a source (the injector) to a sink (the producer), offers a qualitative and quantitative approach to conceptualizing waterflood displacement mechanisms. This work is an application of streamtube modeling to predicting performance of oil/gas reservoirs on waterflood, with particular reference to direct-line and edge-water injection schemes.

4.2.2 INTRODUCTION

Several modeling techniques have contributed to our understanding of waterflood displacement mechanisms since its accidental discovery in the Bradford field, Pennsylvania in the late 19^{th} century. Yet, our understanding would benefit further from new contributions in this area. Waterflooding is attractive for many operational, economic, and technical reasons. Not surprisingly, it is a natural preference for improved recovery from oil/gas reservoirs. Water is readily available onshore and offshore, accounting for $4/5^{th}$ of the earth's areal surface. Our current understanding of its chemical and physical properties makes water handling onshore and offshore relatively easy, thus making it even more attractive among other cheap and available options for improved recovery from oil/gas reservoirs.

The sweep efficiency of a waterflood scheme is determined by reservoir properties, drive patterns, reservoir depletion planning, and development strategies. Three patterns of most common use in the industry are direct-line drive, staggered-line drive, and 5-spot patterns, as shown in Fig. 1. They are all based on applying a repeated injector/producer geometry across a field. However, for steeply dipping reservoirs, peripheral or edge-water injection flood configuration is an option to consider.

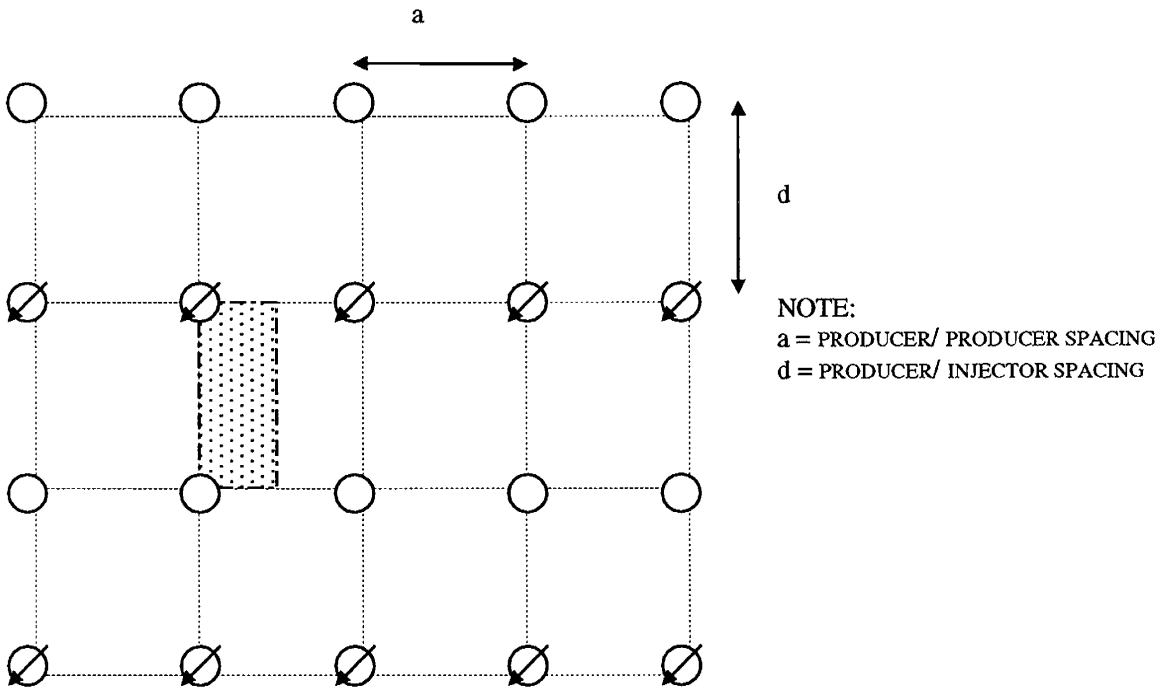

Figure 1(a). Direct Line Drive Pattern. The shaded area marks the element of symmetry for the pattern. Aspect ratio is d/a.

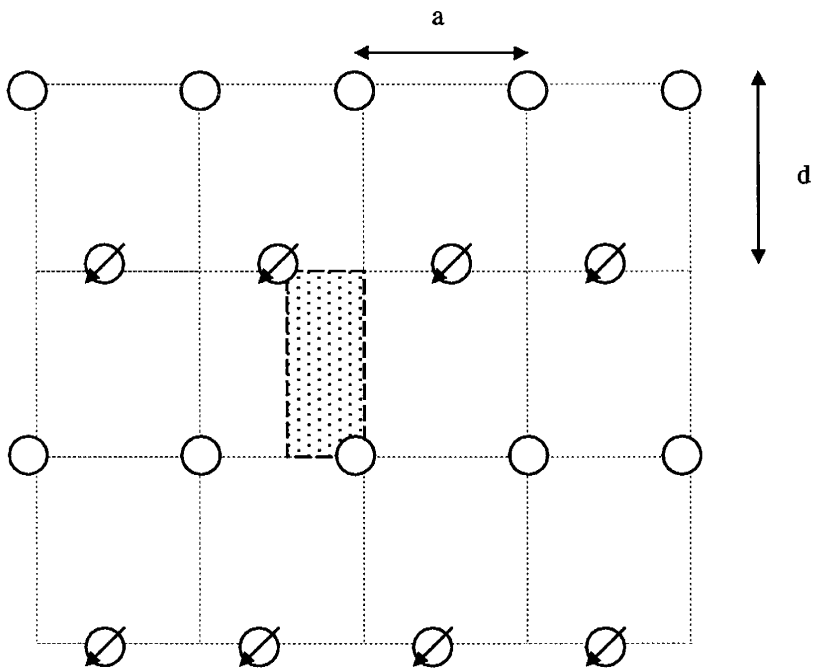

Figure 1(b). Staggered-Line Drive Pattern. The shaded area marks the element of symmetry for the pattern.. Aspect ratio is d /a.

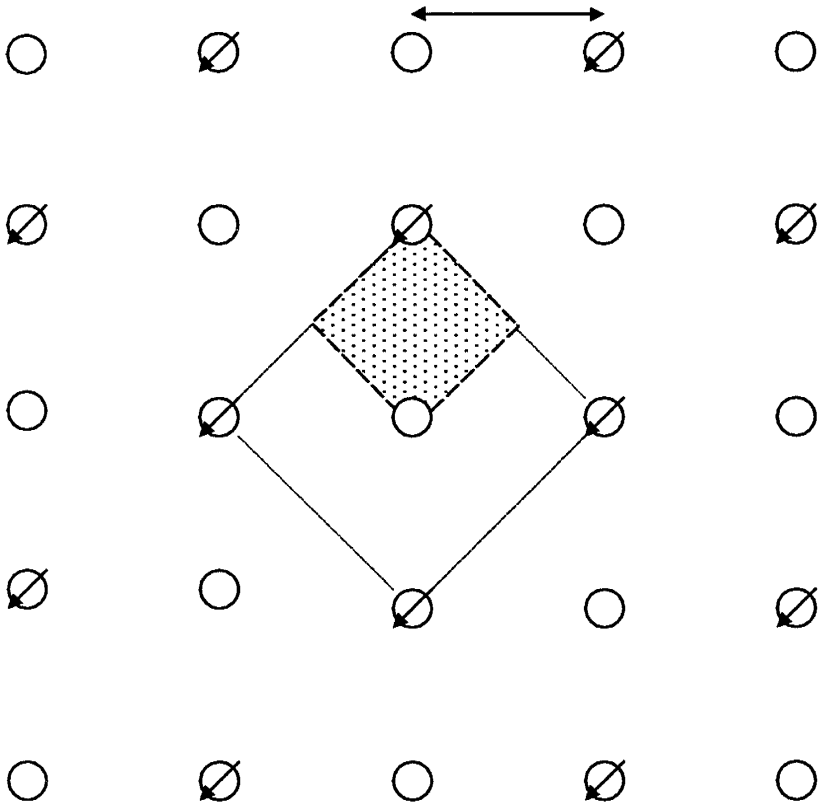

Figure 1(c). 5-Spot Drive Pattern. The shaded area marks the element of symmetry for the pattern.. Aspect ratio is always 1, (since a = d by definition).

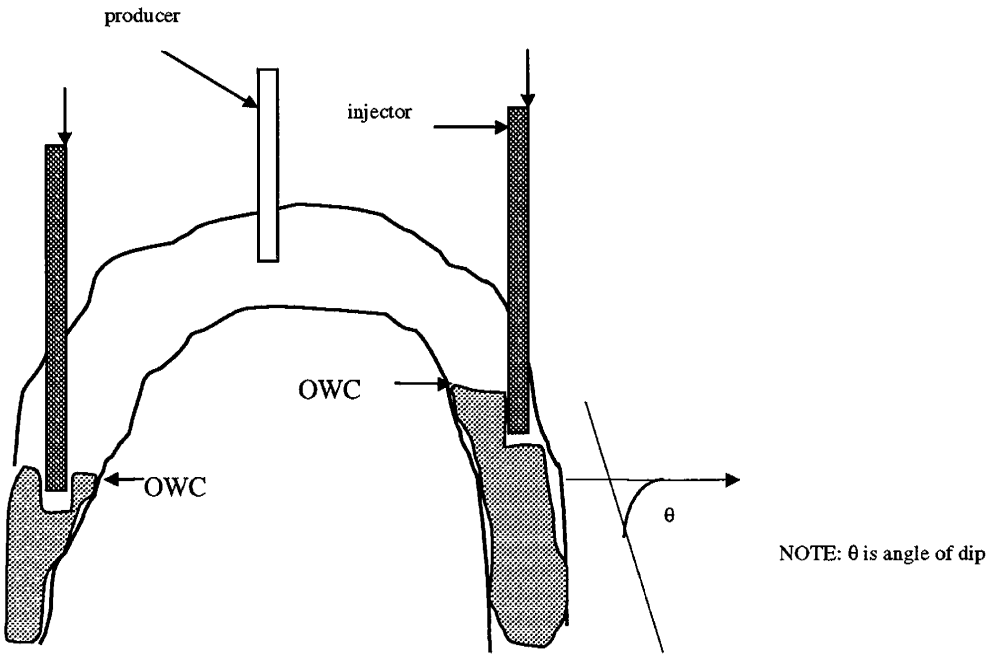

Figure 1(d). Peripheral or Edge Water Drive (EWD) Waterflooding. Most common applications are offshore dipping reservoirs.

Peripheral flooding, as illustrated in Fig. 1(d), combined with irregularly spaced injection and producing wells is gaining application in offshore deep-water development especially where the reservoirs are steeply dipping. This application provides a frontier that is also worth further understanding and research. It is noteworthy that new field discoveries are now mostly confined to offshore locations in increasing water depths. This trend may increasingly make peripheral waterflooding more relevant. Unfortunately, the literature is very sparse on peripheral flooding.

Reservoir pressure is the driving force for production of oil and gas from the subsurface oil/gas reservoirs. Interestingly, subsurface flow patterns mimic what is generally observed at the surface. That is, fluids flow through the path of least resistance from high-pressure regions to low-pressure regions. Streamlines, thus, offer a qualitative and quantitative conceptualization of reservoir flows and a means to evaluate various development scenarios. A streamline is a hypothetical line across which there is no flow, and can be defined as the locus of points defining the path of motion of an elemental volume of fluid. Thus, a streamtube which is formed by two streamlines is an envelope with constant volume of fluid at steady-state conditions. The application of streamtube

modeling to predicting performance of oil/gas reservoirs is a vast frontier for research contributions and is currently a busy research area.

4.2.3 OBJECTIVES

Following the success of work by Wang *et al* (1999) on staggered-line drive and five-spot patterns, it is possible is to investigate the effects of aspect ratio and mobility ratio on areal sweep efficiency of direct-line-drive waterflood patterns using streamline/streamtube simulation. This will be done as a preliminary exercise where we will investigate recovery efficiency of a direct-line drive with a unit aspect ratio using streamtube/streamline simulation.

Secondly, we will provide a preliminary basis for the evaluation of recovery efficiencies of edge-water or peripheral-drive waterfloods using either a streamtube or black-oil model, or a combination of both.

The bottom line for any waterflood scheme is increased incremental oil recovery. Performance evaluation is a measure of volumetric sweep efficiency. Volumetric Sweep Efficiency, E_V, is defined as the ratio of volume swept to volume contacted by the displacing fluid. It can be decomposed into areal, E_A, and vertical, E_I, Sweep Efficiencies.

$$E_V = E_A \times E_I \tag{1.1}$$

Areal efficiency is the ratio of area contacted by displacing agent to the total area, while vertical sweep efficiency is the ratio of cross-sectional area contacted by displacing agent to the total cross-sectional area. Both areal and vertical efficiencies are normally obtained independently using correlation, analytical calculations, scaled laboratory models and numerical simulation.

Another parameter that gives a measure of the effectiveness of a waterflooding scheme, and thus helps in its management and monitoring, is mobility ratio. It is defined as the ratio of the effective permeability to the coefficient of viscosity of the displacing

phase upon the ratio of the permeability to the coefficient of viscosity of the displaced phase.

$$M = (k_d / \mu_d) / k_D / \mu_D \tag{1.2}$$

where subscript d stands for the displacing phase and D the displaced phase.

The displacement process is very favorable when mobility ratio is much less than unity, (that is $M << 1$).

4.2.4 LITERATURE REVIEW

Many authors and scholars have contributed to the evolution of waterflooding as a proven technique for enhanced, improved or simply incremental oil recovery. There are four methods for modeling oil/gas flows, namely - correlation, scaled physical models, analytical models and simulation models.

4.2.4.1 Laboratory Studies

Scaled physical models are popular because they afford a scaled observation of the actual scenario. The contributions of Dyes *et al.* (1954) are significant in this regard. Dyes *et al.* assumed piston-like displacement, in a regular, homogeneous confined pattern such as five-spot, staggered-line and direct-line. Their results plotted as areal sweep efficiency (E_A) versus mobility ratio (M), (indicate that areal sweep efficiency increases with dimensionless time and decreasing mobility ratio. Areal sweep efficiency also increases as the pattern drive geometry or configuration becomes more linear. Conversely, large mobility ratios are detrimental to the displacement process. Other contributors are Craig (1971), and Claridge (1972).

Dyes *et al.* (1957) also studied the effects of water breakthrough on oil production at different mobility ratios. Their work represents one of the earliest to study the effects of fluid mobilities on areal sweep efficiency after breakthrough in an injection scheme. It is noteworthy that prior to the work of Dyes *et al.*, post-breakthrough performance was unquantified and most researchers at that time limited their work to performance before

breakthrough. Dyes *et al.*'s results, therefore, positively impacted the economics of waterflood projects. The most interesting of their results was that over 50% of ultimate recovery is possible post breakthrough, although this recovery may be slow.

However, the success of Dyes *et al.* work is impaired by the simplifying assumptions that underlined their work. These assumptions are at variance with actual reservoirs, which are naturally heterogeneous. Though experiments afford the opportunity of observing in-situ the reservoir displacement mechanisms, it is clear that they cannot be made to capture all the details and characteristics of the reservoir. Simulation offers a tremendous advantage over experiments in this regard as it can be made to account for local heterogeneities as may be desired.

4.2.4.2 Simulation

Simulation models are many and varied, with the black-oil model being the most widespread in the industry. The black-oil model when solved using conventional finite - difference methods displays numerical dispersion and excessive run times when fine grids are used. These problems can become amplified when used to model large waterflood reservoirs.

The streamline theory of water/oil/gas flows has received a significant and practical contribution via the work of Thiele *et al.* (1994). They simulated convective displacements in heterogeneous reservoirs by mapping fluid displacements as streamtubes while accounting for the mobility changes within the reservoir. Their work has culminated in the versatile streamtube simulator (3DSL).

Wang *et al.* (1999) recently investigated the effects of mobility ratio on pattern behavior of a homogeneous porous medium using 3DSL. They confirmed that staggered-line drive has better areal sweep efficiency (E_A) than an equivalent five-spot pattern at unit mobility ratio (that is, at $M = 1$). Notably, they obtained an interesting result that at very favorable mobility ratio ($M < 1$), a five-spot pattern has a higher areal sweep

efficiency than staggered-line drive, a result which corroborates the experimental results of Dyes *et al.*

Direct-line drive represents the beginning point for our exploration of waterflood operations while peripheral flooding represents another extreme. Peripheral flooding represents an unexplored challenge particularly utilizing the streamtube modeling approach.

4.2.4.3 Analytical Methods

Two common approaches to modeling fluid kinematics are Eulerian and Lagrangian methods. Both methods are predicated on kinetic energy theory that fluids are continua. In the Lagrangian method, the history of an elemental volume of fluid is followed. The elemental fluid volume is identified by its spatial coordinates at the instant time $t = 0$ and its coordinates at any later time t are functions of time t, and the initial coordinates. The path of an elemental volume of fluid is the curve of fundamental importance in the Lagrangian method.

The Eulerian method is a cinematographic approach, and the basic concept is the state of velocity throughout the whole region occupied by the fluid at one instant. The complete state of motion is given by succession of such instantaneous pictures of the state of flow. In this method, the curve of fundamental importance is the streamline. The Eulerian method is utilized in this work to model waterflood performance via 3DSL. Hence, a summary of the Eulerian approach is given.

A streamline is a curve such that its tangent is parallel to the velocity of fluid, at a given instant, at the point of interest. At a given instant, a streamline is the locus of all the elemental fluid volumes which have passed through a fixed point within the fluid. Thus at steady state, streamlines are identical to the paths of the elemental fluid volumes.

Eulerian Approach

Applying the continuity equation to the control volume $\delta x \delta y \delta z$ in 3D.

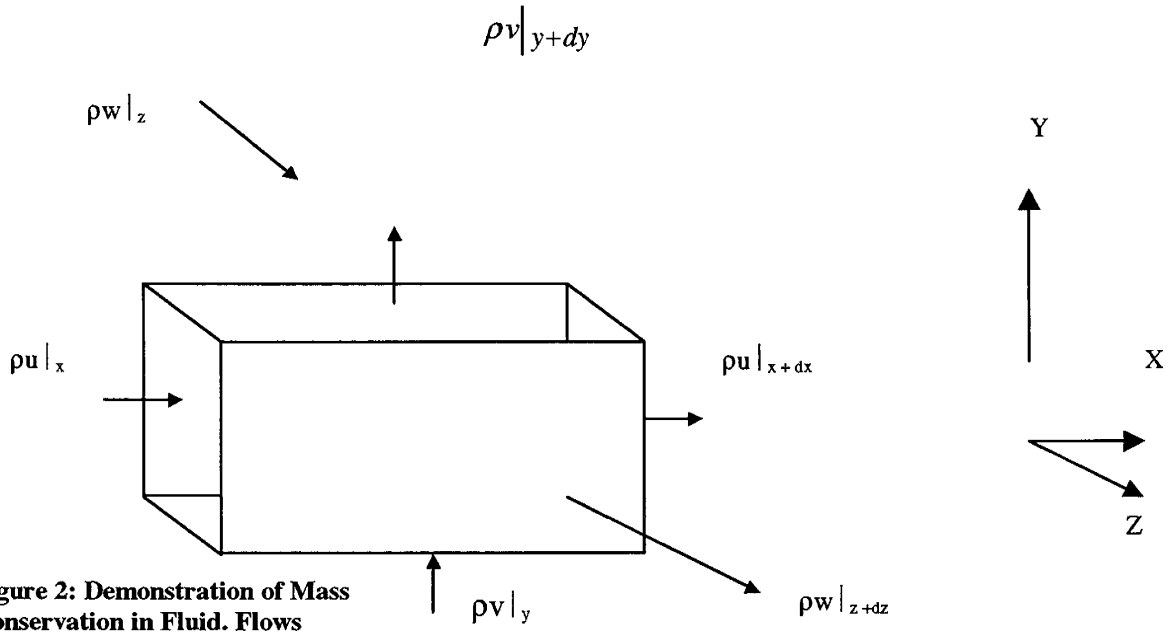

Figure 2: Demonstration of Mass Conservation in Fluid. Flows

The net mass flow per unit cross sectional area in the $x-$direction is

$$\rho u|_x - \rho u|_{x+dx} \tag{1.3}$$

where u is the velocity in the $x-$direction.

Similarly, the net amount of mass leaving the box per second through the $y-$ and $z-$ faces are $\rho v|_y - \rho v|_{y+dy}$

$$\rho w|_z - \rho w|_{z+dz} \tag{1.4}$$

where v and w are the velocities in the $y-$and $z-$direction respectively.

Using Taylor's expansion and neglecting terms of order 2 , the accumulation of mass per second in the control volume is –

$$\delta z\left[\frac{\partial(\rho u)}{\partial x}+\frac{\partial(\rho v)}{\partial y}+\frac{\partial(\rho w)}{\partial z}\right]\delta x\delta y\delta z \tag{1.5}$$

The rate of change of mass of the fluid in the box is –

$$\left(\frac{\partial \rho}{\partial t}\right)\delta x\delta y\delta z \tag{1.6}$$

Equating total accumulation to rate of change of mass:

$$-\frac{\partial p}{\partial t}+\frac{\partial(\rho u)}{\partial x}+\frac{\partial(\rho v)}{\partial y}+\frac{\partial(\rho w)}{\partial z}=0$$

Expanding the derivatives,

$$-\frac{\partial \rho}{\partial t}+\frac{u\partial \rho}{\partial x}+\frac{v\partial \rho}{\partial y}+\rho\left(\frac{\partial u}{\partial x}+\frac{\partial v}{\partial y}+\frac{\partial w}{\partial z}\right)=0 \tag{1.7}$$

For steady and incompressible flow the equation reduces to,

$$\frac{\partial u}{\partial x}+\frac{\partial v}{\partial y}+\frac{\partial w}{\partial z}=0 \tag{1.8}$$

The divergence of the velocity vector is zero as expected.

$$\nabla\left(u_i+v_j+w_k\right)=0 \tag{1.9}$$

The stream function (or current function) is defined as a line everywhere tangent to the velocity vector. The stream function is the line integral of the normal velocity component from a specified source to a sink. A streamline is thus also defined as the locus of points of equal stream function.

The amount of fluid flowing across any path between two points on two streamlines is the change in stream function between the two lines. In 2-D, this change in stream function is

$$d\Psi = -vdx + udy \tag{1.10}$$

where Ψ is the stream function.

Expressing the change in stream function as a total derivative:

$$d\Psi = \partial\Psi / \partial x\big|_y dx + \partial\Psi / \partial y\big|_x dy \tag{1.11}$$

Comparing Eqs. (1.10) and (1.11)

$$u = - \partial\Psi / \partial y$$

$$v = \partial\Psi / \partial x \tag{1.12}$$

Injectors and Producers as Source-Sink Pairs

From a source (the injector) in the reservoir, displacing fluid issues symmetrically in all directions provided that permeability and pressure fields are homogeneous and the displaced fluid is produced at a sink (the producer). The strength of the source which defines the flow field, is determined by the permeability and in-situ pressure gradient distributions.

In 3DSL producers and injectors are modeled as sinks and sources, respectively. Consider a source-sink pair of equal strength $\pm m$ and situated a distance $2c$ apart (Fig. 3), in a homogeneous porous medium where the pressure gradient is initially zero.

The stream function at a point $P(r,\theta)$ due to this combination is

$$\Psi = \frac{m\theta_1}{2\pi} - \frac{m\theta_2}{2\pi} = \frac{m\beta}{2\pi} \tag{1.13}$$

But $\tan\theta_1 = y/(x-c)$, $\tan\theta_2 = y/(x+c)$,

and $\tan(\theta_1 - \theta_2) = (\tan\theta_1 + \tan\theta_2)/(1 + \tan\theta_1 \tan\theta_2)$,

therefore,

$$\theta_1 - \theta_2 = \beta = \arctan\,[2cy/(x^2 + y^2 - c^2)] \tag{1.14}$$

Substituting,

$$\Psi = m\beta/2\pi = m/2\pi \arctan\,[2cy/(x^2 + y^2 - c^2)] \tag{1.15}$$

A plot of the stream function gives streamlines, which are a series of circles with passing through the y-axis and intersecting at the source and sink.

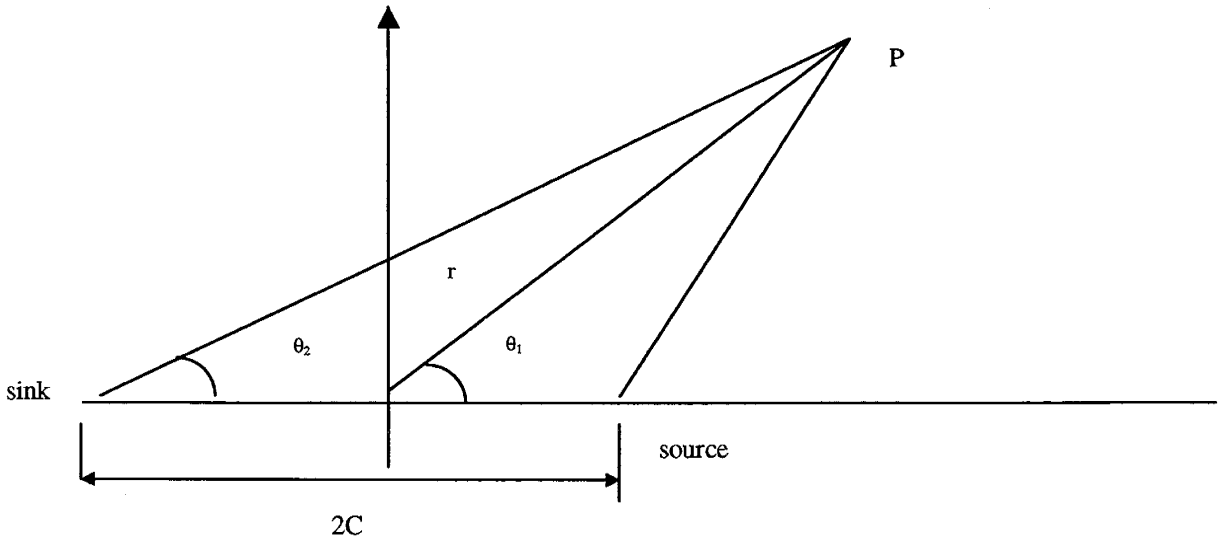

Figure 3 – Source-Sink Geometry

4.2.5 FUTURE WORK PLANS

Work on this project has just begun. Future plans follow.

1. Continue exploring the use of 3DSL with several hypothetical case(s) and actual field data for direct-line drive pattern.

2. Search the literature for work related to edge-water injection (EWD), such as gravity drainage and bottom-water drive.
3. Formulate the component parts/considerations required for evaluation and management of EWD.
    - Investigate each factor with 3DSL
    - Identify necessary modifications to 3DSL if necessary.
    - Collect actual field data
        - History match production and pressure profiles
    - Attempt simulation with ECLIPSE using identical data sets
    - Compare results of 3DSL to ECLIPSE
4. Summarize conclusions

    Direct-line drive

    Edge Water Drive
5. Prepare Final Report.

4.2.6 REFERENCES

1. Dyes, A.B., B. H. Caudle, and R. A. Erickson: "Oil Production after Breakthrough – as Influenced by Mobility Ratio," in *Petroleum Transactions, AIME*, **201**, Paper #3784 (1954).
2. Wang, Y., A. R. Kovscek, and W. E. Brigham: "Effects of Mobility Ratio on Pattern Behavior of A Homogeneous Porous Medium", *In Situ* (1999).
3. Yazdi, Mojtaba and Paul B. Crawford: "Performance of a Simulated Fractured Matrix Subject to Bottom-Water Drive", SPE, paper 4573 (1973).

4. Thiele, M.R., M.J. Blunt, and F.M. Orr: "A New Technique for Predicting Flow in Heterogeneous Systems Using Streamtubes," paper 27834, presented at the SPE's Ninth Symposium on Improved Oil Recovery, Tulsa, Oklahoma (April 17-20, 1994).

5. Bates, G.R. and W.A. Flanders: "Optimizing Reservoir Surveillance by Using Streamlines and the Microcomputer," SPE Paper 16482 (1987).

6. Smith, Charles Robert: Mechanics of Secondary Oil Recovery, Reinhold Publishing Corporation, New York (1966).

7. Lake, Larry W.:, "Enhanced Oil Recovery", Prentice Hall Inc., Englewood Cliffs, New Jersey (1989).

8. Mojola, O. O.: "Course Notes for Fluid Mechanics II", Obafemi Awolowo University, Ife – Nigeria, (unpublished) (1986).

9. Willhite, G. Paul: "Waterflooding", SPE Textbook Series, Society of Petroleum Engineers, Richardson, TX (1986).

PROJECT 5: FIELD SUPPORT SERVICES

To provide technical support for design and monitoring of DOE sponsored or industry initiated field projects.

Even though no project directly related to field support services was completed this year, SUPRI personnel have been active in information exchange and results dissemination. Those activities include holding the annual meeting of our Industrial Advisory Committee with eight companies attending. We have also participated in the Annex IV of the research agreement between the U.S. Department of Energy and the Venezuelan Ministry of Energy and Mines. Presentation of technical papers was made at various Society of Petroleum Engineers meetings as well as at the International Energy Agency Annual scientific meeting. Our researchers have participated in some of the Petroleum Technology Transfer Center West Coast activities. Technical reports and selected publications are available on the Worldwide Web at: www.ekofisk.stanford.edu//SUPRI-A .